Transport AC loss in high temperature superconducting coils

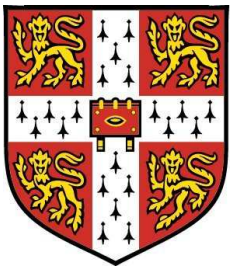

Mark Ainslie

King's College

University of Cambridge

A thesis submitted for the degree of

Doctor of Philosophy

January 24, 2012

Declaration

The work presented in this dissertation was carried out at the Department of Engineering, University of Cambridge, between January 2009 and January 2012 under the supervision of Dr. Tim Flack.

The author declares that, except for where specific reference is made to the work of other authors or specifically indicated in the text, the contents of this dissertation are his own work, and include nothing done in collaboration. This report has not been previously submitted in part, or in whole, to any other university for a degree, diploma or other qualification. This dissertation is within the word limit of 65,000 words, including appendicies, bibliography, footnotes, tables, and equations, and does not contain more than 150 figures.

Acknowledgements

There are a number of people who have contributed, either directly or indirectly, to the work presented in this thesis and for their contributions I am extremely thankful.

Firstly, I would like to express my utmost gratitude to my supervisor, Dr. Tim Flack, for his advice, guidance and support throughout the duration of my research. He taught me the skills required for independent research and allowed me the freedom to explore my own ideas, whilst providing appropriate guidance and criticism to ensure that I carried out my research professionally and completed my work on time.

I would like to also thank the members of the Bulk Superconductivity Group in the Department of Engineering at the University of Cambridge for their support and welcoming me into their group. In particular, group leader Prof. David Cardwell for support and advice and extensive knowledge of superconductivity, Prof. Archie Campbell for his informative discussions on superconductor modelling and experimentation, Dr. John Durrell for his technical expertise and informative discussions, and Mr. Tony Dennis for his technical assistance.

I must also thank the EPEC Superconductivity Group in the Department of Engineering for their advice, allowing access to experimental equipment and assistance with experiments. In particular, Dr. Tim Coombs, Dr. Zhiyong Hong, Dr. Weijia Yuan, and Dr. Ruilin Pei.

I attended a number of conferences and workshops during my PhD, and I am extremely grateful to those who I have collaborated with or who have provided comments and constructive criticism of my work:

Assoc. Prof. Frederic Sirois, Dr. Victor Rodriguez-Zermeno, and Dr. Francesco Grilli for their assistance with numerical modelling; Dr. Milan Majoros, Dr. Fedor Gomory, Dr. Stephen Ashworth, Dr. Enric Pardo, and Prof. Pascal Tixador for their assistance with AC loss measurements.

Prof. Harry Jones and Mr. Anthony Hickman at the University of Oxford must also be thanked for winding the circular superconducting pancake coil.

Finally, I must thank all of my friends and family for their love and support. My parents, Harry and Christine, have supported me in all of my pursuits and encouraged me to set my goals for achievement high. My partner, Briony, has supported me wholeheartedly, and without her help and encouragement, I would not have achieved all that I have thus far. The emotional support required to complete a PhD is often underestimated.

Abstract

In this dissertation, the problem of calculating and measuring AC losses in superconducting coils is addressed, with a particular focus on the transport AC loss of coils for electric machines. In order to model the superconducting coil's electromagnetic properties and calculate the AC loss, an existing two dimensional (2D) finite element model that implements a set of equations known as the H formulation, which directly solves the magnetic field components in 2D, is extended to model a superconducting coil, where the cross-section of the coil is modelled as a 2D stack of superconducting coated conductors.

The model is also modified to allow the inclusion of a magnetic substrate, which is present in some commercially available HTS wire. The analysis raises a number of interesting points regarding the use of superconductors with magnetic substrates. In particular, the presence of a magnetic substrate affects the penetration of the magnetic flux front within the coil and increases the magnetic flux density within the penetrated region, both of which can increase the AC loss significantly. In order to investigate these findings further, a comprehensive analysis on stacks of tapes with weak and strong magnetic substrates is carried out, using a symmetric model that requires only one quarter of the cross-section to be modelled.

In order to validate the modelling results, an extensive experimental setup is designed and built to measure the transport AC loss of a superconducting coil using an electrical method based on inductive compensation by means of a variable mutual inductance. Measurements are carried out on the superconducting racetrack coil and it is found that the experimental results agree with the modelling results

for low current, but some phase drift occurs for higher current, which affects the accuracy of the measurement. In order to overcome this problem, a number of improvements are made to the initial setup to improve the lock-in amplifier's phase setting and other aspects of the measurement technique.

New measurements are carried out on a single, circular pancake coil and the discrepancies between the experimental and modelling results are described in terms of the assumptions made in the model and aspects of the coil that cannot be modelled. Using the original measured properties of the superconducting tape, there is an order of magnitude difference between the experiment and model. The properties of the superconductor can degrade during the winding and cooling processes, and a critical current measurement of the coil showed that the tape critical current reduced from nearly 300 A, down to around 100 A. Applying this finding to the model, the experimental and modelling results show good agreement, and the difference in the slope of the AC loss curve can be described in terms of the B-dependent critical current dependency $J_c(B)$ used in the model.

Finally, methods used to mitigate AC loss in superconducting wires and coils are summarised, and the use of weak and strong magnetic materials as a flux diverter is investigated as a technique to reduce AC loss in superconducting coils. This technique can achieve a significant reduction in AC loss and does not require modification to the conductor itself, which can be detrimental to the superconductor's properties.

List of publications

- **M.D. Ainslie**, J.H. Durrell, A.R. Dennis, S.P. Ashworth, A.M. Campbell, T.J. Flack, "Transport AC loss measurements of a YBCO-based superconducting pancake coil," submitted for review (*Supercond. Sci. Technol.*), 2012

- **M.D. Ainslie**, T.J. Flack, A.M. Campbell, "Calculating transport AC losses in stacks of high temperature superconductor coated conductors with magnetic substrates using FEM," *Physica C*, Vol. 472, No. 1, p. 50-56, 2011

- **M.D. Ainslie**, V.M. Rodriguez-Zermeno, Z. Hong, W. Yuan, T.J. Flack, T.A. Coombs, "An improved FEM model for computing transport AC loss in coils made of RABiTS YBCO coated conductors for electric machines," *Supercond. Sci. Technol.* 24 (2011) 045005 (8pp)

- **M.D. Ainslie**, W. Yuan, Z. Hong, R. Pei, T.J. Flack, T.A. Coombs, "Modeling and Electrical Measurement of Transport AC Loss in HTS-based Superconducting Coils for Electric Machines," *IEEE Trans. Appl. Supercond.*, Vol. 21, No. 3, p. 3265-3268, 2011

- **M.D. Ainslie**, T.J. Flack, Z. Hong, T.A. Coombs, "Comparison of First- and Second-Order 2D Finite Element Models for Calculating AC Loss in High Temperature Superconductor Coated Conductors," *COMPEL: The International Journal for Computation and Mathematics in Electrical and Electronic Engineering*, Vol. 30, Iss. 2, p. 762-774, 2011

- **M.D. Ainslie**, Y. Jiang, W. Xian, Z. Hong, W. Yuan, R. Pei, T.J. Flack, T.A. Coombs, "Numerical analysis and finite element modelling of an HTS synchronous motor," *Physica C*, Vol. 450, No. 20, p. 1752-1755, 2010

- W. Yuan, **M.D. Ainslie**, W. Xian, Z. Hong, Y. Yan, R. Pei, T.A. Coombs, "Theoretical and experimental studies on Jc and AC losses of 2G HTS coils," *IEEE Trans. Appl. Supercond.*, Vol. 21, No. 3, p. 2441-2444, 2011

- R. Pei, R. Viznichenko, **M.D. Ainslie**, Z. Hong, W. Xian, L. Zeng, W. Yuan, T.A. Coombs, "The Ic Behavior of 2G YBCO Tapes under DC/AC Magnetic Fields at Various Temperatures", *IEEE Trans. Appl. Supercond.*, Vol. 21, No. 3, p. 3226-3229, 2011

- Z. Hong, W. Yuan, **M. Ainslie**, Y. Yan, R. Pei, T.A. Coombs, "AC Losses of Superconducting Racetrack Coils in Various Magnetic Conditions," *IEEE Trans. Appl. Supercond.*, Vol. 21, No. 3, 2466-2469, 2011

- Z. Hong, Z. Jin, **M. Ainslie**, J. Sheng, W. Yuan, T.A. Coombs, "Numerical Analysis of the Current and Voltage Sharing Issues for Resistive Fault Current Limiter Using YBCO Coated Conductors," *IEEE Trans. Appl. Supercond.*, Vol. 21, No. 3, p. 1198-1201, 2011

- W. Yuan, W. Xian, **M. Ainslie**, Z. Hong, Y. Yan, R. Pei, T.A. Coombs, "Design and Tests of a Superconducting Magnetic Energy Storage (SMES) coil," *IEEE Trans. Appl. Supercond.*, Vol. 20, No. 3, p. 1379-1382, 2010

- W. Yuan, A.M. Campbell, Z. Hong, **M. Ainslie**, T.A. Coombs, "Comparison of AC losses, magnetic field/current distributions and critical currents of superconducting circular pancake coils and infinitely long stacks using coated conductors," *Supercond. Sci. Technol.* 23 (2010) 085011 (8pp)

Contents

List of Figures

List of Tables

Chapter 1

Introduction

The annual world electricity consumption was estimated at 138 trillion kWh in 2006, and is estimated to reach almost 200 trillion kWh in the year 2030 [1]. Given that there is a finite quantity of fossil fuel remaining, and the world's population continues to grow, our existing methods for energy supply and usage are clearly unsustainable. In developed industrialised nations, such as the UK and the US, the industrial sector uses about one third of all energy consumed [2], and approximately two thirds of this energy is consumed by electric motor drives [3].

Scientists and engineers can provide an important contribution to the reduction of energy consumption and its associated environmental pollution. Electrical energy consumption can be reduced in electric machines in the following ways: good housekeeping (for example, switching idling motors off), the use of variable-speed drives, and the construction of electric motors and generators with better efficiency [4]. Loss of electrical energy due to resistance to current flow, which is prevalent in conventional machines, translates directly to wasted energy and, therefore, to wasted economic resources.

Superconductivity offers zero to near zero resistance to electrical current when cooled down to a particular cryogenic temperature. Consequently, the use of superconducting materials can improve the overall electrical system efficiency. In addition, superconducting materials are able to carry much larger current densities than conventional materials, such as copper. In electric machines, in particular, increasing the current and/or magnetic flux density increases the power density, which leads to reductions in both size and weight. The expected improved

performance and efficiency, as well as a smaller footprint in comparison with conventional devices, has seen continued interest in introducing superconducting materials to not only electric machines, but other electric power applications, such as cables, superconducting fault current limiters (SFCL) and transformers.

Investigating and modelling the electromagnetic behaviour of superconductors is crucial to the design of superconductor-based electrical devices. In order for these devices to be cost- and performance-competitive with conventional devices, the use of superconducting materials and the associated cooling system must be shown to possess improved properties in comparison to its conventional counterpart. Although lossless for DC (direct current), superconductors do experience AC (alternating current) losses, which can be a significant problem in any device exposed to a time-varying current or magnetic field. Since superconductors require operation at cryogenic temperatures, these AC losses increase the refrigeration load, which decreases the overall efficiency and increases the technological complexity of the design.

In an electric machine, there are usually multiple superconductors in tape/wire form wound into coils and interacting together in a complex magnetic environment. It is only in recent years that long lengths of wire have been available commercially, which has made it possible to wind coils and cables for large scale applications. Significant efforts have been made to understand the complex interactions between multiple superconducting coated conductors in quite simple geometries, but no reliable technique exists to both model and measure AC losses in more complex geometries, such as superconducting coils. Superconducting coils are found in a number of different applications, such as superconducting magnetic energy storage (SMES) systems and transformers.

This dissertation aims to address the problem of calculating and measuring AC losses in superconducting coils, with a particular focus on the transport AC loss of coils for electric machines. In order to model the superconducting coil's electromagnetic properties and calculate the AC loss, a two dimensional (2D) finite element model that implements a set of equations known as the H formulation has been developed, which directly solves the magnetic field components in 2D, where the cross-section of the coil is modelled as a 2D stack of superconducting coated conductors.

Firstly, in order to optimise the coil model in terms of accuracy of solution and computational speed, an investigation is carried out on the artificial expansion of the thickness of the YBCO layer and selecting an appropriate mesh type and number of elements. This is done using a single tape, as the preliminary groundwork for optimising more complex geometries. The artificial expansion technique is then applied to the geometry of a superconducting racetrack coil of an all-superconducting high-temperature superconductor (HTS) permanent magnet synchronous motor to model the individual turns of the coil, and the result is compared with a model using a bulk approximation. The limitations of the artificial expansion technique and its application to coils is discussed in detail.

A technique is then applied that allows the actual superconducting layer thickness to be modelled without the associated problem of increased computation time due to a large number of mesh elements, and a comprehensive study on the minimum number of mesh elements required for accurate results is carried out. The model is also modified to allow the inclusion of a magnetic substrate, which is present in some commercially available HTS wire. The analysis raises a number of interesting points regarding the use of superconductors with magnetic substrates, and a comprehensive analysis on stacks of tapes with weak and strong magnetic substrates is provided, using a symmetric model that requires only one quarter of the cross-section to be modelled.

In order to validate the modelling results, an extensive experimental setup has been designed to measure the transport AC loss of a superconducting coil using an electrical method based on inductive compensation by means of a variable mutual inductance. Electrical measurement methods are generally faster than calorimetric methods and provide greater sensitivity, but a major problem when applying this technique to a superconducting coil is the compensation of the much larger inductive component of the coil's voltage. Since the voltage related to the superconducting coil's AC loss, which is in-phase with the current, is orders of magnitude less than the coil's inductive voltage, which is 90° out of phase with the current, the loss voltage is difficult to extract using conventional measurement techniques. The variable mutual inductance is utilised to cancel the inductive voltage, and is used in conjunction with a lock-in amplifier, which can extract a signal with a known carrier wave where the signal-to-noise ratio is very

small. Measurements are carried out on the superconducting racetrack coil, as well as a circular pancake coil, and the validity of the modelling and experimental techniques is investigated in detail in regards to estimating a superconducting coil's transport AC loss.

The transport AC loss of a superconducting coil is found to be significantly large, and this will reduce the efficiency of the device in which it is utilised, particularly when the loss is reflected back to room temperature by including the refrigeration cost. Many existing AC loss mitigation techniques involve modification of the HTS conductor itself, which can cause significant degradation of the conductor properties. Therefore, an investigation is carried into the use of weak or strong magnetic materials to manipulate the magnetic flux in a superconductor to reduce the AC loss, which is presented for stacks of tapes with and without a (weak) magnetic substrate. The use of external magnetic materials as a flux diverter can achieve a significant reduction in AC loss without modifying the original conductor, and shows promise as a technique to mitigate AC losses in practical superconducting coils.

An overview of the structure of the dissertation is provided in the following section. A thorough literature review is presented at the beginning of each chapter for the three main sections: modelling of HTS-based superconducting coils, measurement of AC loss in HTS-based superconducting coils, and AC loss mitigation.

1.1 Thesis outline

In Chapter 2, a brief introduction to superconductivity is presented, including the main commercially available high temperature superconductor materials. The underlying theoretical principles relating to the topics covered in this dissertation are then presented, including the existing analytical techniques for modelling the electromagnetic properties of HTS materials, followed by the mechanisms for and analytical calculation of AC loss for these materials in simple geometries. This theoretical background is referred to extensively in later chapters and forms the basis for comparing the results using the finite element method in the following chapter.

In Chapter 3, the modelling of HTS-based superconducting coils using the finite element method is described in detail, including the evolution of the development of the coil model as the research in this dissertation has progressed. Often there is a compromise in computer modelling between the accuracy of the solution and the computational time required, and a number of different models are compared to examine the optimum parameters. Firstly, the numerical model used in this thesis is described, which is based on solving a set of Maxwell's equations in 2D implementing the H formulation using the commercial software package Comsol Multiphysics. The coil cross-section is modelled as the number of individual turns in the coil, and an artificial expansion technique is investigated to improve the computational speed of the model, which can require hundreds of thousands of mesh elements. Different methods to approximate the critical current density J_c are also discussed. A technique that allows the real superconducting layer thickness to be modelled, using a mapped mesh, is then investigated, and the model is modified to include the magnetic substrate present in some superconducting tapes. This investigation raises some interesting points for further analysis, and a detailed investigation on stacks of superconducting tapes with both weak and strong magnetic substrates is carried out at the end of the chapter.

In Chapter 4, the measurement of AC loss in HTS-based superconducting coils is described in detail, including an experimental setup that uses an electrical technique to accurately measure the transport AC loss of a superconducting coil. The experimental technique is based on the use of a lock-in amplifier to extract the in-phase component of the superconducting coil voltage, which corresponds to the AC loss voltage. In order to compensate for the coil's large inductive voltage, a variable mutual inductance is used. The technique is applied firstly to measure the racetrack coil introduced in the previous chapter. It is found that the experimental results agree with the modelling results for low current, but some phase drift occurs for higher current, which affects the accuracy of the measurement. In order to overcome this problem, a number of improvements are made to the initial setup to improve the lock-in amplifier's phase setting and other aspects of the measurement technique, including the use of the signal generator's reference (TTL) output and a Rogowski coil to provide stable reference signals to accurately set the reference phase of the lock-in amplifier, and new measurements

are carried out on a single, circular pancake coil. Discrepancies between the experimental and modelling results are described in terms of the assumptions made in the model and aspects of the coil that cannot be modelled. Finally, some suggestions to improve the experimental setup in the future are presented.

In Chapter 5, methods used to mitigate AC loss in superconducting wires and coils are summarised, and the use of weak and strong magnetic materials as a flux diverter is investigated as a technique to reduce AC loss in superconducting coils that does not require modification to the conductor itself, which can be detrimental to the superconductor's properties.

Chapter 6 summarises the contributions of the research completed thus far and its implications, and discusses possible directions of research in this area in the future.

Chapter 2

Superconductivity and theoretical overview

This chapter aims to present a brief introduction to superconductivity, including the main commercially available high temperature superconductor materials. The underlying theoretical principles relating to the topics covered in this dissertation are then presented, including the existing analytical techniques for modelling the electromagnetic properties of HTS materials, followed by the mechanisms for and analytical calculation of AC loss for these materials in simple geometries. This theoretical background is referred to extensively in later chapters and forms the basis for comparing the results using the finite element method in the following chapter.

2.1 Introduction to superconductivity

Superconductivity has come a long way since first being discovered in 1911 by H. Kamerlingh Onnes, one of the first professors in experimental physics at Leiden University. Kamerlingh Onnes observed that the electrical resistance of metals such as mercury, lead and tin disappeared completely from a finite value in a small temperature range around a critical temperature, T_c, which is characteristic of the particular material. His first discovery was the disappearance of solid mercury's resistance below a temperature of around 4 K [5], which he reached

using a refrigeration technique he designed just three years earlier. He received the Nobel Prize in Physics in 1913 for his work regarding the properties of matter at low temperatures.

Perfect conductivity was the first phenomenalogical characteristic of superconductivity; however, in 1933, perfect diamagnetism in these materials was discovered by Meissner and Ochsenfeld, which meant that a superconductor completely expelled an applied magnetic field except for a distance of λ, the penetration depth [6]. This became known as the Meissner effect.

Therefore, to prove the existence of superconducting material, it was necessary to observe two principal properties in the superconductor: the disappearance of resistance and the complete expulsion of an applied magnetic field. A superconductor can be characterised by its critical temperature, T_c, its critical magnetic field, H_c, and its critical current density, J_c, as shown in Figure 2.1. These parameters define the upper limits for the superconductivity in a material and can be used to describe the state a superconductor is in (superconducting or normal) for a given set of conditions [7]. The shaded volume in this figure corresponds to the material being in its superconducting state.

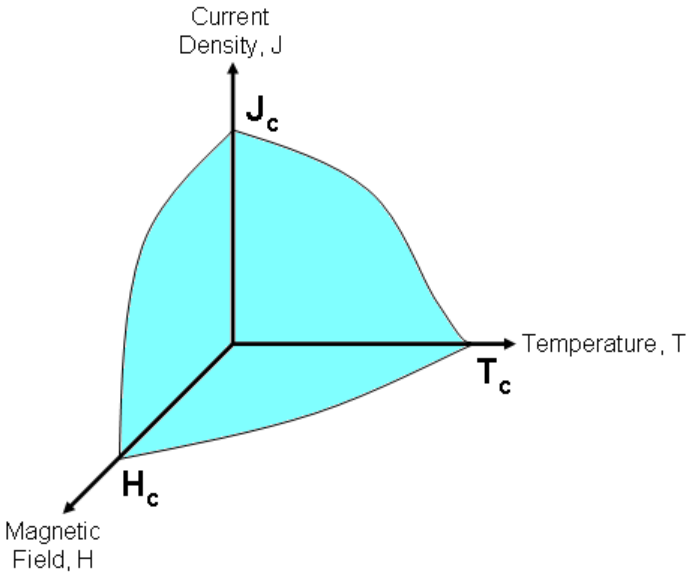

Figure 2.1: Characteristics of superconductivity

By the end of the 1960s, a remarkably complete and satisfactory theoretical picture of classic superconductors had emerged, based around the Meissner effect [6], the London equations [8], Ginzburg-Landau theory [9], and BCS (Bardeen-Cooper-Schrieffer) theory [10].

2.1.1 Type I & type II superconductors

For many years it was thought that the behaviour described above was inherent to all superconductors, but in 1957 Alexei Alexeyevich Abrikosov published a theoretical paper regarding another class of superconductors that may have different properties [11]. It is now realised that the apparently irregular properties of certain superconductors are not just effects of impurities, but inherent features of another class of superconductors, called 'Type II' superconductors [12].

One of the characteristic features of 'Type I' superconductors is the Meissner effect (perfect diamagnetism) below H_c, which implies the existence of a surface energy boundary between any normal and superconducting regions in the metal. This plays an important role in determining a superconductor's type [13]. Above H_c the type I superconductor reverts back to the normal state, where the magnetic field fully penetrates the material. Type I superconductors are limited in their current-carrying capacity due to the Meissner effect and Ampere's law. Current flow in a conductor is accompanied by a self-induced magnetic field, which are both confined to the outer layer as the field is excluded from the interior by the Meissner effect. According to Silsbee's criterion of depairing current, a superconductor loses its zero resistance when at any point on the surface the total magnetic field strength (due to the transport current and applied magnetic field) exceeds H_c [14]. The maximum current that can be carried by a Type I superconductor with a circular cross-section and radius r is given by $I_c = 2\pi r H_c$ [15]. For currents above this value, the self-induced magnetic field is large enough to destroy the superconducting state [16]. This transformation of a superconducting wire to the normal state when the current passing through it exceeds the critical value is called the Silsbee effect [15]. The critical value H_c is dependent on the temperature:

$$H_c = H_o(1 - (\frac{T}{T_c})^2) \tag{2.1}$$

Silsbee's criterion mentioned above holds only for type I superconductors, whereas for type II superconductors, the complete explusion of flux at $H < H_c$ does not take place [14]. Type I superconductors have a positive surface energy; however, type II superconductors have a negative surface energy, which leads to a 'mixed state,' where there exists an upper and lower critical magnetic field, H_{c2} and H_{c1}, respectively. In the mixed state, the magnetic field penetrates partially into the material in the form of vortices. These vortices (or flux tubes) are small tubular regions of the order of the coherence length ξ (a length scale that characterises superconducting electron pair coupling), each containing one quantum of flux, which Abrikosov determined as $\Phi_0 = \frac{h}{2e} = 2.1 \times 10^{-15}$ Tm^2. The vortices form a periodic lattice called the Abrikosov vortex lattice. The resistivity of the superconductor may be vanishing as long as the vortices are pinned or trapped. As the external field increases towards H_{c2}, the size of the superconducting region between the cores of the flux lines shrinks to zero, and the superconductor shows a continuous transition towards the normal state [17].

For magnetic fields below H_{c1}, the material is in the superconducting state and any magnetic field is expelled from the inside of the superconductor; above H_{c2}, the material is in the normal state and the superconductivity is largely confined to the surface of the material [18]. In this case, the number of vortices has reached its maximum and no more vortices can be added.

Type II superconductors can carry larger amounts of current in higher magnetic fields in comparison with Type I superconductors because H_{c2} can be hundreds of times larger than H_c. For example, the strongest type I superconductor (pure lead) has a critical field of around 80 mT (800 Gauss), whereas YBCO (Y-Ba-Cu-O) has an H_{c1} around 20 mT (200 Gauss) and an H_{c2} as high as 100 T [19]. The critical field as a function of temperature for each type of superconductor is shown in Figure 2.2.

There is also another defined field for type II superconductors, called the irreversibility field H_{irr}. For an applied magnetic field above this value, the vortices

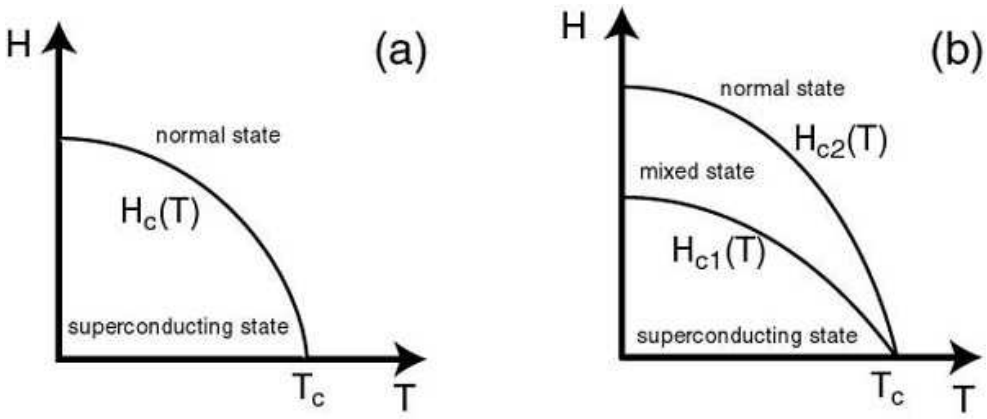

Figure 2.2: Critical magnetic field as a function of temperature for (a) type I superconductors and (b) type II superconductors [13]

begin to move, creating additional dissipation. H_{irr} is considered the practical limit of type II superconductors and is an order of magnitude lower than H_{c2} [18]. For YBCO, for example, the irreversibility field at 77 K is 5-6 T [20].

The group of type I superconductors is mainly comprised of metals and metalloids that show some conductivity at room temperature, including lead (Pb), mercury (Hg), tin (Sn), indium (In), and aluminium (Al), and form part of another group of superconductors called 'low temperature superconductors' (LTS). Except for the elements vanadium, technetium and niobium, the group of type II superconductors is comprised of metallic compounds and alloys, and this group includes some LTS, the high temperature superconductors (HTS) and magnesium diboride (MgB_2). Figure 2.3 shows a comparison of the different critical temperatures for many superconductors, as well as the year each superconductor was discovered. The axis on the right hand side shows equivalent examples for these temperatures. This dissertation focuses on HTS materials, in particular YBCO.

2.1.2 High temperature superconductors [22], [23]

High temperature superconductors were discovered in 1986, when Bednorz and Muller discovered LSCO ($La_{2-x}Sr_xCuO_2$) [24], for which they were conferred the fastest Nobel Prize ever awarded. These are layered materials dominated by

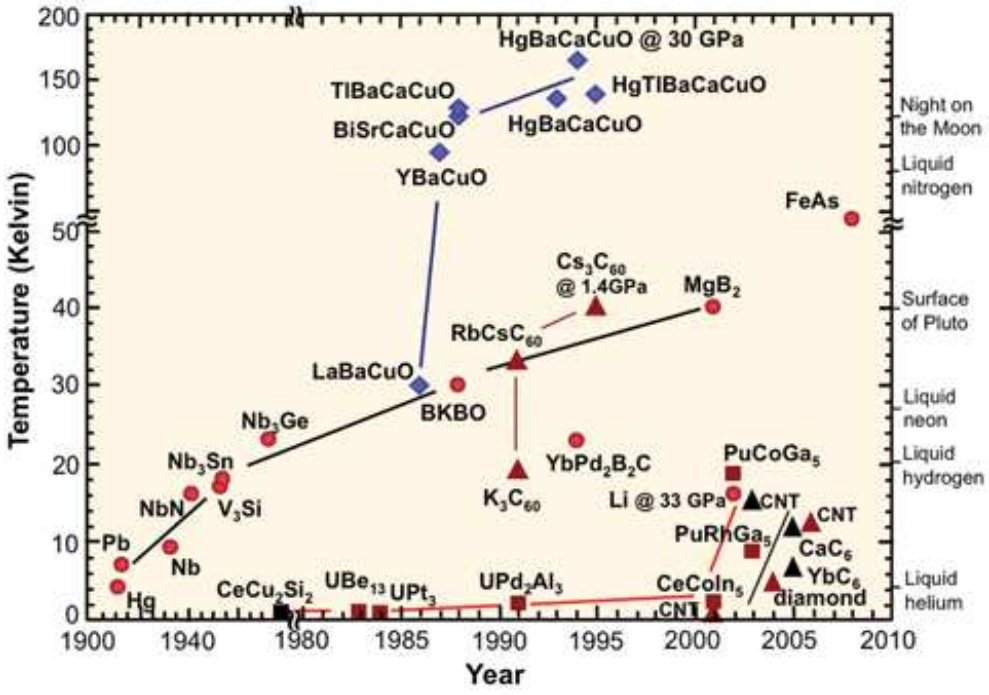

Figure 2.3: Critical temperatures and year of discovery for different superconductors [21]

copper oxide planes, called Perovskites, which have been discovered with T_cs of over 100 K. HTS are generally defined as superconductors with a T_c higher than around 23 - 30 K (30 K is the upper limit allowed by BCS theory, 23 K is the 1973 record that lasted until copper-oxide materials were discovered).

YBCO ($YBa_2Cu_3O_7$) is the most famous of these HTS and was discovered by Paul C. W. Chu and M-K. Wu in 1986 and 1987, respectively, and is known as the second generation (2G) HTS - the second HTS to be used for making conducting wires. It was the first material to superconduct above 77 K, the boiling point of liquid nitrogen, and has consequently paved the way for a much broader range of practical applications. All other materials discovered before this became superconducting at temperatures near the boiling points of liquid helium or hydrogen (4.2 K and 20 K, respectively), which are both more expensive and difficult to obtain than liquid nitrogen. YBCO also appeals to researchers because it is the cleanest and most ordered crystal - the crystalline structure of YBCO

is shown in Figure 2.4. Shown in the bottom left of this figure are the axes (or planes) of the material. The crystal structure of YBCO is highly anisotropic, with much higher conductivity within the CuO_2 than perpendicular to the planes. Thus, supercurrents flow only within the CuO_2 (a-b) planes, i.e. left to right in the figure, meaning the trapped field generated by these supercurrents is directed along the c-axis [25].

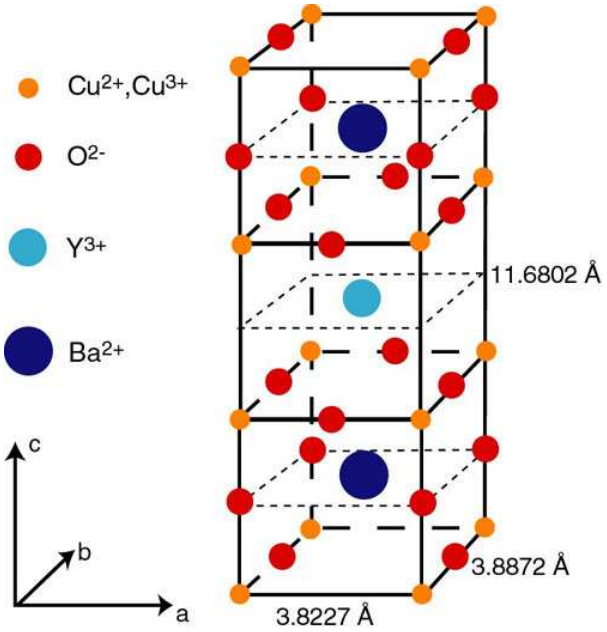

Figure 2.4: Crystalline structure of YBCO [13]

2.1.3 Commercial HTS wire

There are two main companies that supply long lengths of YBCO-based HTS tape/wire: American Superconductor (AMSC) [26] and SuperPower [27]. The manufacturing techniques differ between the two, which results in a different configuration for the final product. It is only in recent years that long lengths of wire has been available commercially, which has made it possible to wind coils and cables for large scale applications, such as electric machines, superconducting magnetic energy storage (SMES) systems, transformers, and so on.

AMSC's approach to manufacturing YBCO-based HTS wire is based on the RABiTS/MOD (rolling assisted biaxially textured substrate/metalorganic deposition) technology and an overview of this technology is shown in Figure 2.5. The buffer layers (a 75 nm Y_2O_3 seed layer, a 75 nm YSZ barrier layer and a 75 nm CeO_2 cap layer) are deposited by high-rate reactive sputtering onto a metal alloy (Ni-W) substrate, and the rare earth doped YBCO is coated onto the buffered substrate. The YBCO is capped with an Ag layer, then oxygenated, and laminated between two metallic stabliser strips, currently either brass or copper.

SuperPower's approach is based on the IBAD/MOCVD (ion beam assisted deposition/metal organic chemical vapour deposition) technology, which involves sputtering a stack of buffer layers to introduce the biaxial texture for the YBCO layer, which is deposited using MOCVD. A thin cover of silver is then sputtered to provide electrical contact. Depending on the application, this is then electroplated to completely surround the wire. The configuration of SuperPower's YBCO-based HTS wire is shown in Figure 2.6.

These two kinds of YBCO-based HTS wire are referred to in this dissertation and the coils used for testing are wound with AMSC and SuperPower wire. The terms *wire*, *tape* and *coated conductor* are used interchangeably. The large aspect ratio of the tape and its crystalline structure makes this type of superconductor highly anisotropic and the tape performance is affected greatly by magnetic fields perpendicular to the tape's wide face, i.e. perpendicular to the a-b plane.

2.2 Modelling HTS behaviour

High temperature superconductors (HTS) possess a number of unique properties that make them attractive for use in a range of engineering applications (for examples, see *Introduction*). In order to optimise the design of a system that includes superconductors, it is necessary to predict the electromagnetic behaviour of the superconductor [29]. The complexity of computing the quantitative electromagnetic properties of HTS materials is significantly increased because they are characterised by a highly non-linear current-voltage relationship.

HTS models belong to two groups: microscopic models and macroscopic models. Microscopic models aim to explain the properties of superconductors,

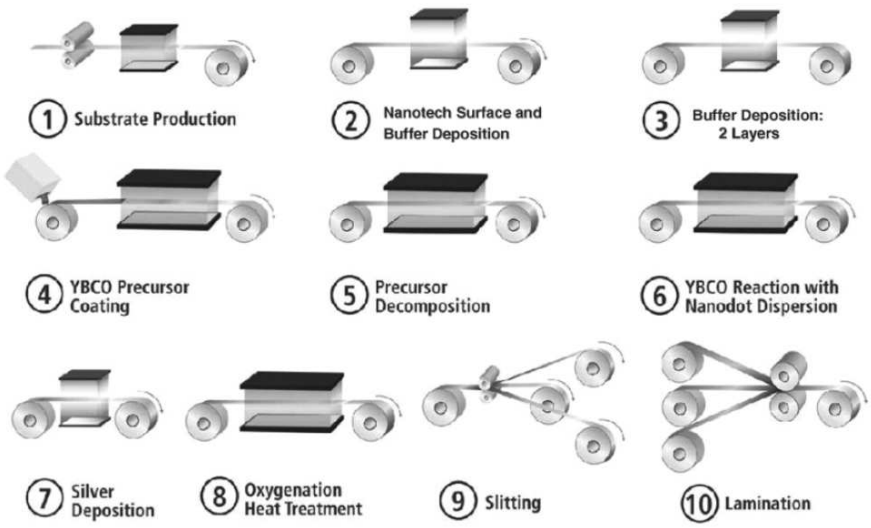

Figure 2.5: Overview of AMSC HTS wire manufacturing process [28]

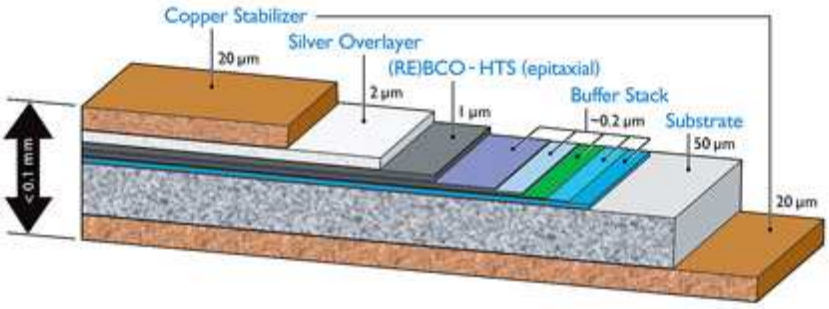

Figure 2.6: SuperPower HTS wire configuration [27]

whereas macroscopic models use simplified descriptions of these properties to predict the performance of superconducting devices [30]. Microscopic models are based around the London model, and the BCS and Ginzburg-Landau theories; macroscopic models are commonly based on critical state models, such as the Bean [31] and Kim [32, 33] models. Other macroscopic models use a non-linear current-voltage relationship, such as the E-J power-law [34], to model the superconductor as a non-linear conductor. Macroscopic models are of more interest to engineers designing large-scale devices that use superconductors, and these will be introduced in this chapter. This is because the computational effort required to solve microscopic models in the context of such applications is prohibitive.

2.2.1 Critical state models

HTS materials are type II in nature, and magnetic flux entering a type II superconductor does so in the form of discrete fluxons (or vortices). Cooper pairs, i.e. super-electrons, flow around the fluxon to shield it from the superconducting matrix. These fluxons always penetrate the sample initially from the edges of the material. Their motion inward is impeded by irregularities in the material microstructure, such as various lattice defects, non-superconducting precipitates, grain boundaries, and dislocations, which are referred to as pinning sites [35]. Without these pinning sites, the magnetisation of a type II superconductor would be reversible, and no magnetic field would be trapped within the superconductor. The magnetic field is trapped due to the interaction force between the fluxon from the pinning site, and is given by the Lorentz force. A fluxon can only pass the pinning site if the Lorentz force is greater than the pinning force. A critical state model (CSM) is often used to represent this behaviour of fluxons, which predicts different 'operating modes' for different situations.

Critical state models are based on the macroscopic behaviour of superconducting materials, derived from experimental observations of the relationship between current density and magnetic field. In these models, the outer layer of the material is said to be in a 'critical state' for a low applied current and/or magnetic field. The critical state occurs when an applied field exceeds a type II superconductor's lower critical magnetic field H_{c1}. Magnetic flux vortices with circulating

superconducting shielding currents penetrate the material to shield the interior of the material from the applied current/field. The vortices are pinned at locations of defects in the crystal lattice of the material, and the depth of penetration depends on the magnitude of the applied current/field. It should be noted here that these defects are deliberately introduced into the superconductor, e.g. secondary phase Y211 in the YBCO system.

For normal materials, current density and electric field are related by Ohm's law, but for superconductors, a different expression is required. The classical CSM introduced by Bean has been successfully used to describe the J_c of type II superconductors. The model comes from Bean's studies of ferromagnetic materials. It is important for two reasons: it introduces domain-like structure into the current density, which seems to be retained even in modified models that allow J_c to be dependent on magnetic field, and it greatly simplifies loss calculations. The CSM model is used for the calculation of J_c from magnetic hysteresis loops of classical type II superconductors - it provides approximate solutions for most simple practical cases, even for those where the critical current density depends on magnetic field [36].

The relevant Maxwell's equations, with displacement current omitted, are

$$\nabla \times \mathbf{H} = \mathbf{J} \tag{2.2}$$

$$\nabla \times \mathbf{E} = -\frac{\mathrm{d}\mathbf{B}}{\mathrm{dt}} \tag{2.3}$$

where $\mathbf{B} = \mu_0 \mathbf{H}$, which is a good approximation for practical applications where $H_{c1} < \mathbf{H} < H_{c2}$ [37], and $\nabla \cdot \mathbf{J} = 0$ as there are no time-varying free charge distributions.

Where there is a current flowing in the superconductor, the magnetic field vortices experience a Lorentz force $\mathbf{F} = \mathbf{J} \times \mathbf{B}$. For a large enough Lorentz force, the vortices become de-pinned and move in the direction of the force with velocity $\mathbf{v}$. This vortex movement induces an electric field $\mathbf{E} = \mathbf{B} \times \mathbf{v}$, and $\mathbf{E}$ is parallel to $\mathbf{B} \times (\mathbf{J} \times \mathbf{B})$. If $\mathbf{B}$ is perpendicular to $\mathbf{J}$, which is always true for 2D models,

then **E** is parallel to **J**. Thus,

$$\mathbf{E} = \rho(\mathrm{J})\mathbf{J} \tag{2.4}$$

where $\rho(\mathrm{J})$ is a highly non-linear function for the region inside the material and $\mathrm{J} = |\mathbf{J}|$. The equation above is analogous to Ohm's law for conventional materials. All CSMs state that the current density in the superconductor cannot exceed the critical value $\mathrm{J_c}$.

2.2.1.1 Bean model

Bean's model [31] is the simplest of all CSMs and it states that the magnitude of the superconductor's current density takes values of either 0 or $\pm\mathrm{J_c}$, the critical current density. It assumes a non-vanishing electric field with current density in the direction of the electric field. Furthermore, the current density is only zero in regions of the superconductor that have never experienced an electric field. When the whole superconductor is penetrated with $\pm\mathrm{J_c}$, the superconductor is in a critical state.

When applying an external field, the field begins to penetrate at the boundary of the superconductor. The penetration depth depends on the value of the external field and $\mathrm{J_c}$. Without vortex pinning, $\mathrm{J_c} = 0$, and any external field fully penetrates the superconductor in the form of moving vortices. With vortex pinning, a gradient of vortex density is maintained by the pinning, and this gradient defines $\mathrm{J_c}$.

Thus, we have two main assumptions for the Bean model:

1. The electric field **E** is parallel to the current density **J**
2. The critical current $\mathbf{J_c}$ flows wherever the material is in the critical state

   $\mathrm{J(x)} = \pm\ \mathrm{J_c}$ if $|\mathrm{E(x)}| \neq 0$

   $\mathrm{J(x)} = 0$ if $|\mathrm{E(x)}| = 0$

If a superconductor is carrying an AC current, the current distribution at the peak AC current is the same as it would be for the same value of DC current. When the transport current or external field producing the shielding currents is

large enough, the current 'sheath' reaches the centre of the superconductor. This is called "full penetration." Losses differ below and above full penetration, and depend on the direction of the applied fields.

As an example, a superconducting slab in an externally applied magnetic field is considered in Figure 2.7. A superconducting slab of thickness 2a is oriented in the y-z plane with an external magnetic field B_0 applied in the z direction. The induced shielding current density J_y flows in the y direction inside the front and back faces [15]. The Bean model for this scenario for different states is shown in Figure 2.8. In this figure, B^* is the characteristic field [15] or full-penetration field, and is given by $B^* = \mu_0 J_c a$ for a wire of radius a. The model can be applied in the same way for transport current, and for both a magnetic field and transport current, the individual solutions for the screening current and transport current can be superposed.

Kim [32] and Anderson [33] modified this model to allow the current density in the critical state to vary with the local magnetic field. This is discussed in detail in the following section describing factors affecting J_c.

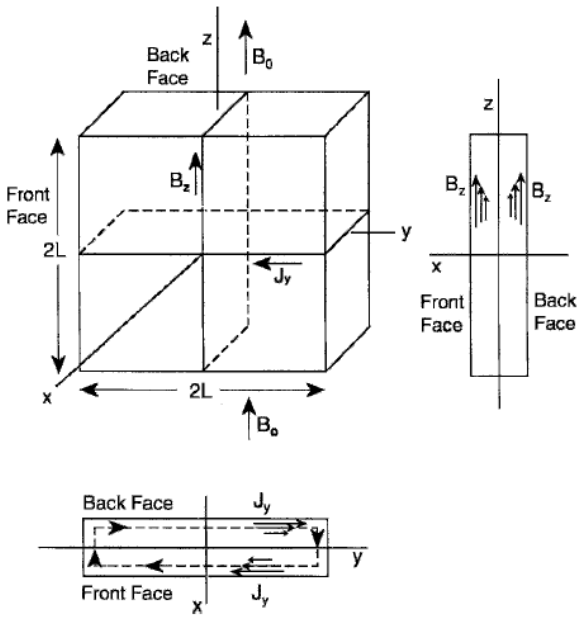

Figure 2.7: Superconducting slab in externally applied magnetic field example [15]

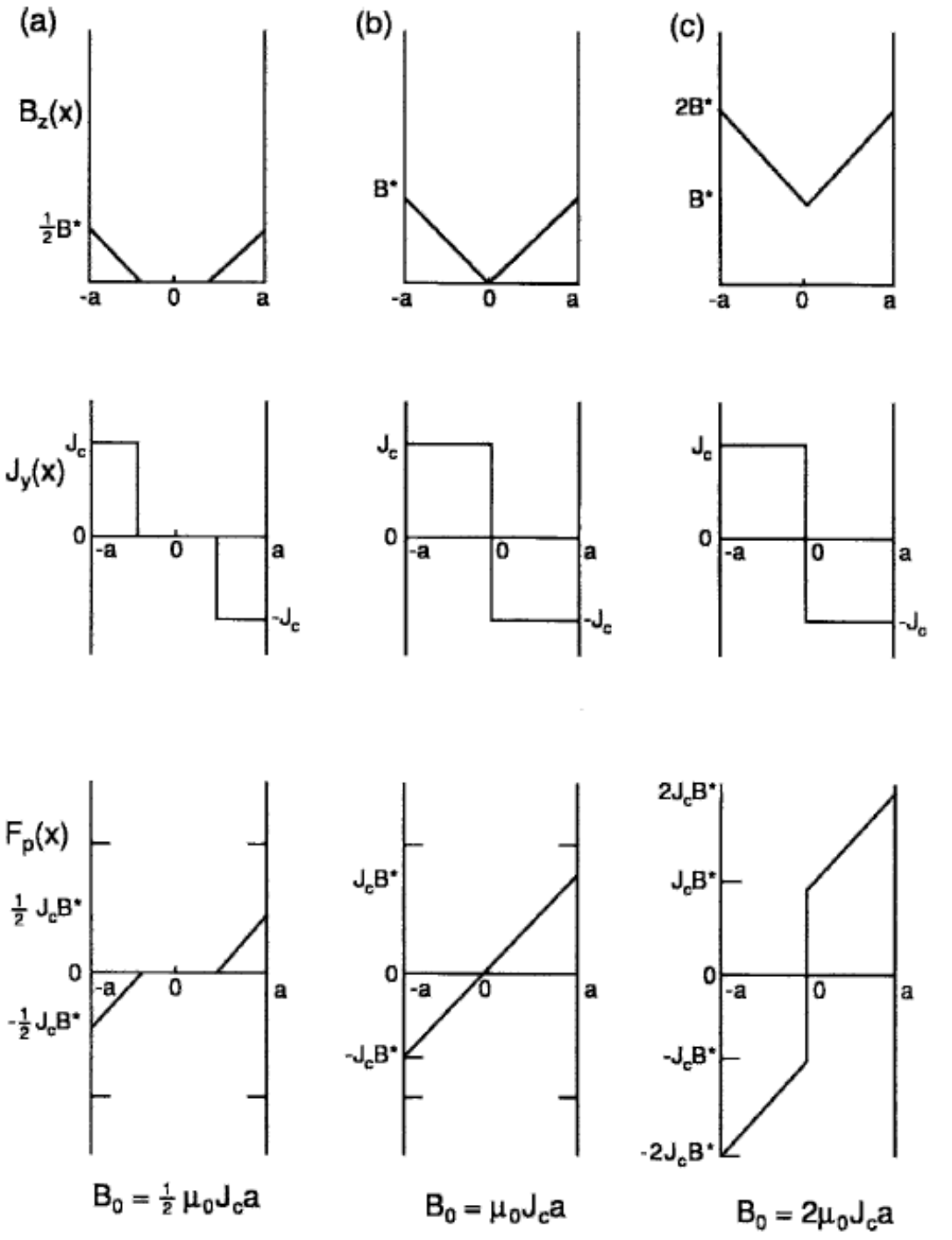

Figure 2.8: Dependence of the internal magnetic field $B_z(x)$, current density $J_y(x)$, and pinning force $F_p(x)$ on strength of applied magnetic field B_0 for normalised applied fields given by (a) $B_0/\mu_0 J_c a = 1/2$, (b) $B_0/\mu_0 J_c a = 1$, and (c) $B_0/\mu_0 J_c a = 2$ using the Bean model [15]

2.2.1.2 Superconducting strip model

Brandt [38, 39] realised that while the Bean model was applicable to long superconductors in a parallel field where demagnetisation effects were negligible, most practical experiments used flat superconductors in a perpendicular field, for which demagnetising effects are crucial. He produced an analysis of superconducting strips in perpendicular magnetic fields and/or carrying transport currents, and a summary of the results of the analysis are presented below. The superconducting strip is a good approximation for the superconducting layer in a superconducting coated conductors, and these results are often used as a basis to compare the results of finite element method (FEM) models, which are described later in this chapter.

For a strip of width 2a (x axis) and thickness d (y axis) in a perpendicular magnetic field (perpendicular to the tape width) with magnitude H_0, Brandt [39] shows that the flux penetrates from the edges such that

$$\begin{aligned} J(x) &= \frac{2J_c d}{\pi} \arctan\left(\sqrt{\frac{a^2-b^2}{b^2-x^2}}\left(\frac{x}{a}\right)\right) && \text{for } |x| < b \\ &= J_c d && \text{for } b < |x| < a \end{aligned} \tag{2.5}$$

where b is the pentration depth and is given by

$$b = \frac{a}{\cosh\left(\frac{\pi H_0}{J_c d}\right)} \tag{2.6}$$

The magnetic field strength along the tape is

$$\begin{aligned} H(x) &= 0 && \text{for } |x| < b \\ &= H_c \arctan\left(\sqrt{\frac{x^2-b^2}{a^2-b^2}}\left(\frac{a}{|x|}\right)\right) && \text{for } b < |x| < a \end{aligned} \tag{2.7}$$

where H_c is the characteristic field, given by $H_c = \frac{J_c d}{\pi}$.

The results are significantly different from that of Bean's 'slab' in that the flux penetration in the Bean model is linear, whereas in the superconducting strip,

the flux penetration is initially quadratic. Additionally, the penetrating flux front has a vertical slope, but in the Bean model it is constant and finite. When the flux has partly penetrated and a critical state with $J = J_c$ is established near the edges of the strip, the current flow is over the entire width of the strip to shield the central flux-free region, but in the Bean model the flux-free region is current free. The screening current density is a continuous function with a vertical slope at the flux front where it reaches J_c, but in the Bean model it is a piecewise constant function.

For a transport current with magnitude I_0, we have

$$\begin{aligned} J(x) &= \frac{2J_c d}{\pi} \arctan\left(\sqrt{\frac{a^2 - b^2}{b^2 - x^2}}\right) && \text{for } |x| < b \\ &= J_c d && \text{for } b < |x| < a \end{aligned} \tag{2.8}$$

where the total current I_0 is

$$I_0 = 2J_c d\sqrt{a^2 - b^2} \tag{2.9}$$

and b is the penetration depth, given by

$$b = a\sqrt{1 - \left(\frac{I_0}{I_c}\right)^2} \tag{2.10}$$

with critical current $I_c = 2aJ_c d$.

The magnetic field strength along the tape is

$$\begin{aligned} H(x) &= 0 && \text{for } |x| < b \\ &= \frac{H_c x}{|x|} \operatorname{arctanh}\left(\sqrt{\frac{x^2 - b^2}{a^2 - b^2}}\right) && \text{for } b < |x| < a \end{aligned} \tag{2.11}$$

where H_c is the characteristic field, given by $H_c = \frac{J_c d}{\pi}$.

The AC loss calculation for each of these cases (perpendicular applied magnetic field and transport current) will be presented in a following section on AC loss.

2.2.2 E-J power law

Bean's model assumes a step relationship between the current density and electric field in the superconductor, based on the existence of a well-defined value for the critical current density as a function of the magnetic field. This is applicable to LTS and some HTS, for which Bean's CSM has proven very successful [34]. However, there exist HTS materials where the critical current is ill-defined. Anderson [33] proposed flux creep theory where this relationship is not discontinuous. In this theory, flux moves slowly, due to thermal activation, at currents lower than the critical current, then an electric field appears and losses occur. Rhyner [34] proposed the following E-J power law, which is commonly used to model the non-linear behaviour

$$\mathrm{E} = \mathrm{E}_0 \left(\frac{\mathrm{J}}{\mathrm{J}_0} \right)^{\mathrm{n}} \tag{2.12}$$

This model fits well to the experimental I-V curves for DC for many HTS materials, and n is a particular characteristic of the HTS dependent on the material properties and its microstructure. The extreme cases of $\mathrm{n} = 1$ and $\mathrm{n} = \infty$ correspond to the linear Ohm's law ($\mathbf{E} = \rho\ \mathbf{J}$) and Bean's model ($\mathbf{J}$ is either zero or $\mathbf{J_c}$), respectively. $\mathrm{n} = 5$ corresponds to a superconductor with strong flux creep, $\mathrm{n} = 15$ for weak flux creep, and $\mathrm{n} = 50$ is the limiting value between HTS and LTS values [37]. For $\mathrm{n} > 20$, it becomes a good approximation of Bean's CSM model. The E-J relationship implied by Bean's model ($\mathrm{n} = \infty$) and the power-law model are shown in Figure 2.9. $\mathrm{J_c}$ is the measured current for a given electrical field, usually $\mathrm{E}_0 = 10^{-4}$ V/m.

2.2.3 Kim model (magnetic field dependency of $\mathrm{J_c}$)

The magnitude of the critical current density $\mathrm{J_c}$ is fixed by the characteristics of the particular superconductor, and depends on factors such as the type of material, granularity, twinning, concentration of defect centres, and so on, which can be referred to as 'internal' factors [15]. As shown previously in Figure 2.1, the critical current density $\mathrm{J_c}$ is dependent on temperature and magnetic field. The I-V relationship of some type II superconductors also depends heavily on strain,

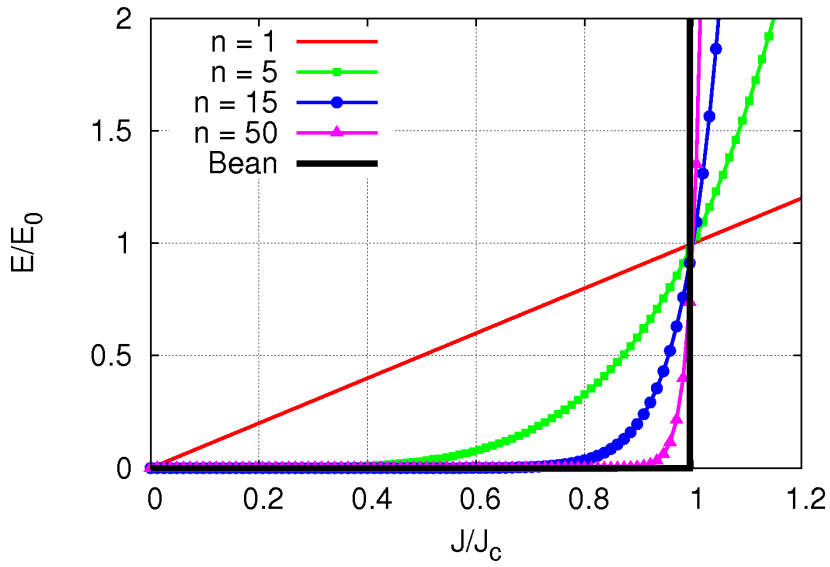

Figure 2.9: The power-law model from n = 1 (linear) to n = ∞ (Bean's model)

which occurs when a superconductor is twisted or bent, as in superconducting cables, motor/generator coils, and so on. These three factors - temperature, magnetic field and strain - can be referred to as 'external' factors. Material scientists try to optimise the internal factors, whilst engineers try to optimise the external factors. Here we introduce the magnetic field dependency of J_c that will be used in this dissertation. Therefore, it assumed that the temperature of the coil remains constant, i.e. the rate of heat production generated by losses is exactly balanced by the rate of heat removal, no parts of the coil quench for the currents applied, and that the superconductor properties are not affected by strain.

Kim [32] and Anderson [33] showed that the critical current in type II superconductors exhibit a strong dependence on temperature, as well as local magnetic field. This empirical relationship is given by

$$J_c(B) = \frac{\alpha(T)}{B_0 + B} = \frac{J_{c0}(T)}{1 + \frac{B}{B_0}} \tag{2.13}$$

where B_0 is a constant dependent on the material, and $J_{c0} = \frac{\alpha(T)}{B_0}$. A depen-

dence of α with temperature was also proposed:

$$\alpha = \frac{1}{\mathrm{d}}(\mathrm{a} - \mathrm{bT}) \tag{2.14}$$

where d depends strongly on the physical microstructure of the material and $\frac{\mathrm{a}}{\mathrm{b}} \leq \mathrm{T_c}$. The B-dependency of the critical current density and the power index n can be written as [40]

$$\mathrm{J_c(B)} = \frac{\mathrm{J_{c0}}}{1 + \frac{|\mathrm{B_y}|}{\mathrm{B_0}}} \tag{2.15}$$

$$\mathrm{n(B)} = \frac{\mathrm{n_{c0}}}{1 + \frac{|\mathrm{B_y}|}{\mathrm{B_0}}} \tag{2.16}$$

where only the y-component of B (parallel to the c-axis) is considered, as the contribution to AC loss from a perpendicular field is much greater than that of a transverse/parallel field [41]. $\mathrm{J_{c0}}$ and $\mathrm{n_{c0}}$ are the critical current density and power index in self-field, i.e. when there is no externally applied magnetic field. $\mathrm{B_0}$ is obtained from the $\mathrm{I_c}$-$\mathrm{B_{DC}}$ experimental curve. This formulation leads to a more accurate model of HTS electromagnetic behaviour, particularly for models where both an applied current and magnetic field exist.

As described in [42] and [43], the Kim model above can be extended using the factor k and a common denominator $\mathrm{B_0}$ to provide an equation for the critical current density when the superconductor is subjected to a combination of parallel and perpendicular magnetic field components.

$$\mathrm{J_c}(|\mathrm{B_x}|, |\mathrm{B_y}|) = \frac{\mathrm{J_{c0}}}{1 + \frac{\sqrt{\mathrm{k^2}|\mathrm{B_x}|^2 + |\mathrm{B_y}|^2}}{\mathrm{B_0}}} \tag{2.17}$$

This was recently extended in [44] and [45] to obtain the angular and field dependence of the critical current density, i.e. $\mathrm{J_c(B}, \theta)$.

In this dissertation, a critical current density that is either constant or dependent on the perpendicular magnetic field $\mathrm{B_y}$ is used. A regression can be performed on the manufacturer-supplied data to find the coefficients k and $\mathrm{B_0}$. For example, for the AMSC tape used in the stator coils of the motor described previously $\mathrm{B_0} = 0.23$ T, based on the data shown in Figure 2.10. Therefore, the

J_c can be described by

$$J_c(|B_{perp}|, 77K) = \frac{J_{c0}}{1 + \frac{|B_{perp}|}{0.23}} \tag{2.18}$$

For SuperPower tape, $B_0 = 0.12$ T, based on the data shown in Figure 2.11. Therefore, the J_c can be described by

$$J_c(|B_{perp}|, 77K) = \frac{J_{c0}}{1 + \frac{|B_{perp}|}{0.12}} \tag{2.19}$$

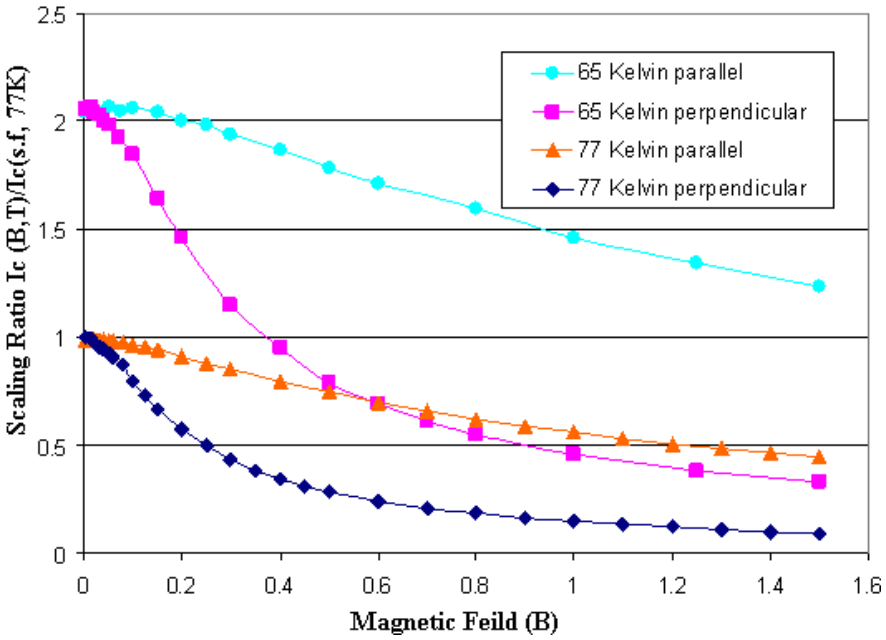

Figure 2.10: AMSC data showing critical current change for parallel and perpendicular magnetic fields

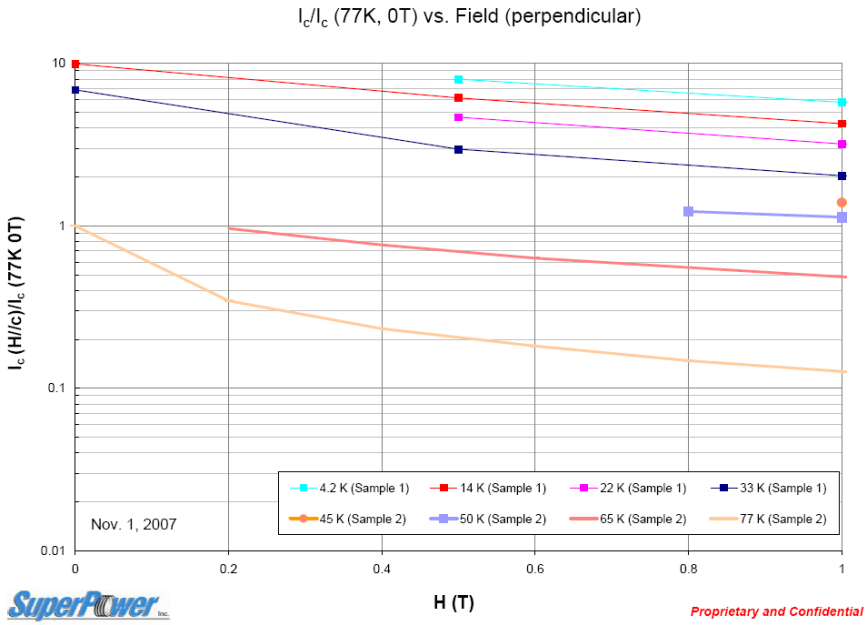

Figure 2.11: SuperPower data showing critical current change for perpendicular magnetic fields

2.3 AC Loss in HTS conductors

2.3.1 AC loss in superconductors

At low frequencies, typical of electrical power applications, resistance arises in ordinary type II superconductors because of flux flow and flux creep. Type II superconductors are of much more technological interest since they can carry more current in larger magnetic fields. However, type II superconductors have losses because electric fields can be produced inside [36].

As mentioned previously, superconductors have to meet several requirements in order to compete with the presently used normal conductors, including a high critical current and a low $/kAm price. In addition, the AC loss should be low enough to justify the extra investment in the superconductor and the cooling equipment. The decision to utilise superconductors in electrical power devices is usually based on financial considerations: energy costs, superconducting material costs, cooling system costs, and maintenance and reliability [46].

The AC loss in a superconductor is usually much lower than the resistive loss in a normal conductor under the same circumstances. However, accurate calculation and measurement and, if possible, minimisation of the AC loss is technically important because the AC loss is dissipated as heat in a low temperature environment [46]. This dissipation leads to evaporation of the coolant or an increased thermal load on the refrigeration/cooling system. The heat produced at low temperatures translates to a much higher 'room temperature' loss, as described in Chapter 3. The use of HTS over LTS greatly reduces the problem of heat removal, due to the higher operating temperature, but does not completely eliminate it. In the case of a superconducting machine, the superconductor and the coil/windings need to be designed such that the size and weight gains realised by using superconductors are not diminished by the requirement of a large cooling system [47].

Calculating the AC loss of a superconductor allows for more detailed design of applications that make use of superconductors, and by comparing experimental data with theoretical values, the completeness of that theory can be checked. Each potential electrical power application of superconductivity needs to be evaluated separately as different devices see different time-varying currents and/or magnetic fields. AC losses can generally be split into two categories - magnetisation loss and transport current loss - depending on the source that provides the energy [48]. Both of these losses can be present in superconducting applications.

2.3.2 AC loss types

The two types of AC loss in superconductors are described below.

Magnetisation loss Q_m is the power dissipated in the superconductor when an alternating magnetic field, B, is applied to the superconductor. The energy comes from source of the magnetic field.

Transport current loss Q_t is the power that is delivered by the power supply that enables a transport current, I, to flow through the superconductor. The voltage, V, along the sample is a measure for the dissipated power.

The total power dissipated is $Q_{total} = Q_m + Q_t$.

2.3.2.1 Magnetisation loss

There are three types of loss that make up the total magnetisation loss: hysteresis loss, coupling loss and eddy current loss.

Hysteresis loss Hysteresis losses are a result of irreversibility caused by vortex pinning [36]. These losses are called hysteresis losses because the flux that has entered the superconductor does not leave precisely in the same manner by which it entered due to this pinning. If one plots the magnetic induction, B, versus the magnetic field, H, a hysteresis loop is obtained, which is traversed once per cycle. The energy loss per cycle is proportional to the area of this loop, provided that no transport currents are flowing [48]. Such hysteresis losses are dissipated as heat. The loss becomes higher for stronger pinning; thus, the larger the critical current of a hard type II superconductor, the larger are the hysteretic losses [35]. An example of a hysteresis (or magnetisation) loop is shown in Figure 2.12.

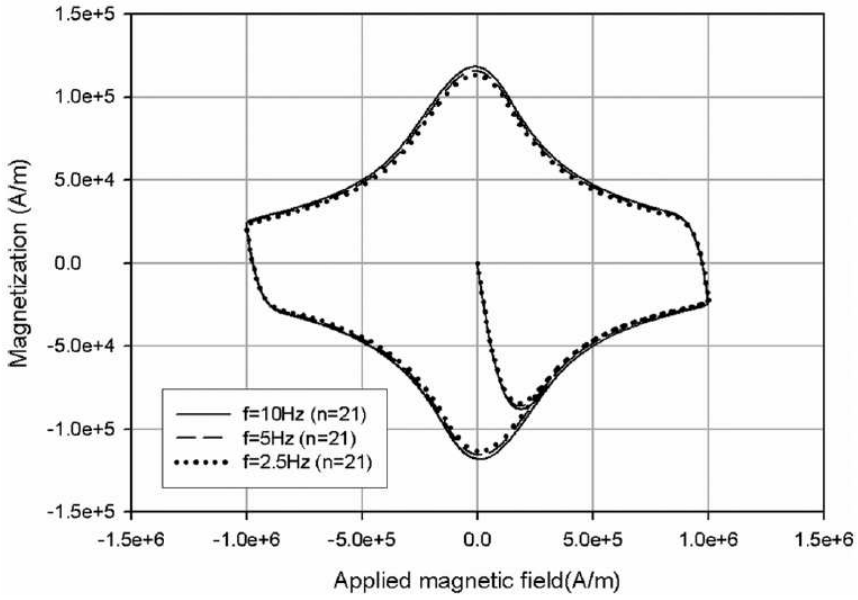

Figure 2.12: Magnetisation loop for a full cycle of applied field [49]

Coupling loss Coupling loss can be a significant problem in multifilamentary conductors, such as BSCCO (Bi-Sr-Ca-Cu-O), which consists of multiple superconducting filaments within a silver sheath [48, 50]. It can also be a problem in YBCO conductors if the tapes are striated into filaments (striation is discussed in detail in Chapter 5 when discussing AC loss mitigation). An eddy current induced by a varying magnetic field, flows partly through the superconductor and also through the silver between the filaments. When currents flow from one filament to another, they can couple the filaments together into a single large magnetic system, which encounters a resistance along the current path through the silver matrix. This ohmic loss in the metal matrix is often called the coupling loss [48].

Eddy current loss When an external time-varying magnetic field penetrates into a normal conductor, it induces a changing electric field, which in turn causes currents to flow [36]. These are known as eddy currents. Due to eddy currents in the tape, the ohmic energy dissipation can be significant if the magnetic field is perpendicular to the tape [36]. At low frequencies the eddy-current loss can be calculated for many conductor geometries. The basic approach to reducing the eddy current losses is increasing the effective resistivity of the matrix. For the calculations in this research, it is assumed (unless otherwise stated) that the superconductor-related losses are dominant and other losses are ignored.

2.3.2.2 Transport current loss

Hysteresis loss When there is an alternating transport current flowing through the superconductor, a hysteresis loss (similar to that described above for magnetisation loss) occurs. The self-field of the superconductor plays the role of the applied field, and the energy of the self-field must be supplied by the source of the transport current [48].

Flux flow loss When the transport current increases, more and more flux lines are depinned and will move in the superconductor. The energy dissipated associated with this process is called flux flow loss [48]. Initially, the self-field

dominates, but for increasing transport current, the flux flow loss contribution becomes significant.

2.3.3 AC loss calculation using the CSM

The AC loss in a superconductor can be calculated using different methods; the basic formulation is based on the Poynting vector ($\mathbf{E} \times \mathbf{H}$). The energy loss per unit volume per field cycle in J/cycle/m^3 in a volume V enclosed by a surface S is given by

$$\mathrm{Q} = \frac{1}{\mathrm{V}} \int_0^{1/\mathrm{f}} \int_{\mathrm{S}} (\mathbf{E} \times \mathbf{H}) \cdot \mathbf{n} \, \mathrm{dS} \, \mathrm{dt} \tag{2.20}$$

Due to the non-linear voltage-current relationship, the magnetic behaviour of the superconductor is hysteretic, just as in ferromagnetic materials. The magnetisation curve encloses an area that represents the magnetisation loss per unit volume per field cycle. In this case, the loss can be described by an equation that is derived from the above equation, where $\mathbf{M}$ is the magnetisation of the superconductor.

$$\mathrm{Q} = \oint_{\mathrm{B}} \mathbf{M} \cdot \mathrm{d}\mathbf{B} \tag{2.21}$$

The AC loss can also be calculated using an electric method. An electric field is induced by an applied time-varying magnetic field. A screening current begins to flow and there is a local non-zero product of voltage and current. The product $\mathbf{E} \cdot \mathbf{J}$ is integrated spatially over the conductor cross-sectional area and with respect to time over the magnetic field cycle yields to give the loss (again per unit volume per field cycle in J/cycle/m^3).

$$\mathrm{Q} = \frac{1}{\mathrm{S}} \int_0^{1/\mathrm{f}} \int_{\mathrm{S}} \mathbf{E} \cdot \mathbf{J} \, \mathrm{dS} \, \mathrm{dt} \tag{2.22}$$

The applied magnetic field is $\mathbf{B} = \mu_0 \, (\mathbf{H} + \mathbf{M})$. If the value of the magnetic field is taken at a considerable distance from the superconductor, where the influence of the screening currents in the superconductor is negligible, and $\mathbf{B} = \mu_0 \, \mathbf{H}$. If the applied magnetic field is larger than the lower critical magnetic field

H_{c1}, then the Meissner state can be ignored.

In order to solve Maxwell's equations in superconductors with analytical methods, several assumptions need to be made. The flux penetration in a superconductor is described by the CSM [31] with the non-linear voltage-current relation

$$\mathbf{J} = J_c \frac{\mathbf{E}}{|E|} \text{ if } \mathbf{E} \neq 0 \tag{2.23}$$

This is the reason for a superconductor's electromagnetic behaviour. The current density induced in the superconductor by an alternating magnetic field is J_c, the critical current density, irrespective of the value of the electric field. The direction of the induced current depends on the direction of the last non-zero electric field. In the special case, $\mathbf{E} = 0$, the current density depends on history. For example, $\mathbf{J} = 0$ in regions where the electric field has been zero since the conductor was cooled below T_c.

For an infinite slab (infinite length and height, but finite thickness), the magnetic field profile, following from Ampere's law, is

$$\nabla \times \mathbf{B} = \mu_0 \mathbf{J} \Rightarrow \frac{dB_y}{dx} = \mu_0 J_z = \mu_0 J_c \tag{2.24}$$

where J_c has only a z component. The profile is one-dimensional in the cross-section because the derivatives in the y and z directions are zero.

Figure 2.13 shows the field profile and current density distribution in a slab for an applied magnetic field that is ramped up to a value B_a from a virgin state. In the CSM description, a current density with magnitude J_c starts to flow in the superconductor and the interior of the slab is shielded from the applied magnetic field. An applied magnetic field that just penetrates to the centre of the superconductor is called the 'full penetration field.' The whole cross-section is filled with current, from Ampere's law ($B_p = \mu_0 J_c d$). A further increase in the applied field will result in a non-zero field, even in the centre of the slab. The field profile will remain the same, but will shift upwards. The difference between the field at the surface of the slab and in the centre remains B_p.

Bean's model [31] gives the E-J characteristics for the superconductor and assumes that the magnitude of the current density is a constant J_c. Since $\mathbf{E}$ and

J are parallel, equation 2.22 can be rewritten:

$$P = \int_V J_c \cdot E \, dV \tag{2.25}$$

An example of using Bean's model to calculate the AC loss of a superconducting slab is provided in Appendix 1 for reference.

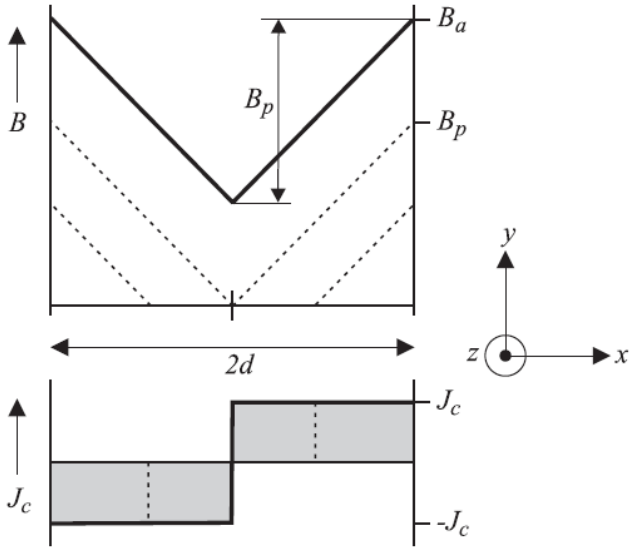

Figure 2.13: Field profile and current density distribution in an infinite slab exposed to a magnetic field [48]

2.3.4 Analytical techniques

The equations presented here for transport current and magnetisation AC loss can be used as a basis to check the accuracy of the AC loss calculation using FEM techniques.

2.3.4.1 Norris

In 1969, Norris proposed an analytical method to estimate the AC loss for a self-field [51]. This is based on the London model [8] that assumes idealised behaviour. The resistance is assumed to rise very steeply as the current tries to increase above

the critical value and the resistance is such that the ohmic voltage drop exactly balances the driving emf with the current density remaining constant. It assumed that the current density is independent of the ambient magnetic field - although it is well known that the critical current depends not only on the magnitude, but also the direction of the field.

For a superconducting strip carrying a transport current with magnitude I_0, the transport AC loss can be computed as [51]

$$P_{strip}\ [W/m] = \frac{\mu_0 I_c^2 f}{\pi}\ [\ (1-\frac{I_0}{I_c})\ln(1-\frac{I_0}{I_c}) + (1+\frac{I_0}{I_c})\ln(1+\frac{I_0}{I_c}) - (\frac{I_0}{I_c})^2\ ] \tag{2.26}$$

A simple graph of the change in AC loss for a thin strip of finite width for different frequencies and ratios of transport current to critical current is shown in Figure 2.14.

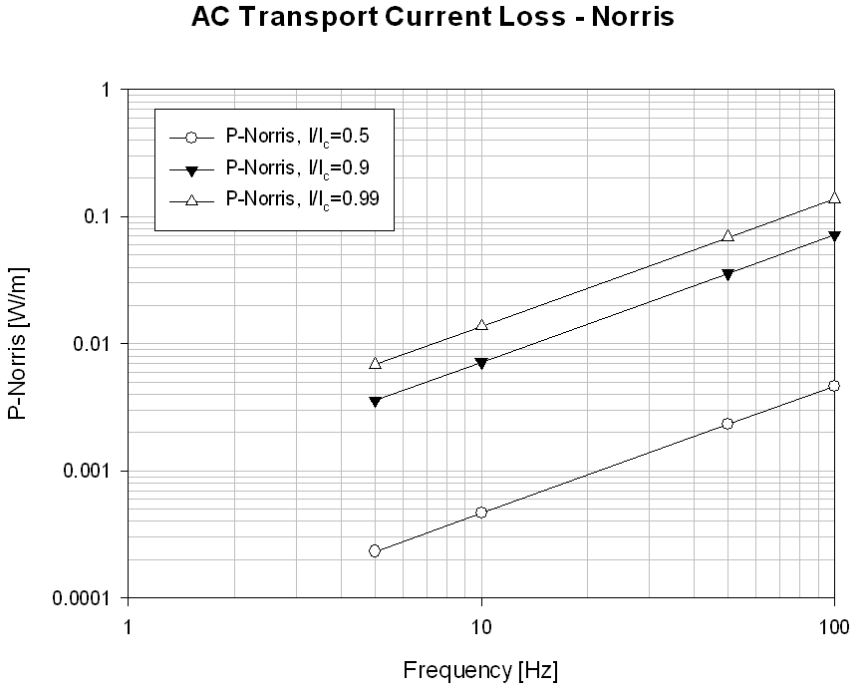

Figure 2.14: AC loss calculation using Norris's equation for thin strip of finite width

2.3.4.2 Brandt

Brandt introduced a widely used method to compute AC losses in two dimensions, which is based on solving Maxwell's equations together with the E-J power law to calculate the AC loss for a superconducting strip for a transport current and/or a perpendicular external magnetic field [38, 39].

The equations for the current and magnetic field distributions were presented earlier in this chapter (see *Superconducting strip model*). For a strip of width 2a and thickness d in a perpendicular magnetic field with magnitude H_0, the previous equations can be used to compute the magnetisation loss:

$$P_{mag}\ [W/m] = 4\pi\mu_0 a^2 H_0 H_c f\ [\ \frac{2H_c}{H_0}\ \ln\cosh(\frac{H_0}{H_c}) - \tanh(\frac{H_0}{H_c})\ ] \tag{2.27}$$

For a transport current with magnitude I_0, the previous equations can be used to compute the transport loss:

$$P_{trans}\ [W/m] = \frac{\mu_0 I_c^2 f}{\pi}\ [\ (1-\frac{I_0}{I_c})\ln(1-\frac{I_0}{I_c}) + (1+\frac{I_0}{I_c})\ln(1+\frac{I_0}{I_c}) - (\frac{I_0}{I_c})^2\ ] \tag{2.28}$$

which is the same as the Norris equation stated above.

Chapter 3

Modelling HTS-based superconducting coils

In this chapter, the modelling of HTS-based superconducting coils using the finite element method is described in detail, including the evolution of the development of the coil model as the research in this dissertation has progressed. Often there is a compromise in computer modelling between the accuracy of the solution and the computational time required, and a number of different models are compared to examine the optimum parameters. Firstly, the numerical model used in this thesis is described, which is based on solving a set of Maxwell's equations in 2D implementing the H formulation using the commercial software package Comsol Multiphysics. The coil cross-section is modelled as the number of individual turns in the coil, and an artificial expansion technique is investigated to improve the computational speed of the model, which can require hundreds of thousands of mesh elements. Different methods to approximate the critical current density J_c *are also discussed. A technique that allows the real superconducting layer thickness to be modelled, using a mapped mesh, is then investigated, and the model is modified to include the magnetic substrate present in some superconducting tapes. This investigation raises some interesting points for further analysis, and a detailed investigation on stacks of superconducting tapes with both weak and strong magnetic substrates is carried out at the end of the chapter.*

3.1 Finite element method (FEM) models

Several numerical methods have been proposed to solve the critical state in superconductors, and analytical methods have been developed for simple geometries and uniform field conditions, as described in the previous chapter. For more complicated shapes and field conditions, numerical methods must be developed. These numerical methods usually make use of the finite element method (FEM) or the finite difference method to solve Maxwell's equations, coupled with the E-J power law, in 2D or 3D, and FEM is a popular technique for solving partial differential equations (PDEs). These methods can be classified by the main equations used: the **A**-V (based on the magnetic vector potential **A**) [37, 52–54], **T**-Ω (based on the current vector potential **T**) [55], **E** (based on the electric field **E**) [56–58], and **H** (based on directly solving the magnetic field components) [29, 59–61] formulations. Maxwell's equations can be written in each of these formulations and these formulations are equivalent in principle, but the solutions of the corresponding PDEs can be very different [62].

3.1.1 The H formulation

The numerical model used in this thesis for modelling the electromagnetic behaviour of HTS is based on solving the set of Maxwell's equations in 2D implementing the **H** formulation using the software package Comsol Multiphysics, version 3.5a. Methods based on the **H** formulation can converge more easily than other methods and it is easy to impose boundary conditions related to the current flowing in the superconductor(s) and/or externally applied magnetic fields.

The space is typically divided into two subdomains: the superconducting region(s) and air. The addition of magnetic materials, e.g. the magnetic substrate found in certain coated conductors, will be discussed in a later section. A set of PDEs, sharing the same dependent variables, is defined in each subdomain. By assuming that the constitutive law $\mathbf{B} = \mu_0\ \mathbf{H}$ is applicable in both the air and superconducting regions, the relevant Maxwell's equations are

$$\nabla \times \mathbf{E} = -\frac{\mathrm{d}\mathbf{B}}{\mathrm{dt}} = -\mu_0 \frac{\mathrm{d}\mathbf{H}}{\mathrm{dt}} \tag{3.1}$$

$$\nabla \times \mathbf{H} = \mathbf{J} \tag{3.2}$$

The E-J behaviour of the superconducting material is modelled assuming

- The electric field **E** is always parallel to the current density **J**
- The power-law relationship: $\mathbf{E} = \mathrm{E_0} \left(\frac{\mathrm{J}}{\mathrm{J_c(B)}}\right)^{\mathrm{n-1}} \frac{\mathbf{J}}{\mathrm{J_c}}$ where $\mathrm{E_0}$ denotes the threshold electric field used to define the critical current density $\mathrm{J_c}$, usually 10^{-4} V/m

Using the power-law model is more suitable than the original Bean model where $\mathrm{n} \to \infty$, and a voltage criterion $\mathrm{E_0} = 1\ \mu$V/cm and constant $\mathrm{n} = 21$ is assumed, which are typical values for melt-processed YBCO [63].

3.1.1.1 H formulation in cartesian coordinates

In this two dimensional model, the space is assumed to be infinitely long in the z direction and the sample is assumed to consist of an infinitely long tape of rectangular cross section w × d. The magnetic flux lies in the xy plane, and the current density **J** flows in the z direction only. A visual description of the model is shown in Figure 3.1.

Thus, Maxwell's equations become

$$\mathrm{J_z} = \frac{\mathrm{dH_y}}{\mathrm{dx}} - \frac{\mathrm{dH_x}}{\mathrm{dy}} \tag{3.3}$$

$$-\frac{\mathrm{dE_z}}{\mathrm{dx}} = -\mu_0 \frac{\mathrm{dH_y}}{\mathrm{dt}} \tag{3.4}$$

$$\frac{\mathrm{dE_z}}{\mathrm{dy}} = -\mu_0 \frac{\mathrm{dH_x}}{\mathrm{dt}} \tag{3.5}$$

Using these two PDEs defined above with the two dependent variables $\mathrm{H_x}$ and $\mathrm{H_y}$, and applying suitable boundary conditions, Comsol can be used to solve the problem. The subdomain settings for 'PDE, General Form (g)' in Comsol, which is appropriate for non-linear PDEs, follows the following convention:

$$\mathrm{e_a}\frac{\mathrm{d}^2\mathbf{u}}{\mathrm{dt}^2} + \mathrm{d_a}\frac{\mathrm{d}\mathbf{u}}{\mathrm{dt}} + \bigtriangledown \cdot \Gamma = \mathrm{F} \tag{3.6}$$

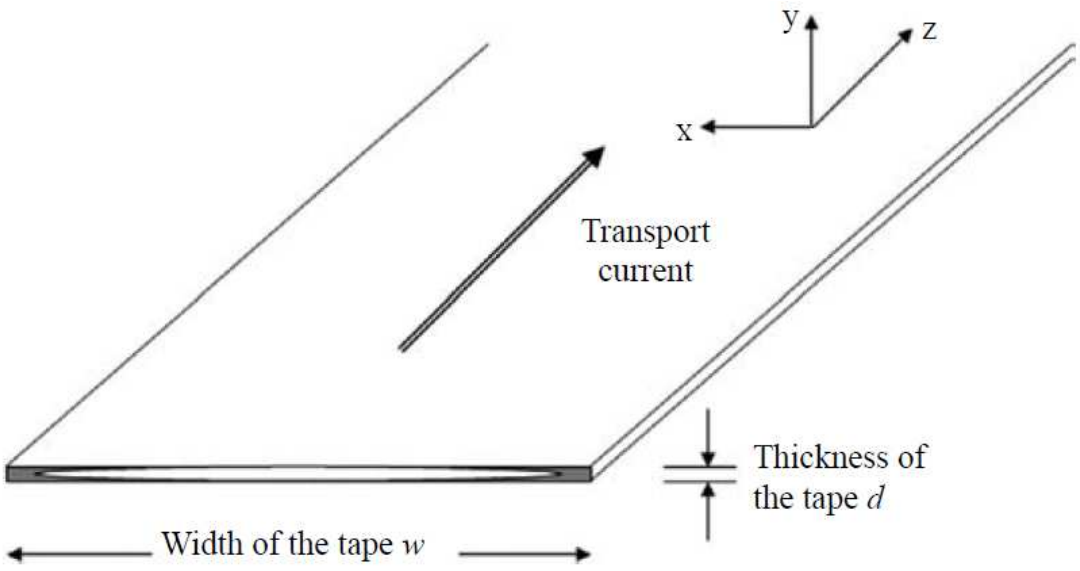

Figure 3.1: FEM model of a high temperature superconductor using the **H** formulation

where $\mathbf{u} = \begin{bmatrix} H_x \\ H_y \end{bmatrix}$

Since **u** is a vector of dependent variables, e_a is a matrix and is known as the mass coefficient. d_a is the damping coefficient and F is the source term. Γ is known as the flux vector. The flux vector Γ, and e_a, d_a and F, can be functions of the spatial coordinates, the solution **u**, and the space and time derivatives of **u**.

Combining this with the previous analysis of Maxwell's equations, we find the subdomain settings to be used in Comsol:

$$\begin{bmatrix} 0 & 0 \\ 0 & 0 \end{bmatrix} \frac{d^2\mathbf{u}}{dt^2} + \begin{bmatrix} \mu_0 & 0 \\ 0 & \mu_0 \end{bmatrix} \frac{d\mathbf{u}}{dt} + \nabla \cdot \begin{bmatrix} 0 & E_z \\ -E_z & 0 \end{bmatrix} = \begin{bmatrix} 0 \\ 0 \end{bmatrix}$$

A Dirichlet boundary condition is used at infinity, which corresponds to the simplest case where transport current flows and there is no externally applied magnetic field. The continuity equation $\mathbf{n} \times (\mathbf{H_1} - \mathbf{H_2}) = \mathbf{0}$ is used at the boundary between air and the superconductor. This is implemented in Comsol by applying Neumann boundary conditions at the surface of the superconductor.

This implies that the tangential components of the magnetic field intensity are conserved at either side of the material interface. An alternative way of expressing this is

$$\frac{dH_{t1}}{dn} = 0, \ \frac{dH_{t2}}{dn} = 0 \tag{3.7}$$

where H_{t1} and H_{t2} are the tangential components of the magnetic field at the surface of materials 1 and 2, respectively.

The PDEs are solved using Comsol, subject to these boundary conditions.

In order to set up these equations in Comsol, scalar expressions must be defined. Firstly, J_z is defined by the expression "d(H_y,x) - d(H_x,y)". ρ_{sc} is defined as "$\rho_{sc} = \frac{E_0}{J_c}(\frac{|\mathbf{J}|}{J_c})^{n-1}$". The electric field E_z is defined for the superconductor subdomain by the (subdomain) expression $\rho_{sc} \cdot J_z$. Similarly, E_z is defined for the air subdomain by the (subdomain) expression $\rho_{air} \cdot J_z$ where ρ_{air} is defined as a constant (e.g. 2×10^{14} Ωm).

A constraint must be placed on the current flowing in the superconductor and this is done by defining a Subdomain Integration Variable I_{int} to ensure the current flow is restricted to the superconductor subdomain. The current applied can be either DC or AC and can be modified as described above for an applied magnetic field. Thus, $I_{int} = \int\int J_z \, dxdy = \int_s J_z \, ds$ where s is the cross-section of the superconductor. This is then used as either a boundary or point setting to constrain current flow to the superconductor; for example, $I_{int,subdomain} = I_{app}$. The current can be defined as a scalar expression as above (e.g. $I_0 \sin(2\pi ft)$ or $I_0(1 - e^{(-\frac{t}{\tau})})$) or defined explicitly in the boundary/point setting.

An external magnetic field can be applied to the tape by modification of the Dirichlet boundary condition described in the previous section. For a transverse applied magnetic field of constant magnitude, i.e. a DC field, the Dirichlet boundary condition is modified such that $H_x = H_{ext}(1 - e^{(-t/\tau)})$ where H_{ext} is the magnitude of the field and the time constant τ is, for example, 0.02 s. Although this function is clearly time-dependent, a step function may not be applied because of the boundary condition due to the initial conditions of the model ($H_x = H_y = 0$) and that to apply a DC field instantaneously is non-physical. A ramp function is also appropriate. For a parallel applied magnetic field of con-

stant magnitude, the Dirichlet boundary condition is modified for the y axis, i.e. $H_y = H_{ext}(1 - e^{(-t/\tau)})$. An alternating magnetic field can be applied by modifying the $(1 - e^{(-t/\tau)})$ term to $\sin(2\pi ft)$ where f is the frequency in Hertz.

Using the model described, the electromagnetic characteristics of a single superconducting tape with an applied transport current and/or applied magnetic field can be analysed for both constant and time-varying conditions.

3.2 Existing coil models

The cross-section of superconducting cables and coils is often modelled as a two-dimensional stack of coated conductors, and these stacks can be used to estimate the AC loss of a practical device. There are a number of examples in the literature that, based on different assumptions and techniques, investigate different aspects of stack problems, such as magnetisation and transport AC loss. A number of techniques are based on the critical state model: [64, 65] use an analytical technique using the infinite[1] stack approximation, [66–69] use a numerical technique for an arbitrary stack, and [42, 70, 71] are based on variational formulations[1].

To model such a stack in this research, the FEM model based on the **H** formulation introduced previously is extended to allow for a multiple number of tapes interacting together. Comparisons with experimental measurements of AC loss in single and small numbers of tapes have shown the **H** formulation to be accurate in predicting losses for simple geometries [62, 72, 73].

In the following sections of this chapter, different aspects of the coil model are investigated, in order to produce an optimised model in terms of accuracy of solution and computational speed. Firstly, the coil under examination for the majority of this dissertation is introduced, then an investigation is carried out on the artificial expansion of the thickness of the YBCO layer and selecting an appropriate mesh type and number of elements. This is done using a single tape, as the preliminary groundwork for optimising more complex geometries. Next, the artificial expansion technique is applied to a coil geometry to model the individual turns of the coil, and the result is compared with a model using a bulk

[1]The term 'infinite' here refers to the height of the stack, i.e. the number of coated conductors in the stack.

approximation. A technique is then applied that allows the actual superconducting layer thickness to be modelled without the associated problem of increased computation time due to a large number of mesh elements, and the model is modified to allow the inclusion of a magnetic substrate. This analysis raises a number of interesting points regarding the use of superconductors with magnetic substrates, and a comprehensive analysis of stacks of tapes with weak and strong magnetic substrates is provided at the end of this chapter, using a symmetric model that requires only one quarter of the cross-section to be modelled.

3.3 Test superconducting coil for modelling

The superconducting coil under examination for the majority of this dissertation is found on the stator of the all-superconducting HTS permanent magnet synchronous motor (PMSM) designed by the EPEC Superconductivity Group at Cambridge [41, 74–81].

The design of the motor is detailed in [76] and [77], and a photograph of the completed test rig is shown in Figure 3.2. The rotor is made of 75 superconducting pucks, arranged in 15 columns of 5 pucks, which can be magnetised to the equivalent of a four-pole permanent magnet. The stator consists of six HTS armature windings, which are installed in slots made of a non-magnetic insulating material. The entire HTS motor is to be cooled by liquid nitrogen to 77 K.

The armature winding in the HTS motor is made of six single flat-loop coils, which are wound as flat racetrack pancake coils with a bend radius of several centimeters. Double layers of HTS windings are stacked together to make one racetrack winding. This maximizes the inductance of the winding within the limited geometry [75]. The total number of turns per phase for the stator windings is 200 turns (with 50 turns for each layer, 100 turns per coil, and two coils per phase). Approximately 60 m of American Superconductor [26] type 344 2G coated conductor was used to wind each coil. The properties of the AMSC YBCO 344 tape used in the stator coils are listed in Table 3.1. A photograph of a manufactured coil is shown in Figure 3.3 and the dimensions are shown in Figure 3.4.

The critical current of a YBCO tape sample and the whole coil were measured

by the DC pulse current measurement technique [76], and the results for the sample and coil are shown in Figure 3.5. The critical current criteria used is based on an electric field $E_0 = 1\ \mu V/cm$. For the YBCO tape sample, the length between the voltage taps is 2 cm, so the measured critical current is 106 A. On the other hand, the total length of the HTS coil is 60 m, so the measured critical current of the coil is 51 A.

The decrease of the critical current is due to several factors. The first is the self magnetic field generated by the HTS coil. Additionally, bending the tape to construct the coil can degrade the tape's performance. The dependence of the critical current on the presence of a magnetic field will be discussed in detail in the following chapter. Furthermore, the HTS tape used to wind the coil was provided in 20 m lengths, while the whole length of the coil is 60 m. This leads to at least two wire joints within the coil, which reduces its critical current due to the finite resistance of these connections. When the critical current of the coil was measured, there was no external magnetic field applied, so only the self-field was present. There will also be a reduction in critical current due to the magnetic field from the pucks on the rotor when the motor itself is run.

Table 3.1: AMSC YBCO 344 tape properties [76]

Average thickness	0.20 mm ± 0.02 mm
Width	4.35 mm ± 0.05 mm
Maximum width (bare)	4.4 mm
Minimum double bend diameter (RT)	30 mm*
Maximum rated tensile stress (RT)	150 MPa*
Maximum rated tensile strain (77 K)	0.3 %*
Maximum rated compressive strain (77 K)	0.3 %*
Length of single tape	20 m
Critical current at 77 K, self-field	> 60 A

*95% I_c retention

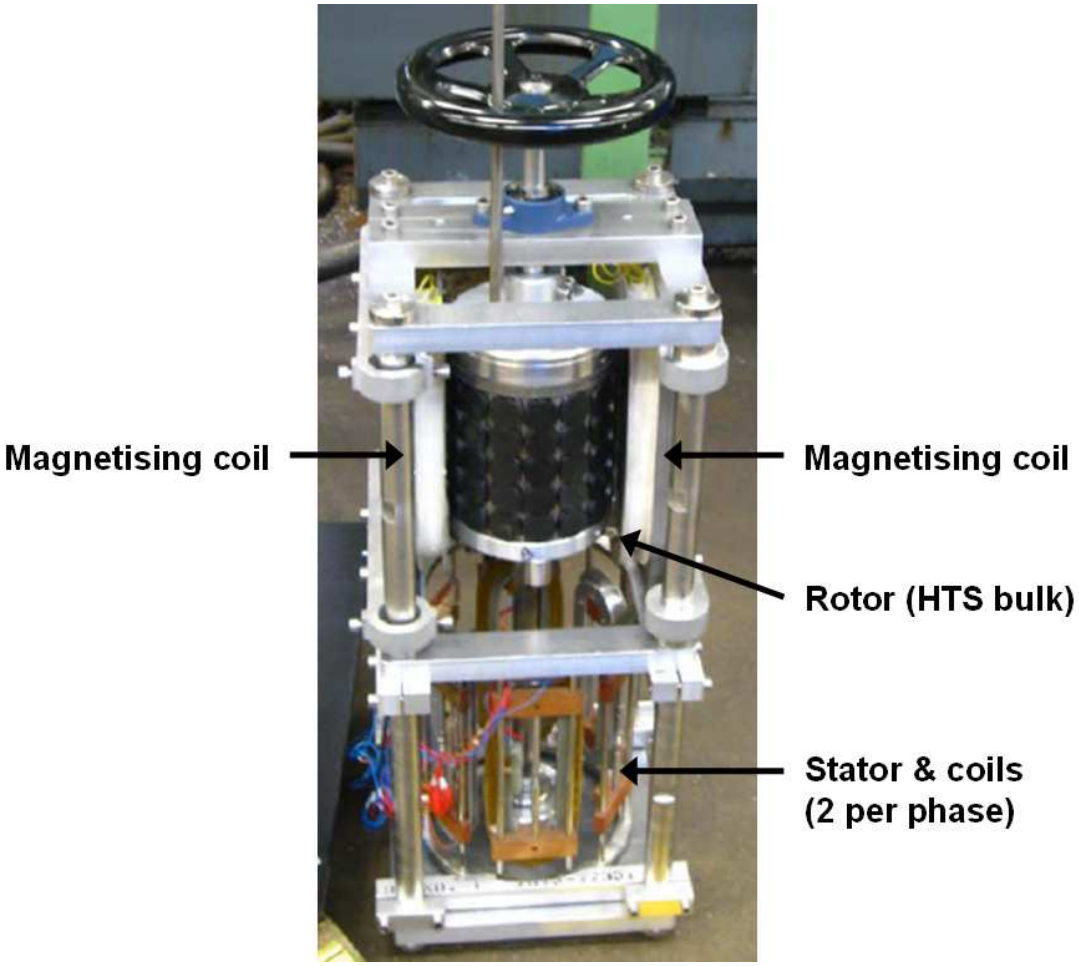

Figure 3.2: Photo of the HTS PM synchronous motor rotor test rig [82]

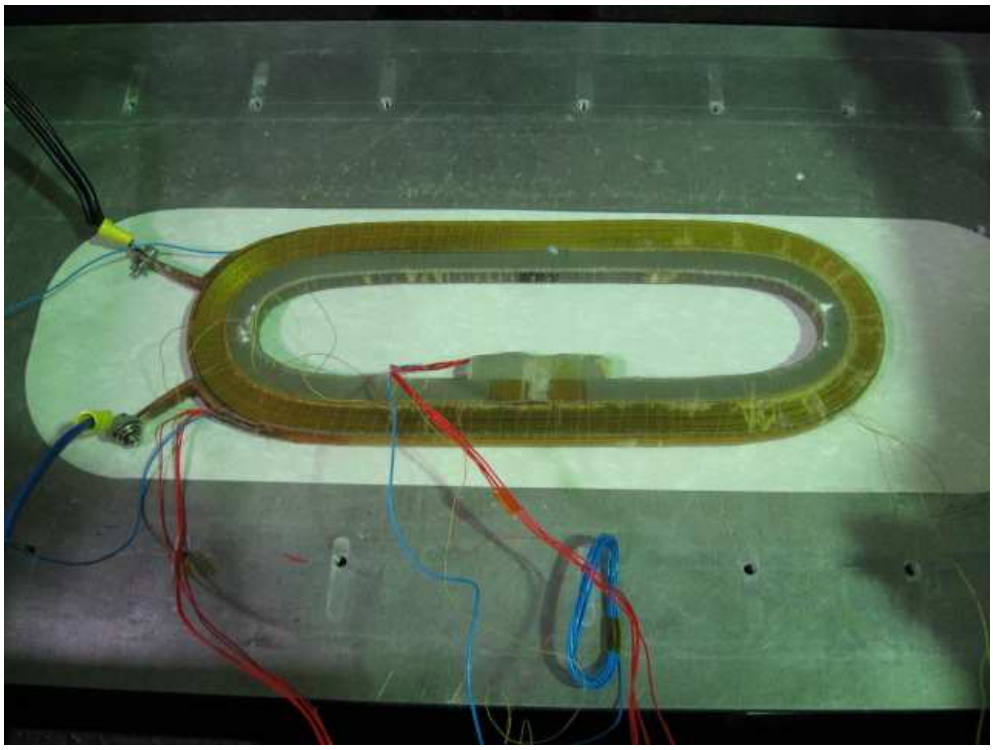

Figure 3.3: Photograph of an HTS PM synchronous motor stator coils

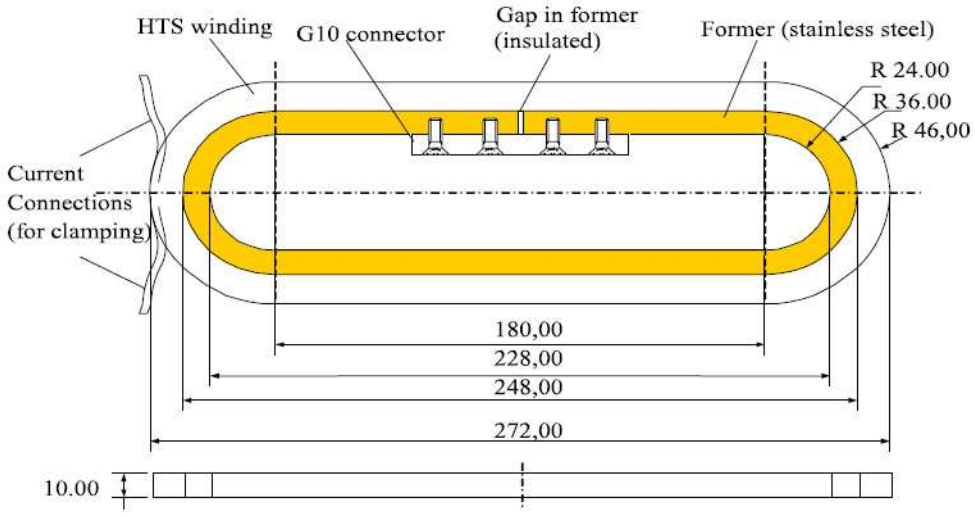

Figure 3.4: Dimensions of an HTS PM synchronous motor stator coil

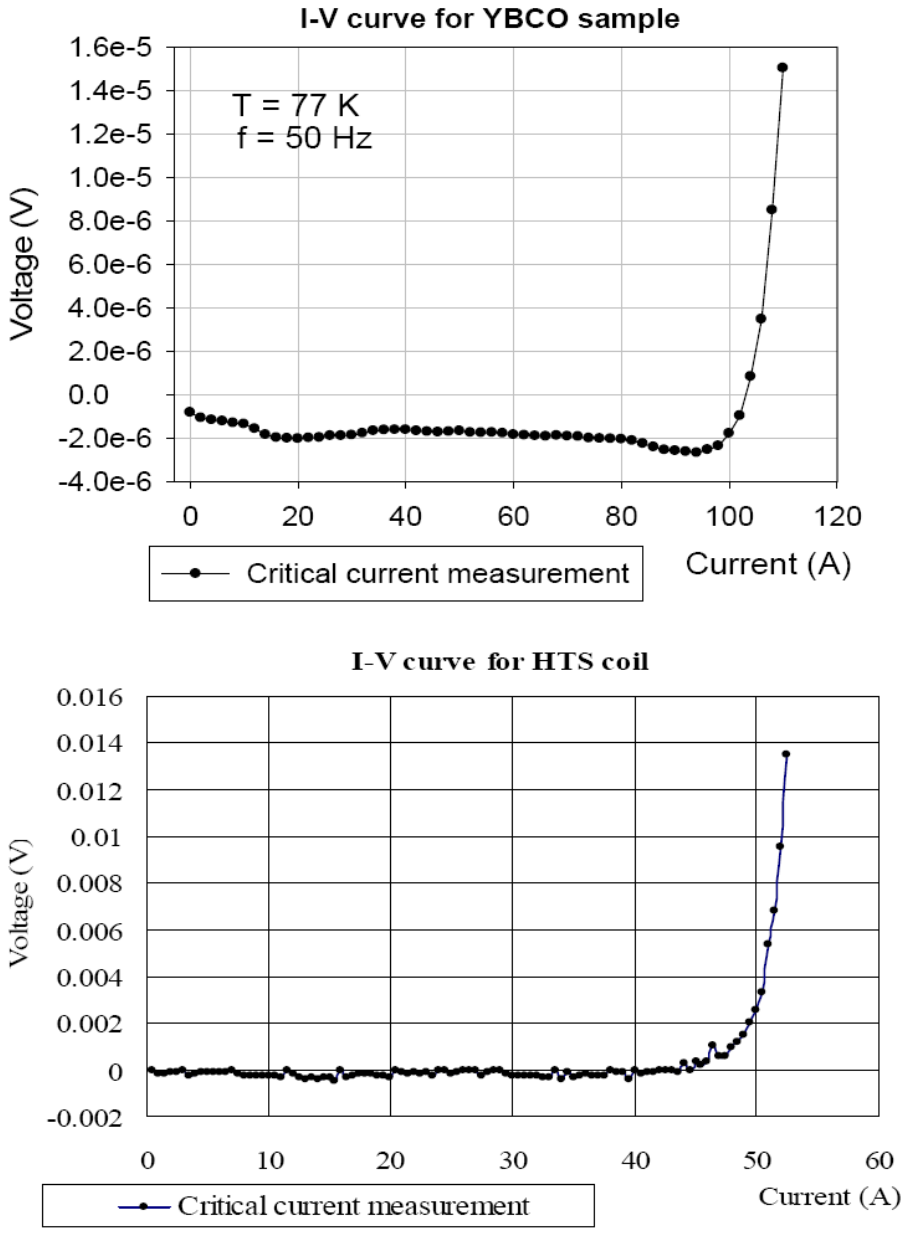

Figure 3.5: Critical current of the YBCO sample tape and coil [76]

3.4 Artificial expansion technique for individual tapes

The geometry of the model is shown previously in Figure 3.1 and the specification of the superconductor under analysis is listed in Table 3.1. The specification is based on the material used in the superconducting racetrack coil shown in Figure 3.3. The critical current density J_c is given by

$$J_c = \frac{I_c}{w \cdot d_{sc}} \tag{3.8}$$

where I_c is the critical current of the tape measured experimentally, and w and d_{sc} are the width and thickness of the superconducting layer, respectively.

One simple way to model a coated conductor for a stack of tapes or coil geometry is to approximate the geometry of the superconducting layer as the whole tape thickness, i.e. 200 μm [66, 67]. Artificially increasing the superconducting layer can improve computational speed by reducing the number of mesh elements required, making it easier to model more complex 2D geometries, but the accuracy of results must not be compromised. The artificial expansion technique works because the dynamics of the flux penetration for this geometry is essentially along only one axis. For a thin strip, which describes the layer of superconducting material in a coated conductor, the flux front moves along the x-axis in this geometry (see Figure 3.1), from the edge of the tape towards the centre, for increasing values of current [38]. As long as a significantly large aspect ratio is maintained, the coated conductor will still behave like an infinitely thin strip, with the current distribution front moving along the x-axis. It will become apparent where the model's behaviour begins to deviate significantly from that of an infinitely thin strip.

200 μm is assumed as the maximum thickness here, which is equal to the whole conductor thickness, and the thickness is varied from this to 2 μm, where 1-2 μm is the approximate real thickness of the YBCO layer. Keeping the width of the tape constant (4.35mm) and the critical current I_c as 100 A, the critical current density must be modified according to the thickness used. For a thickness of 200 μm, the critical current density J_c is 1.15×10^8 A/m^2, which is known as the engineering

critical current density J_e. For a thickness of 2 μm, J_c is 1.15×10^{10} A/m^2.

In order to simplify the analysis and allow comparison with Norris's analytical equation introduced in the previous chapter, the critical current density is assumed to be independent of applied magnetic field, i.e. J_c is constant. In reality, the critical current depends not only on the magnitude, but also the direction of the field, which includes the superconductor's self field. Field dependence of the critical current will be investigated later in this chapter. Furthermore, in this analysis, only the superconductor layer is modelled and the presence of a substrate (and its associated loss) is ignored. This, too, will be investigated later in this chapter. Here we are concerned only with the hysteretic superconductor loss, and the material surrounding the superconducting layer is represented by air, i.e. a relative permeability of 1 and very low electrical conductivity. This investigation is based on an analysis of transport AC loss only and this requires appropriate settings for the boundary conditions. Since no externally applied magnetic field exists, the boundary settings are $H_x = H_y = 0$ for a sufficiently large surrounding air subdomain.

The computational effort required by the solver and the accuracy of the solution is highly dependent on the selection of the mesh and its elements. The first model (model A) in this section uses a triangular mesh, and the number of the elements in the mesh is the smallest number possible, maintaining the same aspect ratio for the elements and such that the mesh remains symmetric. The motivation for using a small number of mesh elements is that complex geometries will be easier to model, as modelling multiple turns in a superconducting coil will require hundreds of thousands of mesh elements. This is done in Comsol by setting the maximum element size of the mesh elements to be the same size as the thickness of the superconducting layer to be meshed via the subdomain free mesh parameters, i.e. for a superconducting layer thickness of 50 μm, the maximum element size is 50 μm. The second model (model B) uses a single layer, square mesh, which is achieved using the same setting. The meshes for the two models are shown in Figure 3.6.

It should be noted that the number of mesh elements within the superconductor is inversely proportional to the thickness of the tape in order to maintain the same aspect ratio for elements within the mesh. The number of mesh elements

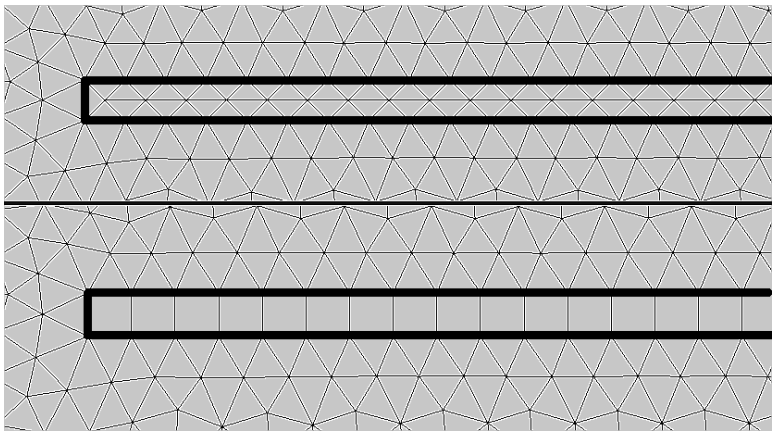

Figure 3.6: Mesh element for models A (triangular) and B (square)

within the superconductor subdomain for different thicknesses for the two models is shown in Figure 3.7, where model A is represented by triangles and model B is represented by squares. Furthermore, the number of mesh elements in the air subdomain for each model is identical for a particular thickness.

In order to make a comparison between the two different meshes and different element types, the following terminology is used hereafter when describing the different models:

- **A1** = Triangular minimum symmetric, first-order Lagrange elements
- **A2** = Triangular minimum symmetric, second-order Lagrange elements
- **AE** = Triangular minimum symmetric, edge elements
- **B1** = Square single layer, first-order Lagrange elements
- **B2** = Square single layer, second-order Lagrange elements

To implement edge elements, Comsol's "shvec" type was used. Comsol implements two formulations for vector, or edge elements, known as "shvec" and "shcurl." "shvec" elements are only implemented for first-order triangular elements, whereas "shcurl" elements are implemented for all element types within Comsol. When this analysis was carried out using the same model settings as

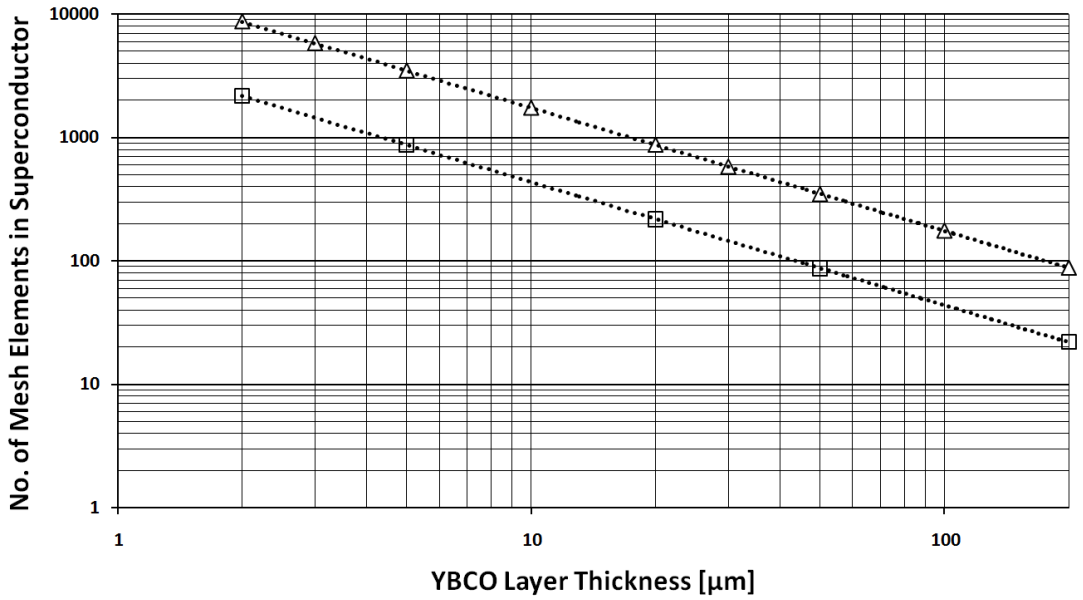

Figure 3.7: Number of mesh elements for different YBCO layer thicknesses for models A (represented by triangles) and B (represented by squares)

the other models, the "shcurl" element either failed to converge to a solution, or if it did, the convergence time was unacceptably long and resulted in non-physical, spurious solutions. On the other hand, for first-order triangular "shvec" elements, the results were in good agreement with theory and also with the models where Lagrange elements were used. Hence, a mesh comprising square single layer, edge elements has been omitted from the analysis. How to overcome this problem is discussed in a following section on modelling the real thickness of the superconducting layer.

3.4.1 Solver time and convergence comparison

One of the critical parameters for modelling coated conductors with high aspect ratios is the computation time required to solve them. Figure 3.8 shows a comparison of the computation time for models A1, A2 and AE for different I_0/I_c ratios (0.25, 0.5, 0.75 and 0.9) as the thickness of the tape is varied between 2 and 200 μm, where I_0 is the amplitude of the input current. Figure 3.9 shows a com-

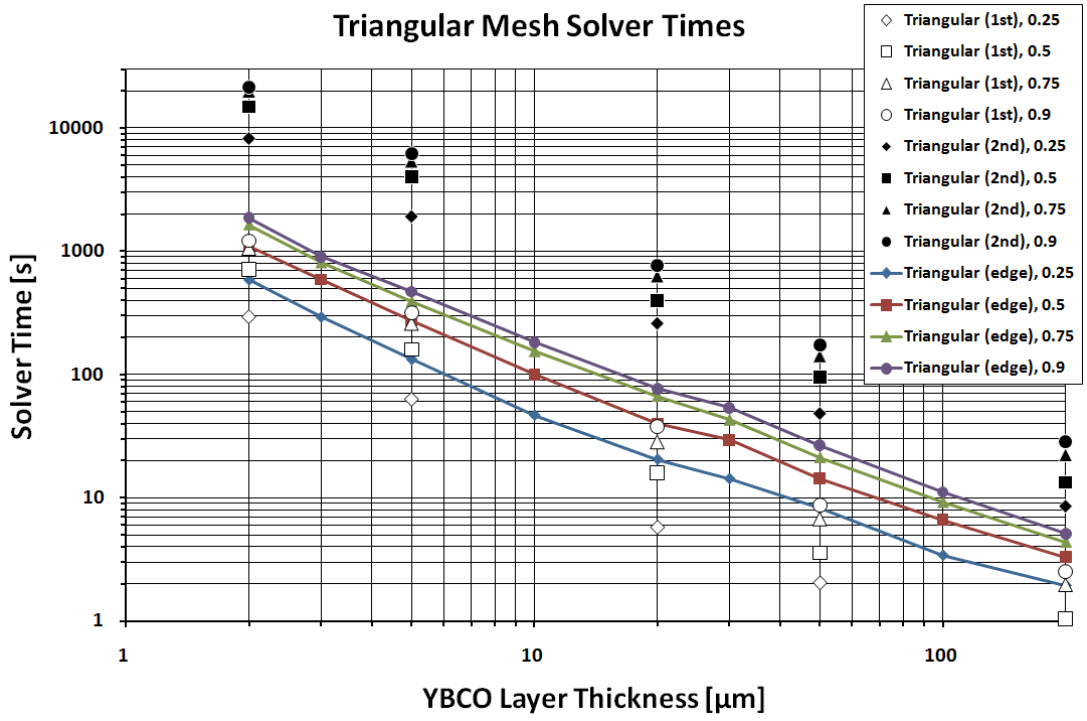

Figure 3.8: Triangular mesh solver times

parison of the computation time for models B1 and B2 for the same conditions. Figures 3.8 and 3.9 show that the computation time increases as the thickness of the superconductor decreases. The time to solve is an order of magnitude higher when second-order elements are used instead of first-order elements for models A and B, and the solver time for triangular edge elements is slightly longer than for first-order elements.

When comparing the triangular mesh with the square mesh for the same order of elements, the triangular mesh takes a few (approximately two to three) times longer to solve. As shown previously in Figure 3.7, the number of mesh elements in model B is four times less than model A. The computation time cannot be estimated by the number of elements in the mesh alone, which in this case would give the expectation that the square mesh (with less mesh elements) would produce a faster solution.

A better measure of computation time is the number of degrees of freedom

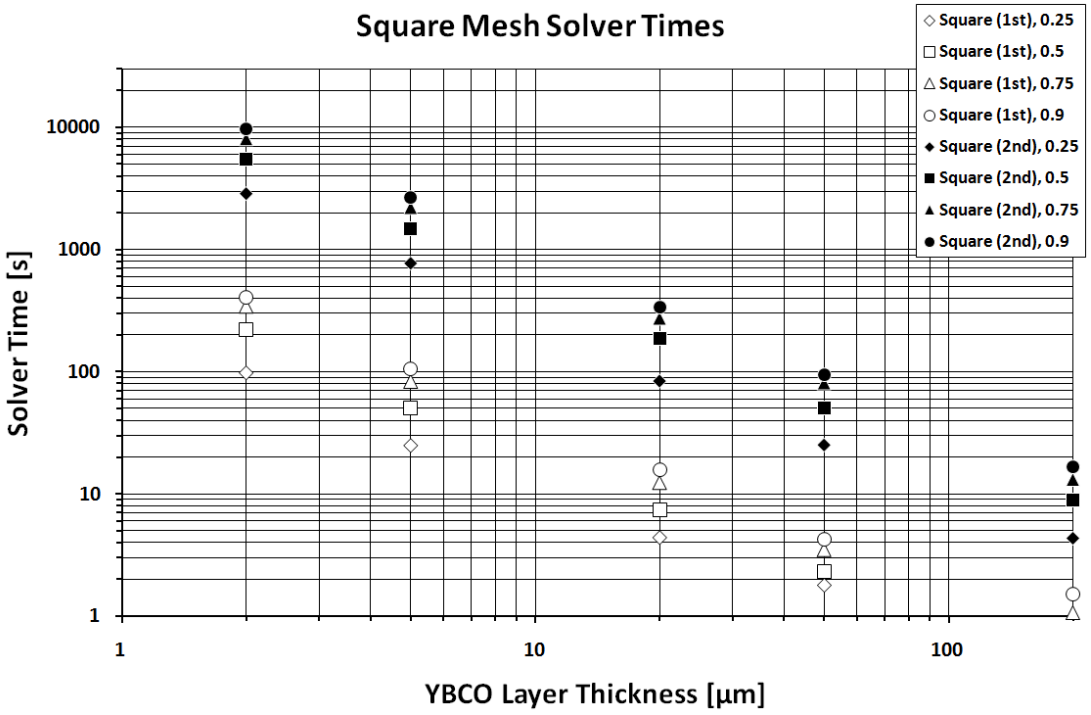

Figure 3.9: Square mesh solver times

the model has [62], which is shown in Figure 3.10 - triangles represent Lagrange elements in model A and squares represent model B. Edge elements (model AE) are represented by diamonds. The double solid line represents second-order Lagrange elements and the double dashed line represents first-order Lagrange elements. The number of degrees of freedom is related to both the number and type of mesh elements used (first-order, second-order, and so on). The degrees of freedom are comparable when using the same order of Lagrange elements, and there are about four times as many degrees of freedom for second-order elements as first-order. The number of degrees of freedom for edge elements is in between the two. The solver times in Figures 3.8 and 3.9 correlate well with the degrees of freedom in Figure 3.10.

A time-dependent solver is used to solve each model using Comsol's default linear system solver (UMFPACK). The default time-stepping method uses variable-order, variable-step-size backward differentiation formulae, and the time steps are automatically selected by the solver. To give a quantitative analysis of the con-

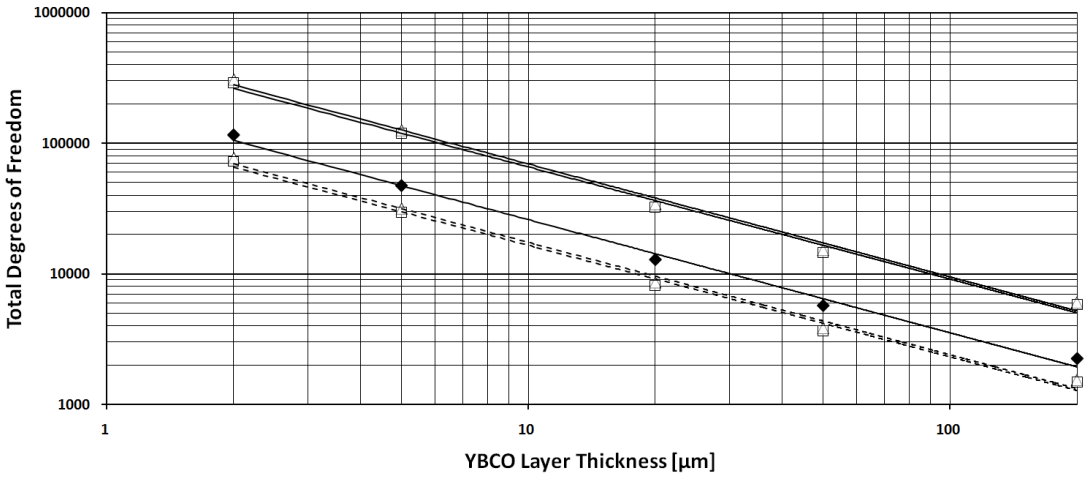

Figure 3.10: Total number of degrees of freedom for different YBCO layer thicknesses for all models. Triangles represent triangular meshes (model A), squares represent square meshes (model B), and diamonds represent edge elements (model AE). The double solid line represents second-order Lagrange elements and the double dashed line represents first-order Lagrange elements.

vergence of each model, Figure 3.11 shows the solver time divided by the degrees of freedom. The second-order models require longer time steps than first-order, meaning second-order models have worse convergence behaviour. The convergence for the edge element model lies in between these two. When less current is applied to the superconductor (e.g. 0.5 I_c instead of 0.9 I_c), the convergence behaviour improves as the current front does not penetrate as far into the superconductor.

Here we have examined the model properties to optimise the computational speed and convergence based on the type of elements and level of discretisation. In the following section, the real quantity of interest, i.e. the AC loss, is calculated, and the accuracy is compared for the different models.

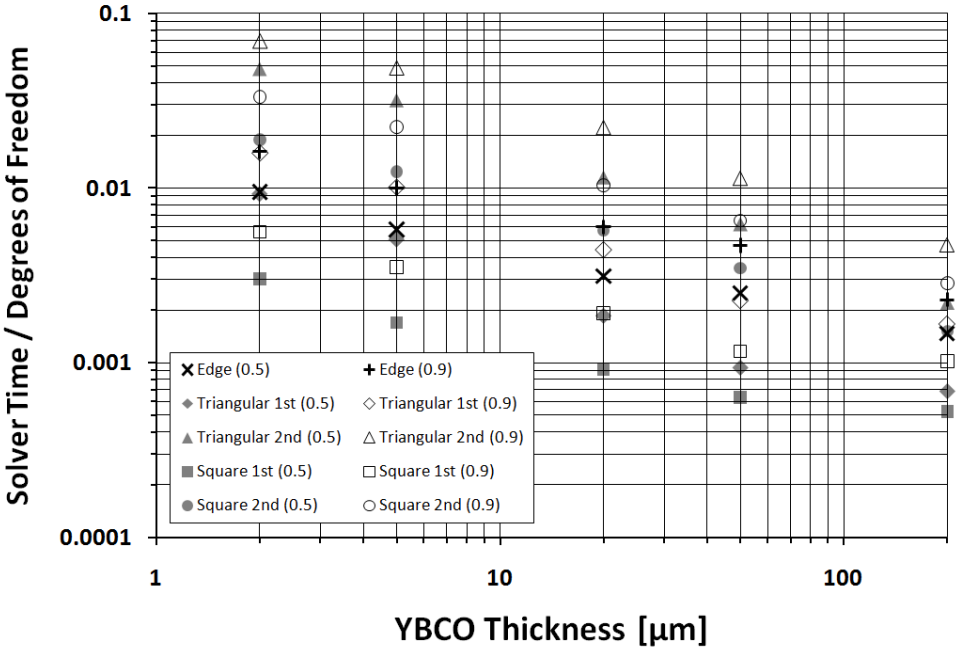

Figure 3.11: Convergence behaviour for all models using solver time per degree of freedom

3.4.2 AC loss comparison

The AC loss per unit length per cycle is calculated using the following equation

$$Q = \int_0^{1/f} \int_S \mathbf{E} \cdot \mathbf{J} \, dS \, dt \tag{3.9}$$

where 1/f is the period of the AC current of frequency f, S is the superconductor cross-section, and $\mathbf{J}$ and $\mathbf{E}$ are the critical current density and electric field at each mesh node, respectively. This gives a loss with units of J/cycle/m.

Figure 3.12 shows the values calculated for the AC loss for all models for YBCO layer thicknesses between 2 and 200 μm. The calculated AC loss in each of the models is compared with the analytical model proposed by Norris, which was introduced in the previous chapter. The analytical equation used for the comparison is Equation 2.26 divided by the frequency f to give units of J/cycle/m.

For I_0/I_c values between approximately 0.5 and 0.9, the calculated AC loss value is similar to the analytical result for models A2, AE and B2. There is no

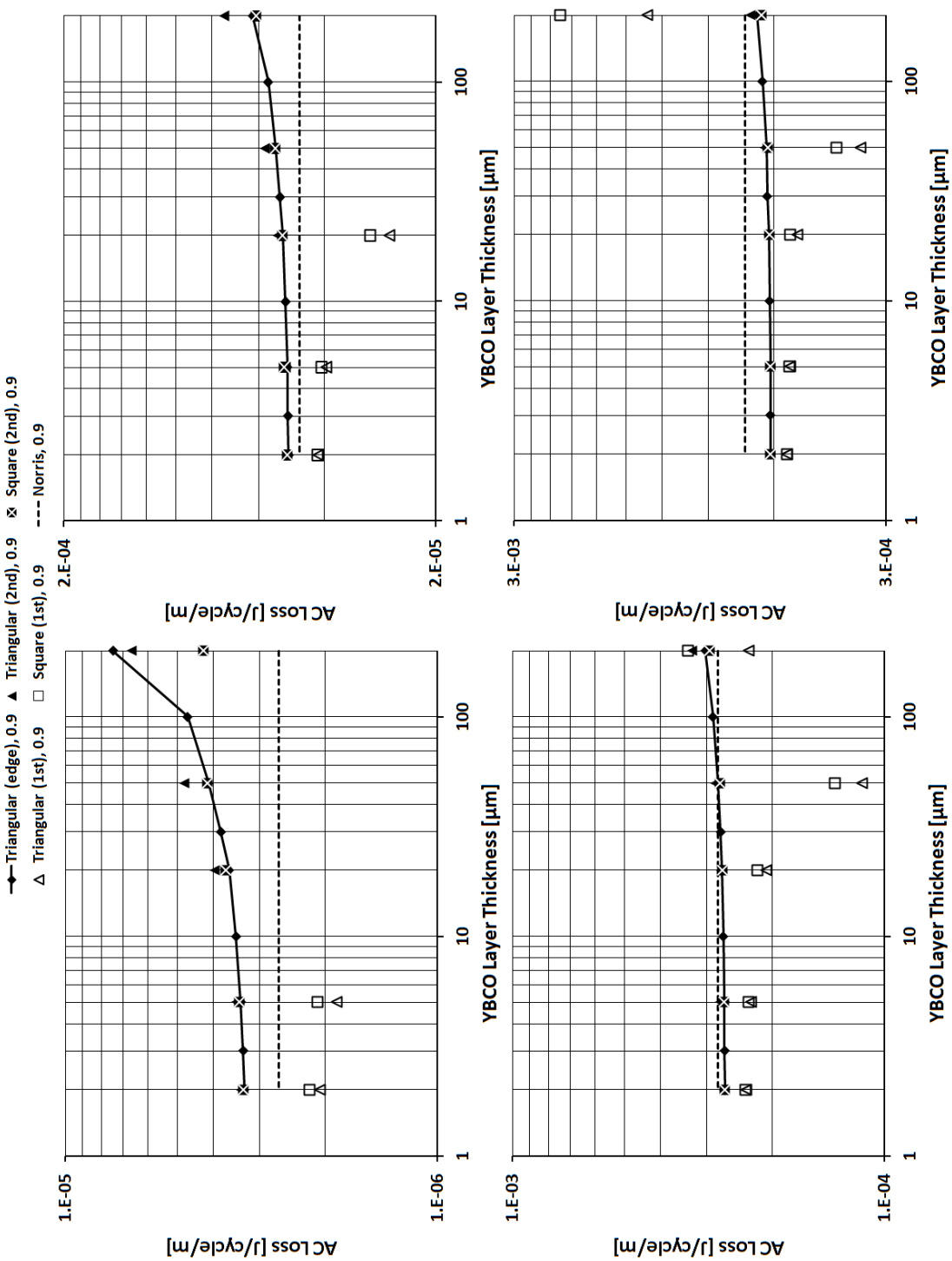

Figure 3.12: AC loss calculation for all models for different YBCO layer thickness compared with Norris's analytical model (clockwise from top left: $I/I_c = 0.25$, $I/I_c = 0.5$, $I/I_c = 0.75$, $I/I_c = 0.9$)

significant variation for these currents over the whole range of thicknesses. For $I_0/I_c = 0.25$, there is a significant variation between the analytical result and the finite element model, particularly when the YBCO layer thickness is large ($\longrightarrow$ 200 μm), where there is also variation between models A2, AE and B2. Similar findings were reported in [83], but should not be a major concern as in practical situations, the ratio I_0/I_c should be maximised, i.e. $\longrightarrow 1$, in order to fully utilise the superconductor's properties, and the region of I_0/I_c between 0.5 and 1 is of primary importance.

For models A1 and B1, the AC loss is significantly lower than the analytical model and deviates significantly as the thickness is increased. Therefore, the first-order models do not produce results which can be relied upon to provide an accurate estimation of AC loss. For these models, the current density profile does not accurately represent the current flow as it should, and as a result, the electric field profile is significantly distorted. For problems involving superconductors, the errors in the current density profile should be minimised as the power-law relationship with electric field creates a much larger error when calculating the electric field and AC loss.

In Figure 3.13, the current density distribution within the superconductor is shown for both models for a transport current $I_0 = 0.5\ I_c$ for YBCO layer thicknesses of 2 and 20 μm. The average values of the current density for different points along the tape width compares well with those calculated by the analytical model, although the current density distribution for triangular second-order elements shows an increase between 2 and 20 μm thicknesses.

In terms of computational speed and accuracy of solution, model AE (edge elements) performs the best of the models. Using first-order elements, whilst faster, does not produce accurate results, and using second-order elements, whilst producing accurate results, takes significantly longer to solve.

In terms of the artificial thickness expansion, the results show that when calculating AC loss, the current density profile should not be significantly modified by the expansion, such that any change in $\mathbf{J}$ affects the AC loss calculation. The electric field is calculated using a power-law relationship, so errors in $\mathbf{J}$ are amplified. For the values of current of interest (I_0/I_c between 0.5 and 1), the thickness may be expanded up to 20-30 μm before the result begins to deviate appreciably.

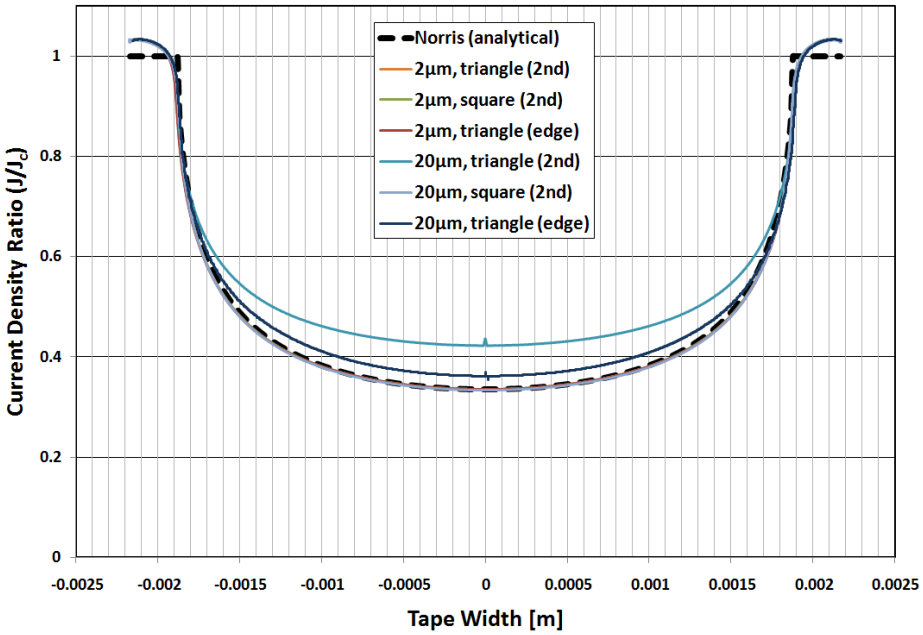

Figure 3.13: Comparison of current density distribution in superconductor with Norris's analytical model for models A2, AE and B2 for $I/I_c = 0.5$ for 2 and 20 μm YBCO layer thicknesses

The ability to artificially expand the YBCO layer thickness will become even more important when modelling complex device geometries, such as wound coils or devices themselves. In the following section, the artificial expansion is applied to a coil geometry to model the individual turns of the coil, and the result is compared with the bulk approximation model.

3.5 Artificial expansion vs. bulk approximation

As described above, one method to improve the speed and convergence of the model is to artificially increase the superconductor layer thickness. In this section we model the cross-section of the racetrack coil using two models: 1) individual turns using the artificial expansion technique, and 2) using a bulk approximation. For the model using individual turns, a thickness of 50 μm is chosen, for which the critical current density is $J_c = 4.6 \times 10^8$ A/m^2. Although an expanded thickness

of 20-30 μm is ideal based on the conclusions from the preceding analysis of a single tape, this would result in a number of mesh elements on the order of 2-300,000, and an even greater number of degrees of freedom, which exceeds the memory capacity of the computer being used. Even the 50 μm model with a minimum symmetric mesh within the superconductor and a free triangular mesh elsewhere results in over 100,000 mesh elements with around 175,000 degrees of freedom.

Each layer is separated by 200 μm to account for the other layers of the superconductor. For each superconducting layer, the minimum possible symmetric mesh is used along with edge elements. For the bulk approximation, the same critical current density is used, but for a geometry of one turn with thickness n times 50 μm, effectively removing the non-superconducting area between the tapes in the individual turns model. Hence, this approximation assumes that the tapes couple electromagnetically such that the multiple tapes behave as a finite superconducting slab carrying n times the current of each individual tape. The geometry and mesh for the individual tapes and bulk models are shown in Figure 3.14 and 3.15, respectively.

For these two models, two critical current densities are compared: the constant J_c value given above, and a B-dependent J_c, which is given by Equation 2.18. Figure 3.16 shows the calculated AC loss for the four different cases: 1) individual turns using a constant J_c, 2) individual turns using the J_c(B) dependence, 3) the bulk approximation using a constant J_c, and 4) the bulk approximation using the J_c(B) dependence.

The J_c(B) dependence increases the calculated AC loss, as the reduced J_c due to the magnetic field results in further penetration into the stack. The calculated AC loss is also increased for the bulk approximation, but for a different reason: the bulk approximation assumes that the individual turns are perfectly electromagnetically coupled, but in reality the coupling between the turns is not so simple. Thus, the bulk approximation will tend to overestimate the calculated loss. The individual turns model is more accurate, as long as the expanded thickness remains within the limit specified earlier. The accuracy gained in comparison with a bulk approximation model is better than any time lost through a small increase in computation time.

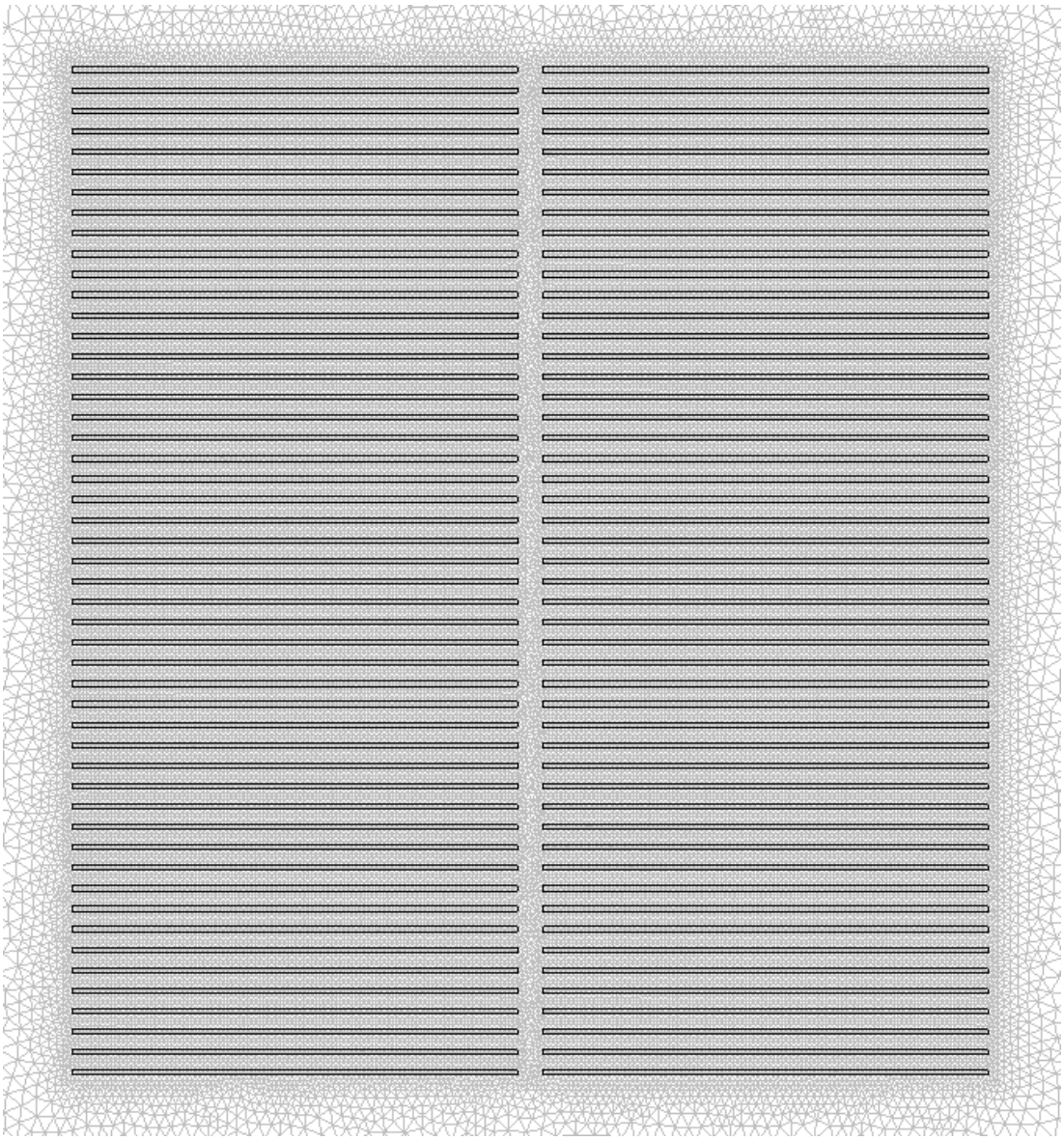

Figure 3.14: Geometry and mesh for model of individual turns using artificial expansion technique

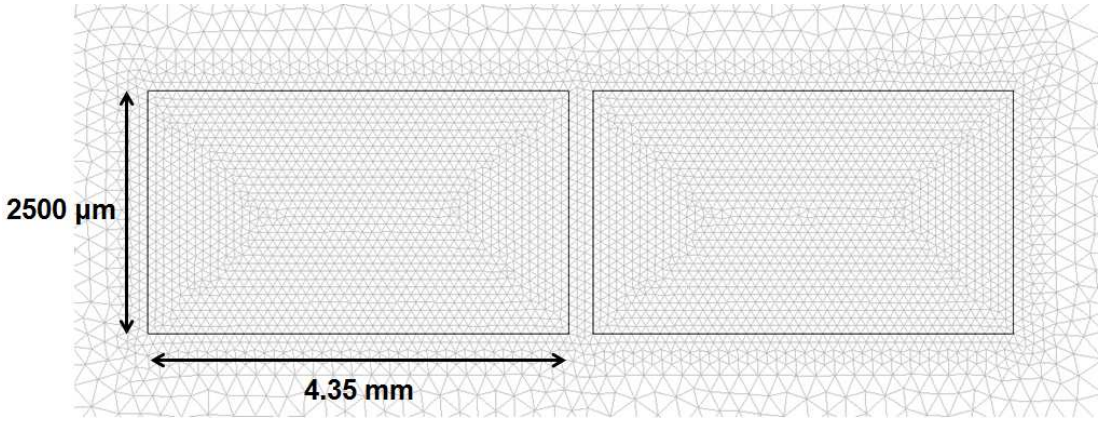

Figure 3.15: Geometry and mesh for model using bulk approximation

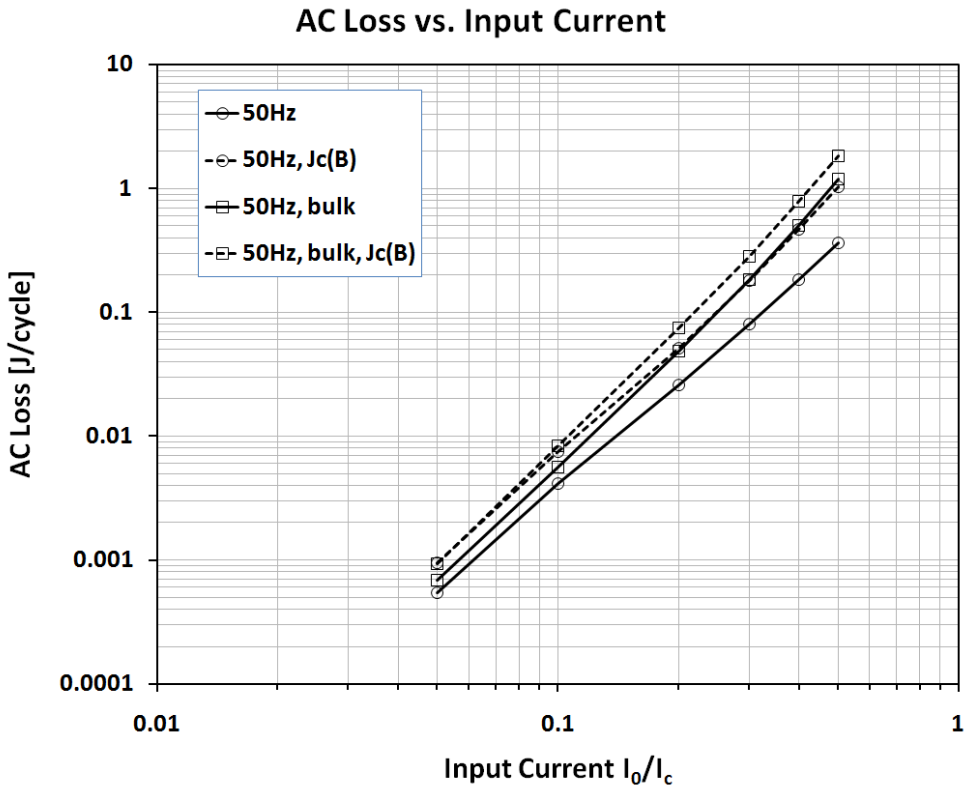

Figure 3.16: AC loss calculation for individual turns and bulk approximation for constant J_c and $J_c(B)$ dependence

3.6 Real thickness

It has been shown that the artificial expansion technique is a valid method to improve the speed and convergence of the superconductor model. The number of mesh elements can be reduced without significant loss of accuracy, provided that the thickness of the superconducting layer is not artificially increased past a certain limit (20-30 μm). However, a significant improvement was made in [84, 85] by using large aspect ratio mapped meshes, hence reducing the number of mesh elements in and between the coated conductors. A sparser mesh is used between the superconducting layers, where it is not as critical to have a fine mesh. Applying the findings of [84, 85], an overall reduction of about two orders of magnitude in the number of elements can be achieved for the coil model in comparison with the previous simulations, which used free meshes. When a free mesh is created in Comsol, the number of mesh elements is determined from the shape of the geometry and various mesh parameters, such as maximum element size, element growth rate, mesh curvature factor, and so on. There are also a number of predefined mesh sizes, ranging from extremely fine to extremely coarse.

Accordingly, by using a mapped mesh, the actual thickness of the YBCO layer can be modelled without a significant increase in computational time, also allowing other layers of the coated conductor, such as the stabiliser layer and substrate, to be implemented using accurate geometrical dimensions. In this section, this technique is applied to model the coil geometry and the exact number of elements required in the superconducting layer is investigated to strike a balance between accuracy and computational speed. The magnetic substrate present in the superconducting coil under investigation is added to the model, which requires modification of the PDEs defined previously, which are only valid when the relative permeability of the materials involved is $\mu_{\mathrm{r}} = 1$.

3.6.1 Optimal number of mesh elements

Previously it was mentioned that when using edge elements (Nedelec elements implemented using the "shcurl" element in Comsol) with square or rectangular mesh elements, the model either failed to converge to a solution, or if it did, the

convergence time was unacceptably long and resulted in non-physical, spurious solutions. To overcome this problem, which was due to the tolerance settings of the solver, the relative and absolute tolerance settings of the solver are set to lower values of 1e-5 and 1e-7, respectively. Previously, these settings were 0 and 1, which was appropriate in producing a fast and accurate solution for those particular mesh/element types.

The relative tolerance specifies the largest acceptable solver error, relative to the size of each state during each time step. If the relative error exceeds this tolerance, the solver reduces the time step size. The acceptable error at each time step is a function of both the relative and absolute tolerances. During each time step, the solver computes the state values at the end of the step and also determines the local error, which is the estimated error of these state values. If the error is greater than the acceptable error for any state, the solver reduces the step size and tries again.

The absolute tolerance specifies the largest acceptable solver error, as the value of the measured state approaches zero. If the absolute error exceeds this tolerance, the solver reduces the time step size. If the absolute tolerance is too low, the solver might take too many steps around near-zero state values, and therefore slow the simulation. If the simulation results do not seem accurate, and the model has states whose values approach zero, the absolute tolerance may be too large. Reducing the absolute tolerance forces the simulation to take more steps around near-zero state values.

By lowering the relative and absolute tolerances as described above, the simulation performs much better, and fortunately this does not hinder the convergence. Thus, square or rectangular edge elements can be utilised and the problems described earlier can be avoided.

Figures 3.17 to 3.21 show a comparison of the AC loss calculation for a single tape with mapped square/rectangular edge elements for I = 0.1, 0.3, 0.5, 0.7 and 0.9 I_c. The number of x and y elements correspond to the number of mapped elements along the x and y axes, respectively. As the base case for the comparison, a very fine mesh of 2000 elements along the x-axis and 20 elements along the y-axis is used, which takes a significantly long time to solve, but produces the most accurate result. It can be seen that a mesh with as little as 100 elements along

the x-axis and a few elements along the y-axis can produce an accurate result, except for small magnitudes of current, which is similar to the previous finding with the artificial expansion technique. This is due to the nature of the flux penetration for small currents/fields where the top/bottom losses are not dominated by the edge losses, i.e. the perpendicular component of the field. Based on these results, a mesh consisting of 100 elements along the x-axis and 4 elements along the y-axis will be used in the superconducting layer for the coil model that follows. However, for small currents, say 0.3 I_c and lower, the number of mesh elements should be increased, in particular the number of elements along the y-axis.

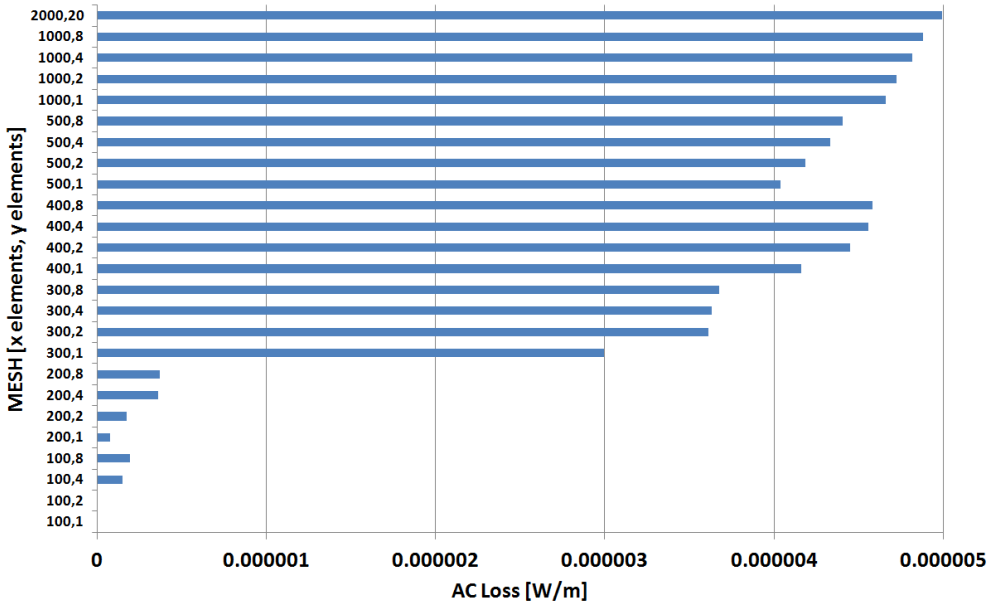

Figure 3.17: Comparison of AC loss calculation for single tape with mapped square/rectangular edge elements, I = 0.1 I_c

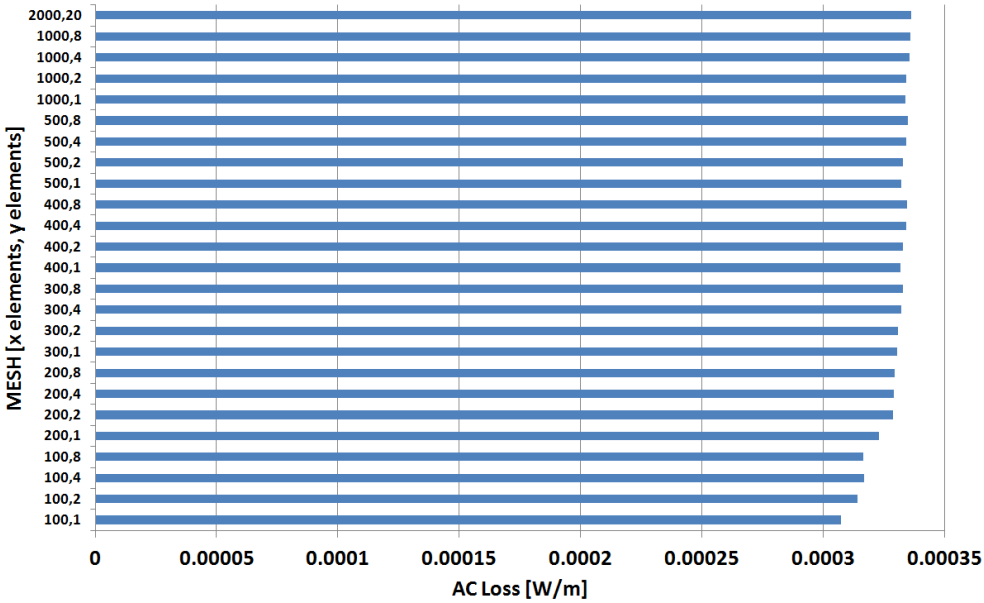

Figure 3.18: Comparison of AC loss calculation for single tape with mapped square/rectangular edge elements, I = 0.3 I_c

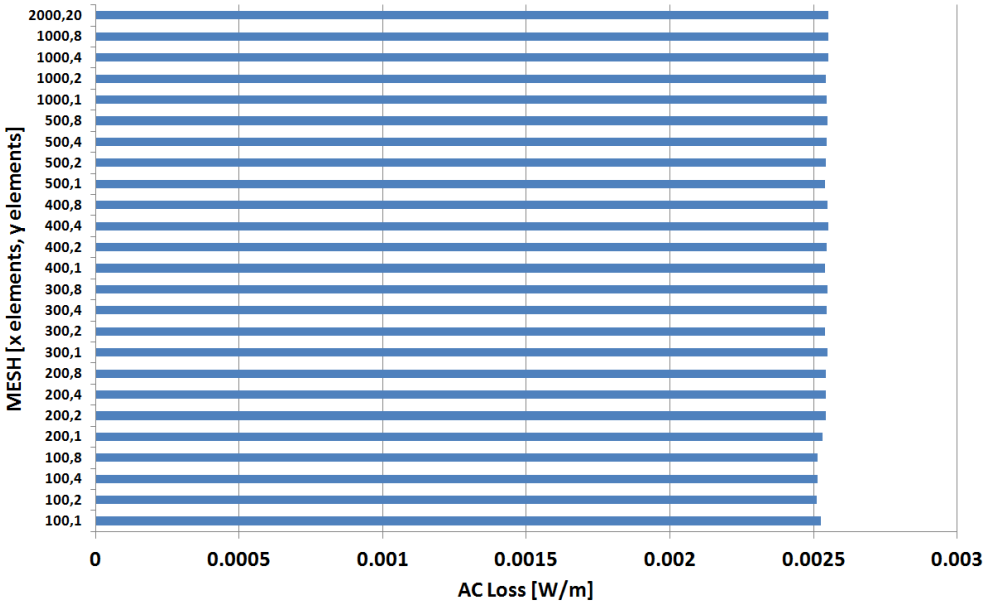

Figure 3.19: Comparison of AC loss calculation for single tape with mapped square/rectangular edge elements, I = 0.5 I_c

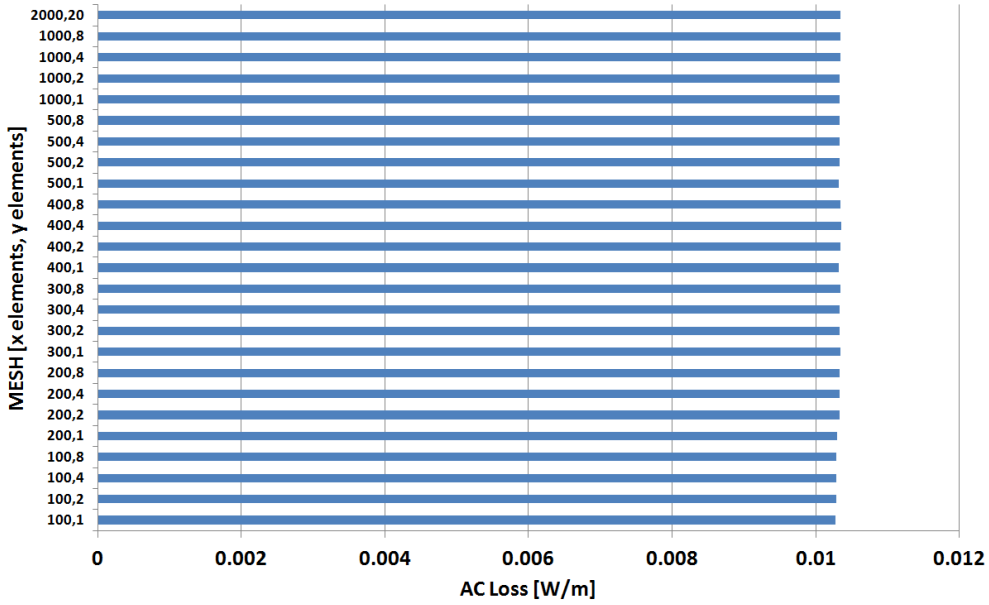

Figure 3.20: Comparison of AC loss calculation for single tape with mapped square/rectangular edge elements, I = 0.7 I_c

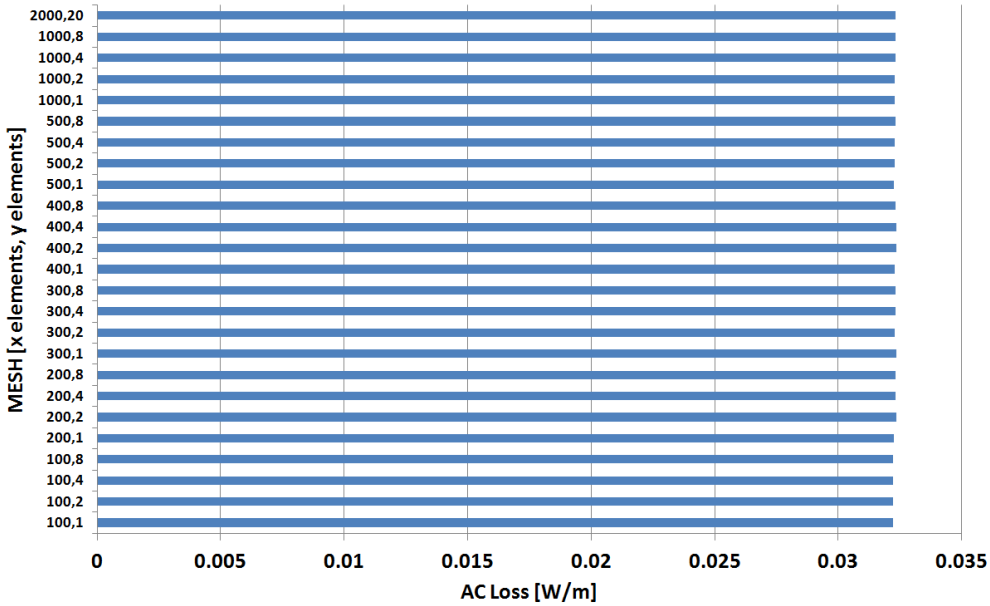

Figure 3.21: Comparison of AC loss calculation for single tape with mapped square/rectangular edge elements, I = 0.9 I_c

3.6.2 Addition of magnetic substrate

The modification of the equations used previously to allow the addition of the magnetic substrate into the model is outlined below.

$$\nabla \times \mathbf{E} = -\frac{\mathrm{d}\mathbf{B}}{\mathrm{dt}} = -\frac{\mathrm{d}(\mu_0 \mu_\mathrm{r} \mathbf{H})}{\mathrm{dt}} \tag{3.10}$$

$$\nabla \times \mathbf{H} = \mathbf{J} \tag{3.11}$$

$$-\frac{\mathrm{dE_z}}{\mathrm{dx}} = -\mu_0 \left(\frac{\mathrm{d}\mu_\mathrm{r}(\mathrm{H})}{\mathrm{dt}} \mathrm{H_y} + \mu_\mathrm{r}(\mathrm{H}) \frac{\mathrm{dH_y}}{\mathrm{dt}} \right) \tag{3.12}$$

$$\frac{\mathrm{dE_z}}{\mathrm{dy}} = -\mu_0 \left(\frac{\mathrm{d}\mu_\mathrm{r}(\mathrm{H})}{\mathrm{dt}} \mathrm{H_x} + \mu_\mathrm{r}(\mathrm{H}) \frac{\mathrm{dH_x}}{\mathrm{dt}} \right) \tag{3.13}$$

Therefore, the subdomain settings to be used in Comsol become

$$\begin{bmatrix} 0 & 0 \\ 0 & 0 \end{bmatrix} \frac{\mathrm{d}^2 \mathbf{u}}{\mathrm{dt}^2} + \begin{bmatrix} \mu_r \mu_0 & 0 \\ 0 & \mu_r \mu_0 \end{bmatrix} \frac{\mathrm{d}\mathbf{u}}{\mathrm{dt}} + \bigtriangledown \cdot \begin{bmatrix} 0 & \mathrm{E_z} \\ -\mathrm{E_z} & 0 \end{bmatrix} = \begin{bmatrix} -\mu_0 \frac{\mathrm{d}\mu_r}{\mathrm{dt}} \mathrm{H_x} \\ -\mu_0 \frac{\mathrm{d}\mu_r}{\mathrm{dt}} \mathrm{H_y} \end{bmatrix}$$

which is solved iteratively by the solver.

To include the field dependence of the relative magnetic substrate of the Ni-W ferromagnetic substrate of the RABiTS YBCO coated conductor, the fitting function presented in [72] is used, which is based on the experimental results published in [86]. The function is represented by [72]

$$\mu(\mathrm{H}) = 1 + 30600 \left(1 - \exp(-(\frac{\mathrm{H}}{295})^{2.5}) \right) \mathrm{H}^{-0.81} + 45 \exp\left(-(\frac{\mathrm{H}}{120})^{2.5} \right) \tag{3.14}$$

where H is the amplitude of the magnetic field strength $\mathrm{H} = \sqrt{\mathrm{H_x^2} + \mathrm{H_y^2}}$.

The superconductor hysteretic loss $\mathrm{Q_{sc}}$ is calculated using the critical current density and the electric field distribution across the cross-section of the YBCO layer. For the model including the magnetic substrate, the additional ferromagnetic loss $\mathrm{Q_{fe}}$ is calculated using the fitting function presented in [72], which is again based on the experimental results published in [86]. The loss, in J/cycle/$\mathrm{m^{-3}}$, is calculated based on the maximum value of the magnetic flux

density seen by the substrate and is represented by [72]

$$Q_{fe}(B_{max}) = \begin{cases} 4611.4B_{max}^{1.884} & \text{for } B_{max} \leq 0.164 \\ 210(1 - \exp(-6.5B_{max})^4) & \text{for } B_{max} > 0.164 \end{cases} \quad (3.15)$$

3.6.3 Modelling results

The geometry of the model and its mesh is shown in Figure 3.22. Figure 3.23 shows the calculated AC loss for the following four cases:

1. Individual turns, without magnetic substrate, constant J_c
2. Individual turns, without magnetic substrate, $J_c(B)$ (equation introduced earlier)
3. Individual turns, with magnetic substrate, constant J_c
4. Individual turns, with magnetic substrate, $J_c(B)$

The substrate loss is indicated by the dotted lines. The $J_c(B)$ dependence increases the AC loss as the magnetic flux front penetrates further into the stack of tapes along the y axis due to the reduced J_c from the edges inwards where the magnetic field is strongest. The inclusion of the magnetic substrate in the model also increases the AC loss, but not necessarily due to the ferromagnetic substrate loss itself, and the reason for the loss increase is discussed in more detail below.

For the range of current investigated (5-50 A), the substrate is saturated (or very close to saturation), and the loss in the superconductor layer is larger than the substrate loss by an order of magnitude or higher for current in excess of about 20 A (20% of the tape I_c, 40% of the coil I_c). In this range, the effect of the substrate loss itself on the overall AC loss is minimal and can be neglected; however, for low current, the substrate loss cannot be neglected, and can indeed exceed the superconductor hysteretic loss for a suitably low current. Additionally, the total AC loss for the model with the magnetic substrate and B-dependent J_c can be seen to be the sum of the AC loss calculated in the constant J_c/substrate and $J_c(B)$/no substrate models. It is also interesting to note that the results

shown in Figure 3.16 are in fact higher than when the actual thickness is used, which is consistent with the results from the artificial expansion analysis.

Figures 3.24 and 3.25 show the magnetic flux density profiles of the magnetic field perpendicular to the tape faces $|B_y|$, which has the greatest impact on the AC loss due to the large aspect ratio of the coated conductor, for models excluding and including the magnetic substrate, respectively, both with $J_c(B)$. Without a magnetic substrate, the magnetic flux front penetrates from the edges of the tape towards the centre in a fairly consistent manner from the top tape in the stack to the bottom. However, when the magnetic substrate is included, the flux front changes shape to an almost triangular one, and penetrates furthest in the middle of the stack and least in the top and bottom tapes. The same trend is observed when a constant J_c is used, which is not included here.

The increase in loss can be attributed to (1) the increased penetration into the middle of the stack, and (2) the higher magnetic flux density within the penetrated region of the superconducting tapes. The higher magnetic flux density in the superconductor is due to the presence of the magnetic substrate and the increased penetration arises due to a local region of large permeability around the middle of the entire stack at the peak of the input current - although the magnetic field strength $|H|$ in this region is relatively low in comparison to $|H_{max}|$ for the whole stack ($< 10^4$A/m) according to the previous equation for the relative permeability, the peak in this curve is around 400 A/m. As shown in Figure 3.23, the contribution of Q_{fe} is negligible.

Figure 3.26 shows a comparison of the AC loss for tapes at different locations within the stack (here 1/4 refers to the 12th tape from the top of the stack and 3/4 refers to the 38th tape). The difference in the AC loss between tapes is minimal for no magnetic substrate and a triangular distribution (with highest loss in the middle tapes) can be observed when the magnetic substrate is present. The overall loss is significantly higher in the latter case, when compared to the former.

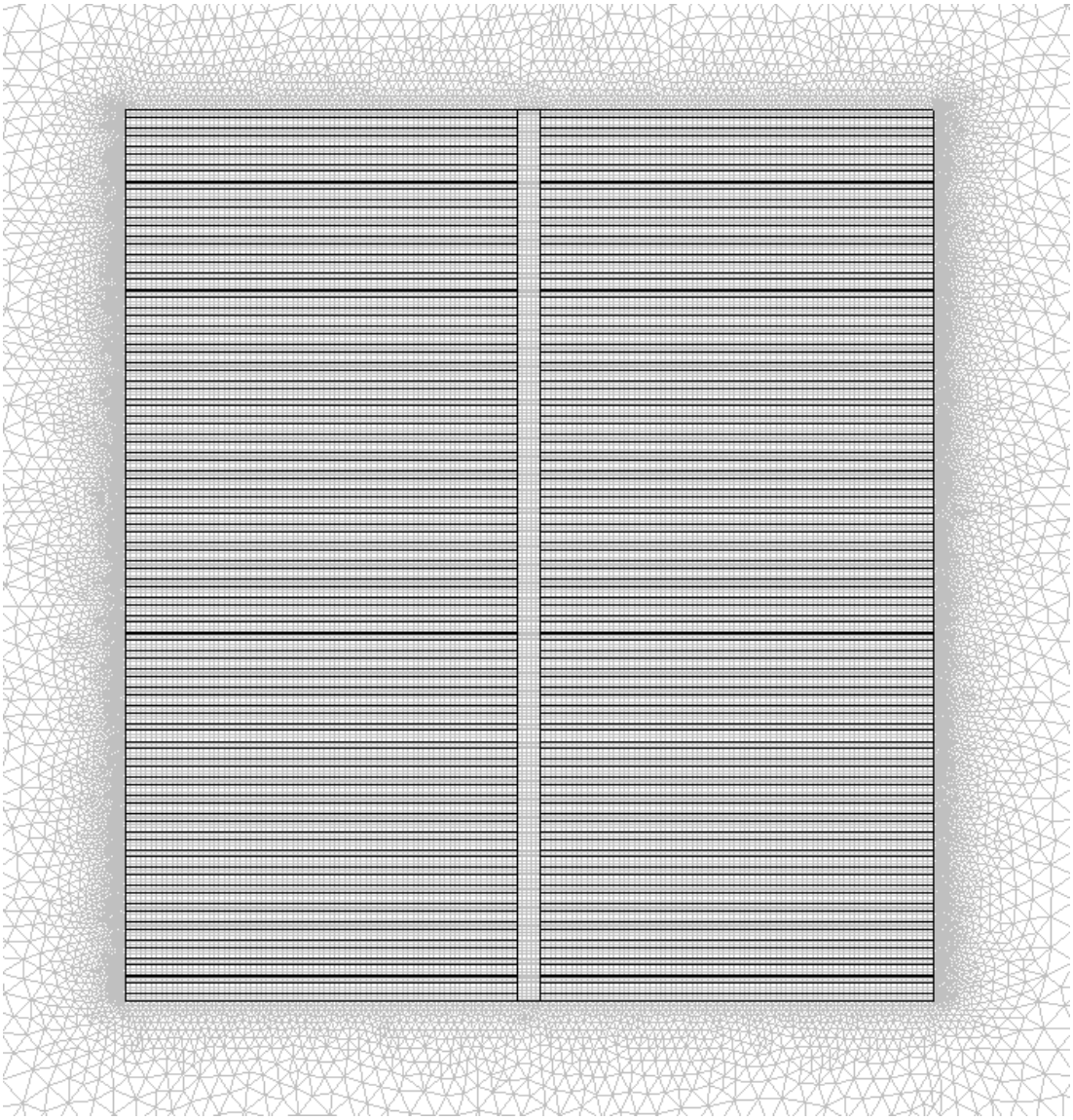

Figure 3.22: Model geometry and mesh using the actual thickness for the YBCO layer and including the magnetic substrate

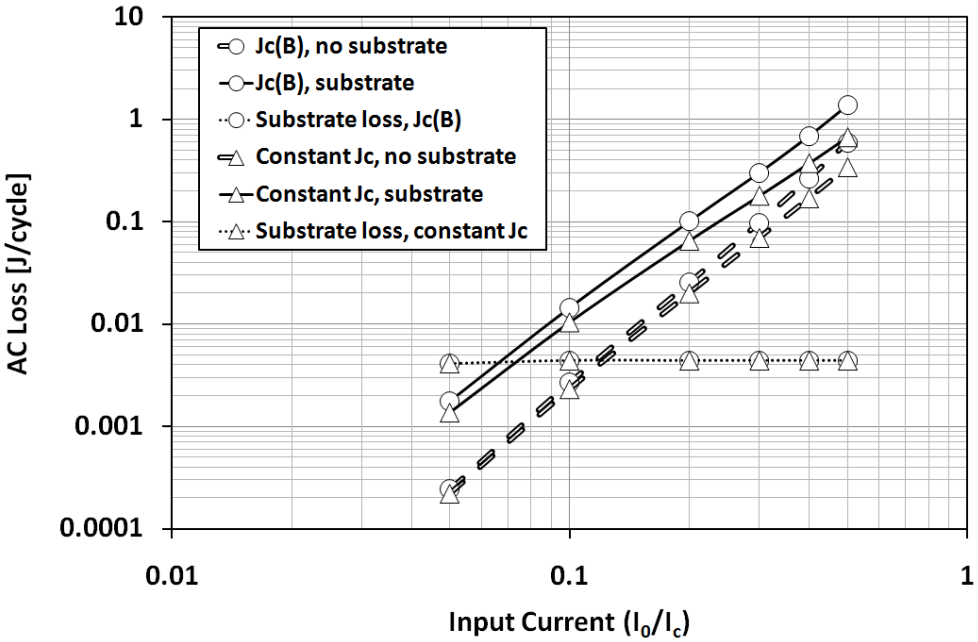

Figure 3.23: Comparison of calculated AC loss for the four cases (J_c and $J_c(B)$ for inclusion/exclusion of magnetic substrate)

3.6.4 Implication of results for motor performance

The AC losses must be kept to a very low level because the heat produced at the low temperatures required to maintain superconductivity requires a certain amount of refrigeration power. An important advantage of HTS materials is the possibility of operating temperatures well above 20 K, which leads to a significant reduction in the required refrigerator input power. The maximum theoretical efficiency attainable is the Carnot efficiency, given by [87]

$$\eta_c = \frac{T_{op}}{T_{amb} - T_{op}} \tag{3.16}$$

where T_{op} is the operating temperature of the refrigerator and T_{amb} is the ambient temperature. The input power P_{in} required to remove a heat load dQ/dt, considering an ideal, reversible cooling cycle, is [87]

$$P_{in} = \frac{1}{\eta_c}\frac{dQ}{dt} \tag{3.17}$$

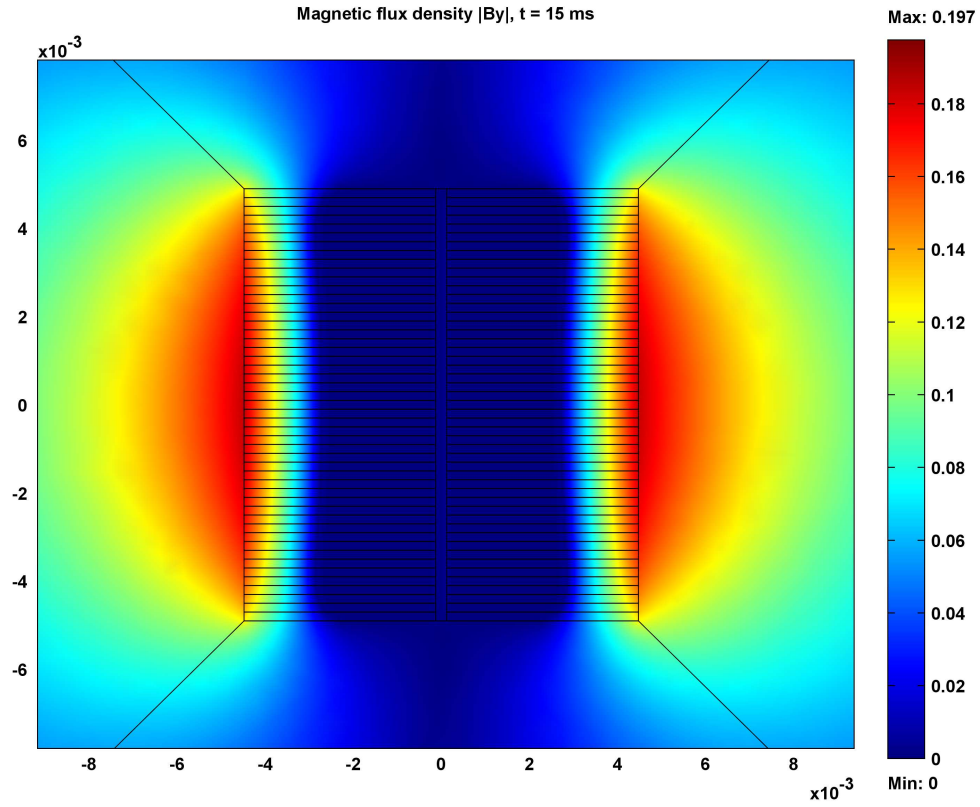

Figure 3.24: Magnetic flux density profile of the magnetic field perpendicular to the tape faces $|B_y|$ without a magnetic substrate and with $J_c(B)$ at t = 15 ms (peak of applied current $|I_0| = 50$ A)

Therefore, for a power of 1 W, an ideal, reversible refrigerator would consume 2.9 W at 77 K, 14 W at 20 K and 70.4 W at 4.2 K. In order to account for the inefficiency of the cooler, as the efficiency of a real refrigerator is much smaller than the Carnot efficiency, a multiplication factor should be introduced between 20 - 50 for operation at 77 K [88]. Large coolers are more efficient (say up to 20 or 30%), but efficient coolers are more expensive. For a small refrigerator able to remove 1 W, the refrigerator efficiency is only a few percent of the Carnot efficiency [87].

Here, a comparison is made between the superconducting coil's transport AC loss and the resistive loss of a similar coil wound with a room temperature

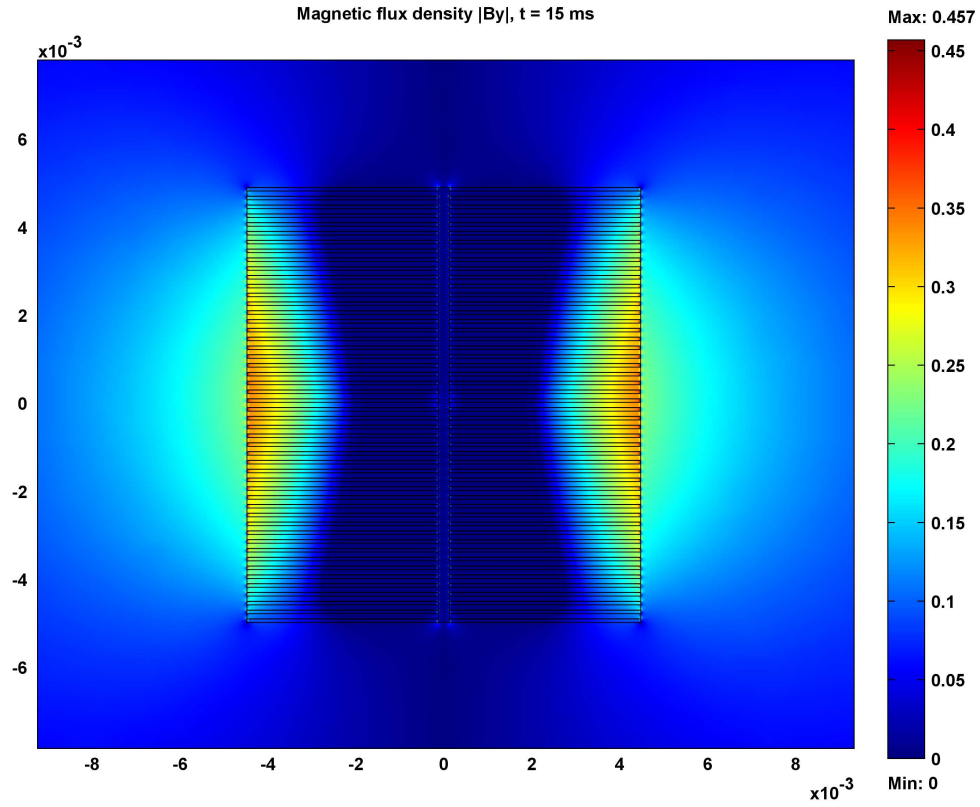

Figure 3.25: Magnetic flux density profile of the magnetic field perpendicular to the tape faces $|B_y|$ with a magnetic substrate and with $J_c(B)$ at t = 15 ms (peak of applied current $|I_0|$ = 50 A)

copper conductor. Although the ductility of copper allows for better distribution of the coil windings within the stator of an electric machine, in order to simplify the analysis, the same coil dimensions as the superconducting coil are assumed, including the same length of conductor, i.e. 60 m. The resistivity of copper can be calculated by $R = \frac{\rho l}{A}$ where $\rho = 1.68 \times 10^{-8}$ Ω m (at 20°C), l = 60 m and $A = \pi\ r^2$. Here r is the radius of the conductor required to carry a maximum current (in rms) comparable to the critical current of the superconducting coil. For example, AWG five wire (diameter 4.62 mm) carries a maximum 47 A_{rms} current [89]. Using the previous equation, the resistance is 0.0601 Ω. Therefore, for I = 50 A_{peak} (35.35 A_{rms}), P = 75.13 W; for I = 40 A_{peak} (28.28 A_{rms}), P =

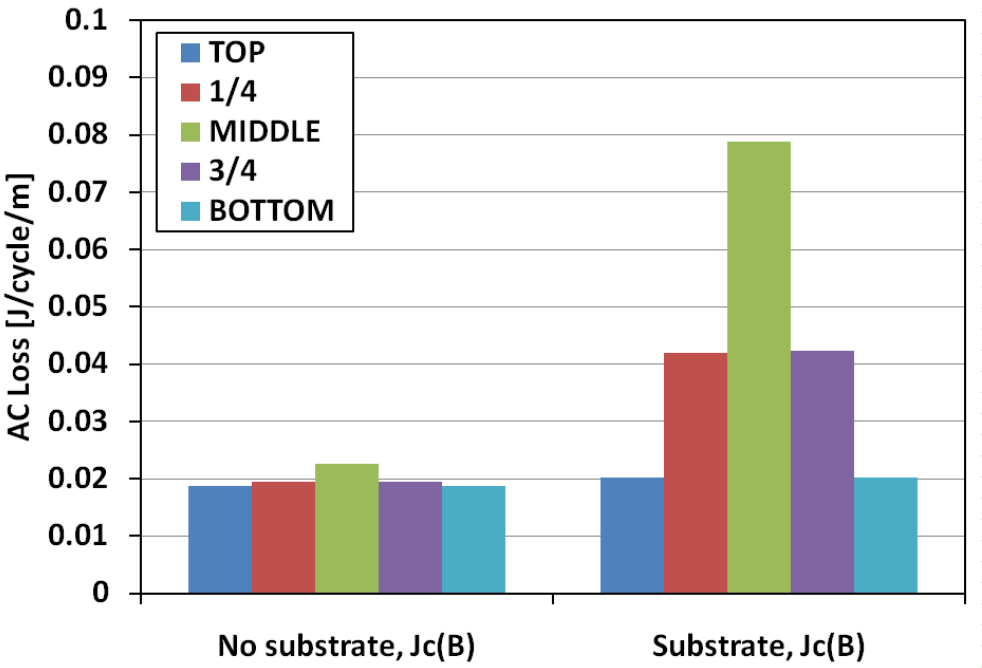

Figure 3.26: Comparison of AC loss for tapes at different locations within the cross-section for $J_c(B)$ models with and without a magnetic substrate for an applied current $I_0 = 50$ A

48.08 W; and so on.

A comparison of the simulation results and the equivalent copper coil is shown in Figure 3.27. The superconducting coil AC losses are reflected to room temperature by $P_{ref} = 20\ P_{AC}$ (at 77 K), which assumes a refrigerator efficiency of around 15%, and is given in units of W, assuming a frequency of 50 Hz. This shows that at least an order of magnitude reduction in the AC loss is required for the coil to have comparable performance to that of copper at power frequencies such as 50 Hz. Reducing the frequency of supply to the machine to a few Hz will also reduce the loss by an order of magnitude, making it feasible for this type of coil to be used in high torque, low speed applications, such as wind turbines.

A comparison can also be made between the transport AC loss reflected to room temperature and the output power of the motor. In [90], the output power of the machine was calculated as 4.52 kW for an electrical loading of 40 A_{peak} and a trapped field in the rotor poles (comprising YBCO bulks) of 0.4 T. In the

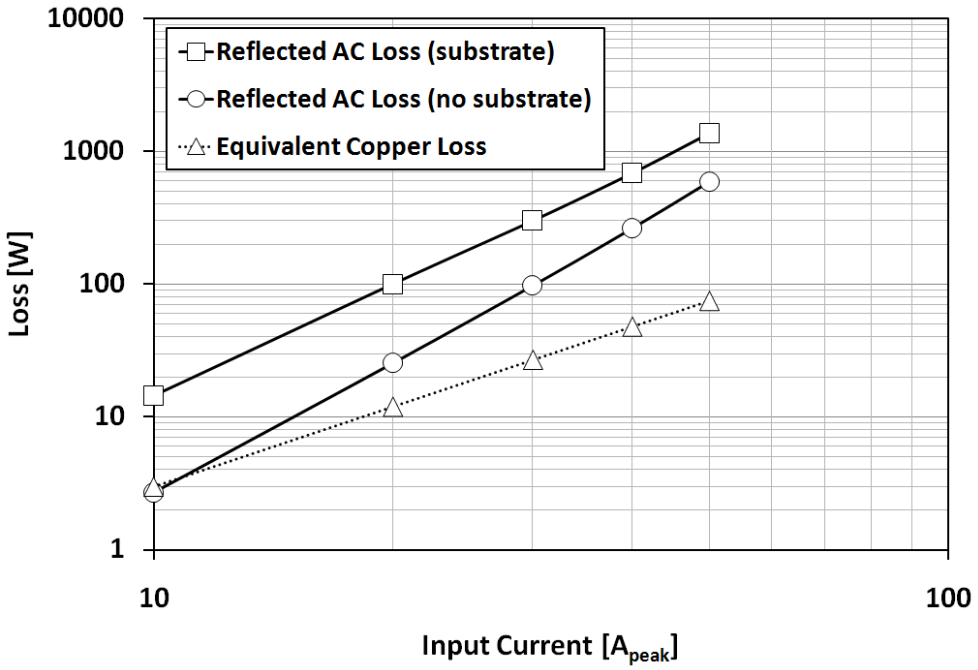

Figure 3.27: Comparison of the superconducting coil transport AC loss (J_c(B) models with and without the magnetic substrate) with an equivalent copper coil

machine design there are six stator coils, meaning the total reflected transport AC loss of the superconducting PMSM is $P_{total} = 6 \times 20 \times P_{AC}$. Therefore, for 40 A_{peak}, the total reflected loss is 1.59 kW (no substrate, J_c(B) model) and 4.14 kW (substrate, J_c(B) model), and these correspond to approximately 35% and 92% of the motor output power, respectively. For 20 A_{peak}, the output power was calculated to be 2.26 kW [90], so the reflected loss (153 W - no substrate, 602 W - substrate) corresponds to approximately 7% and 27 % of the motor output power, respectively.

From these results, it is clear that serious investigations need to be carried out in the area of AC loss mitigation for all-superconducting machine design. For example, shielding using superconducting or magnetic materials, or tape striation. This topic will be explored further in Chapter 5. The magnetic flux density profile for coils wound with a magnetic substrate raises some interesting points for further analysis, which will be investigated in the following section.

3.7 Detailed investigation on stacks with magnetic substrates

In this section, a detailed investigation into the effect of a magnetic substrate on the transport AC loss is carried out. The number of tapes in each stack is varied from 1 to 150, and three types of substrate will be compared: non-magnetic, weakly magnetic and strongly magnetic. The model makes use of symmetry, as shown in Figure 3.28, where only one quarter of the stack is required by setting appropriate boundary conditions. The left-most boundary condition is $H_y = 0$ (along the y-axis) and the bottom boundary condition is $H_x = 0$ (along the x-axis). The constant J_c approximation is used in these models in order to simplify the comparison between models and to compare the results with analytical models.

To model a weakly magnetic substrate, e.g. the Ni-W ferromagnetic substrate of the RABiTS YBCO coated conductor, the same relative magnetic permeability and ferromagnetic loss is used as described above. To include a strongly magnetic Ni-alloy substrate, the following fitting function is used, which is based on the experimental results published in [86]. The fitting function has been selected such that it provides reasonable values for the permeability when the magnetic field is either very small or very large. For the strongly magnetic substrate, there is not a significant difference between the relative permeability at 77 K and that at room temperature [86].

$$\mu(H) = 1 + 120000 \left(1 - \exp(-(\frac{H}{70})^{3.2})\right) H^{-0.99} \tag{3.18}$$

For the strongly magnetic substrate, the additional ferromagnetic loss Q_{fe} is calculated using the following fitting function, which is again based on the experimental results published in [86].

$$Q_{fe}(B_{max}) = \begin{cases} 171.2 B_{max}^{1.334} & \text{for } 0.1 \leq B_{max} \leq 1.53 \\ 375(1 - \exp(-(\frac{B_{max}}{1.407})^{6.787})) & \text{for } B_{max} > 1.53 \end{cases} \tag{3.19}$$

Figure 3.29 shows the experimental data and fitted function for the relative magnetic permeability of a strongly magnetic substrate and Figure 3.30 shows

the substrate loss. The strongly magnetic substrate can be seen to saturate at $B_{max} \approx 1.7$ T. The weakly magnetic substrate saturates at $B_{max} \approx 0.2$ T [72].

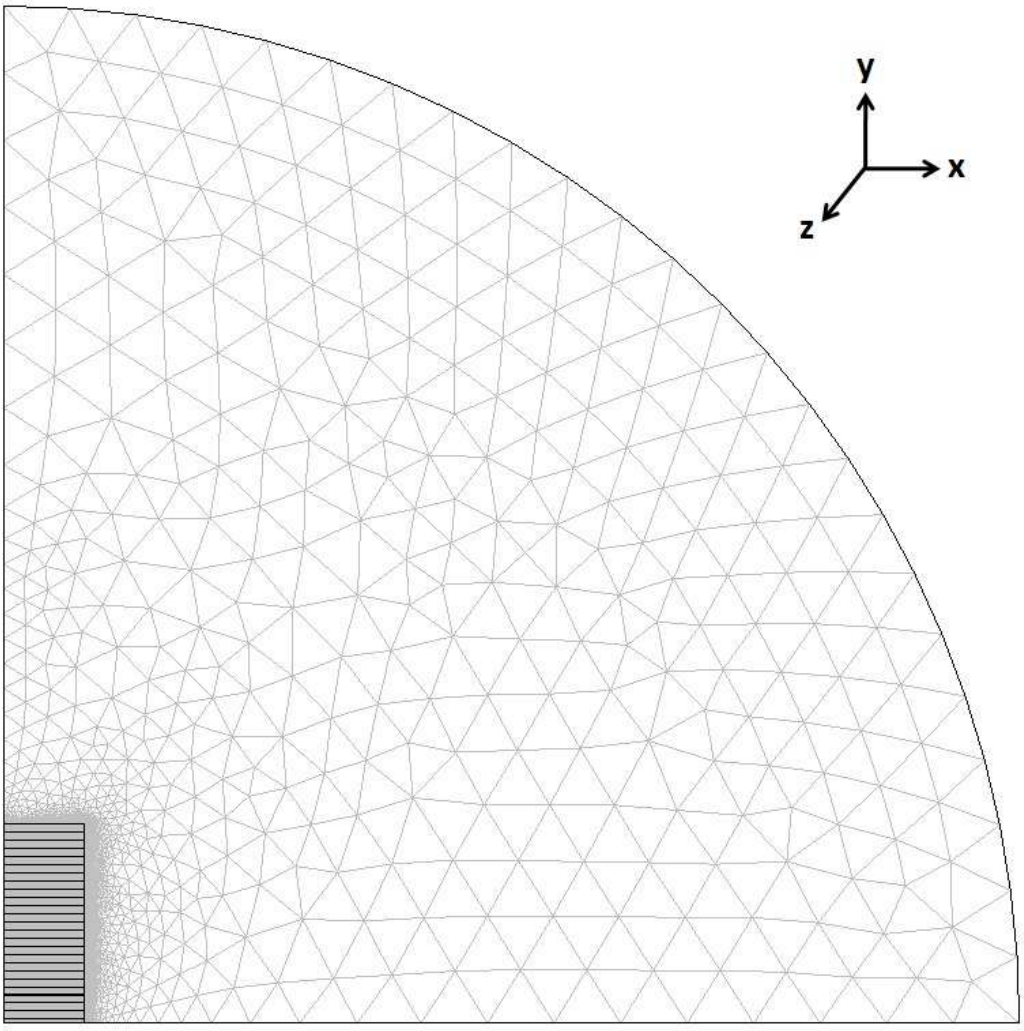

Figure 3.28: 2D symmetric model geometry without a magnetic substrate and using the actual thickness for the YBCO layer (shown is the 50 tape stack)

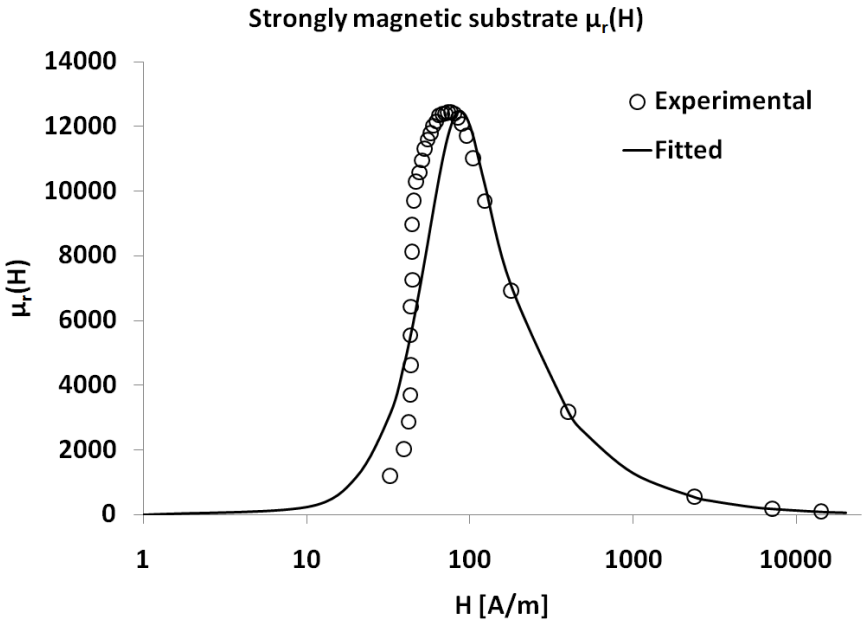

Figure 3.29: Relative magnetic permeability μ_r(H) for a strongly magnetic substrate

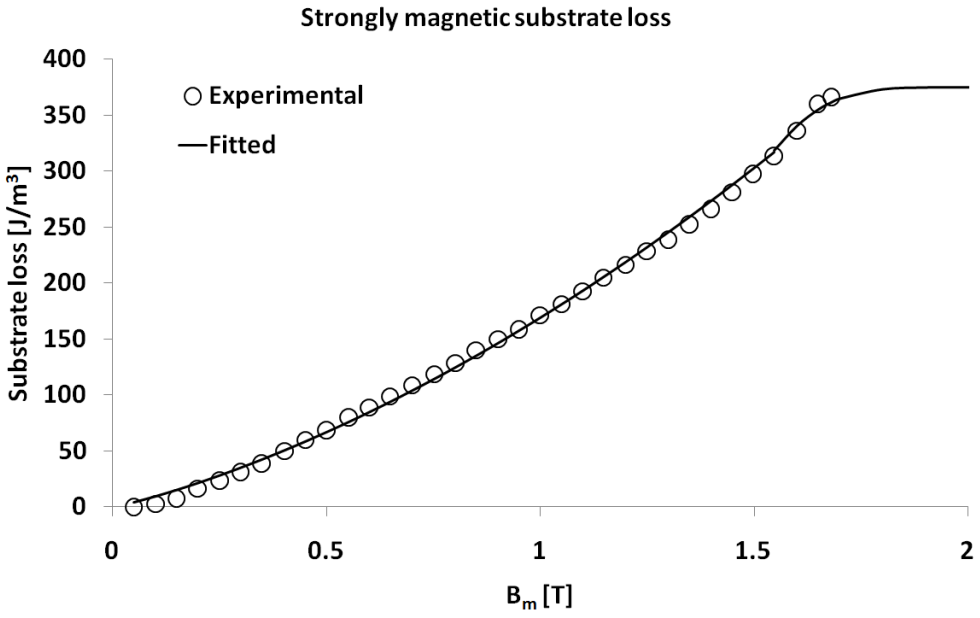

Figure 3.30: Ferromagnetic substrate loss Q_{fe} for a strongly magnetic substrate

3.7.1 Stack AC loss comparison of symmetric FEM and analytical models

Figure 3.31 shows the total transport AC loss per unit length for the symmetric non-magnetic substrate stack model for a transport current with magnitude varying from 10% to 90% of the critical current of a single coated conductor. In order to compare the model with existing techniques, the result for the single tape model is compared with Norris [51], and the Clem infinite stack model [66] is utilised as the limiting value for a significantly large stack. The model agrees well with the Norris equation for a single tape, as found previously in [29, 62], for example, and as the number of tapes increases past 150, the AC loss calculation tends asymptotically towards the result for the Clem infinite stack model. Similar graphs are presented in [70, 71] with identical conclusions for other models based on the minimum magnetic energy variation (MMEV) method [70] and the infinitely thin approximation based on a variational formulation of the Kim critical-state model [71].

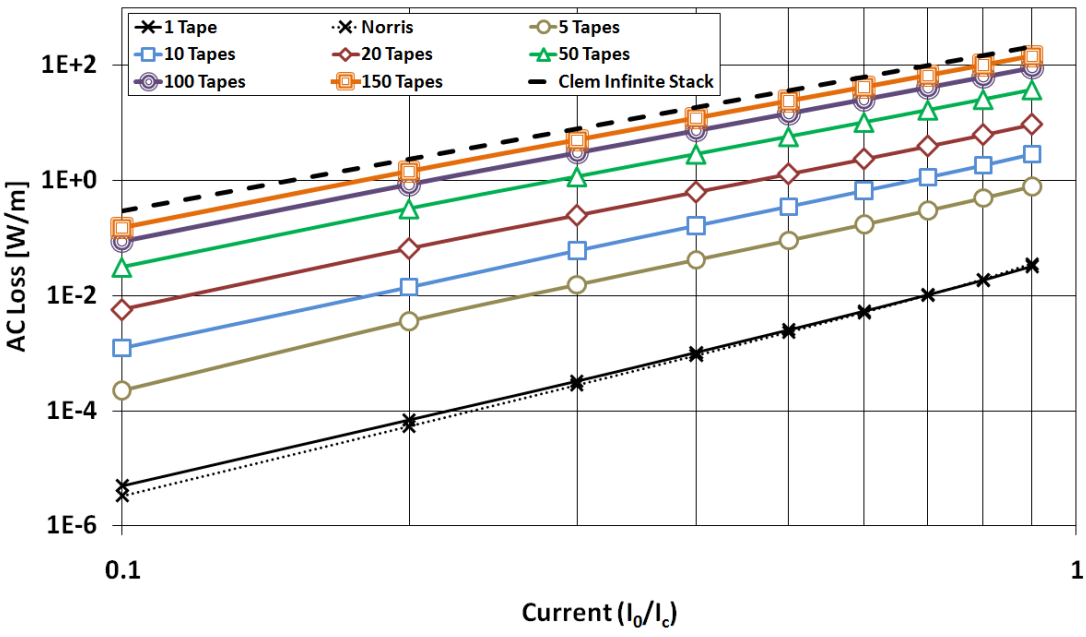

Figure 3.31: Comparison of symmetric non-magnetic substrate stack model with Norris (single tape) and Clem (infinite stack) models

3.7.2 Stack AC loss comparison with and without magnetic substrates

Here the total AC loss per unit length of stacks of tapes is compared for tapes with (for both weak and strong cases) and without a magnetic substrate. As described previously, the total AC loss comprises the superconductor hysteretic loss Q_{sc} and the ferromagnetic loss Q_{fe}. These separate components are shown on each of the following figures. The transport current is varied between 10% and 90% of the critical current of the single tape. Figures 3.32, 3.33 and 3.34 show the comparison of the total AC loss for a stack of 5, 50 and 150 tapes, respectively. As shown in Figure 3.32, even for a stack with a relatively small number of tapes, the superconductor hysteretic loss tends to dominate the ferromagnetic loss. However, the hysteretic loss is different depending on the type of substrate used. The presence of the magnetic substrate increases the loss due to increased penetration of the magnetic field into the stack (particularly at the centre) and higher magnetic flux density within the penetrated region. The stronger the magnetism of the substrate, the higher the transport AC loss in the stack. In the following section, the AC loss in certain locations of the stack is shown, which confirms these findings. The results suggest that for practical applications, where AC transport current is involved, superconducting coils should be wound where possible using tapes with a non-magnetic substrate to reduce the total AC loss of the coil.

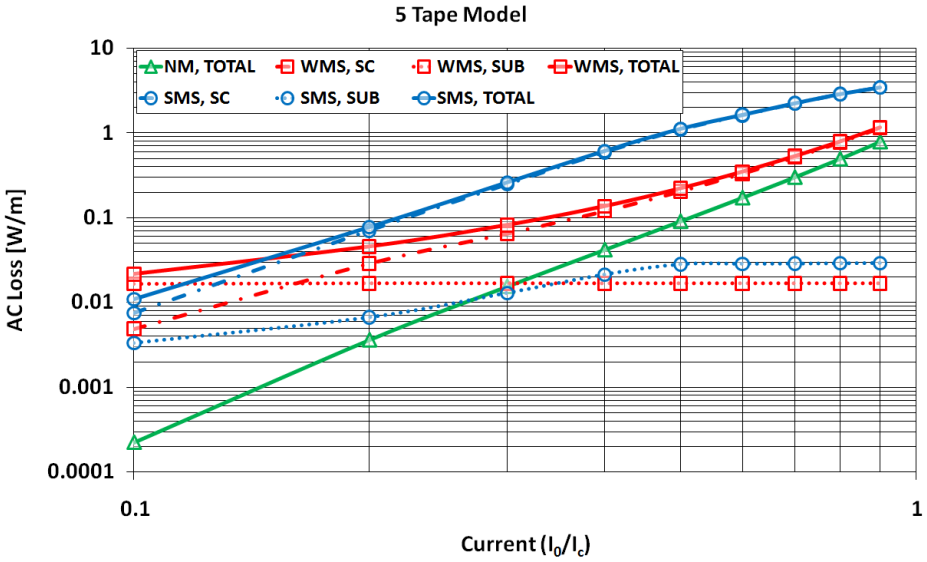

Figure 3.32: Comparison of AC loss in a stack of 5 tapes with and without a magnetic substrate (weak/strong) [NM = non-magnetic, WMS = weakly magnetic substrate, SMS = strongly magnetic substrate; TOTAL = total loss, SC = superconductor hysteretic loss, SUB = ferromagnetic substrate loss]

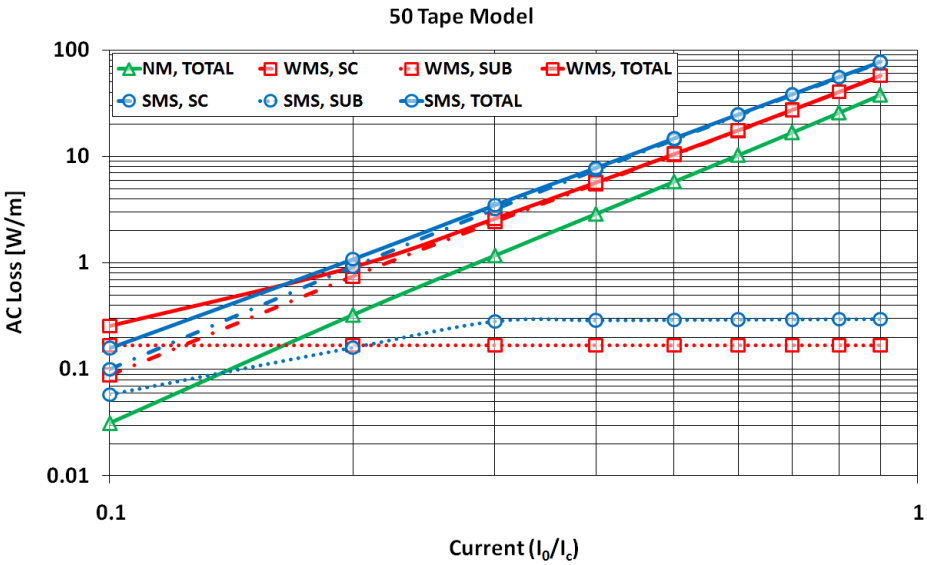

Figure 3.33: Comparison of AC loss in a stack of 50 tapes with and without a magnetic substrate (weak/strong)

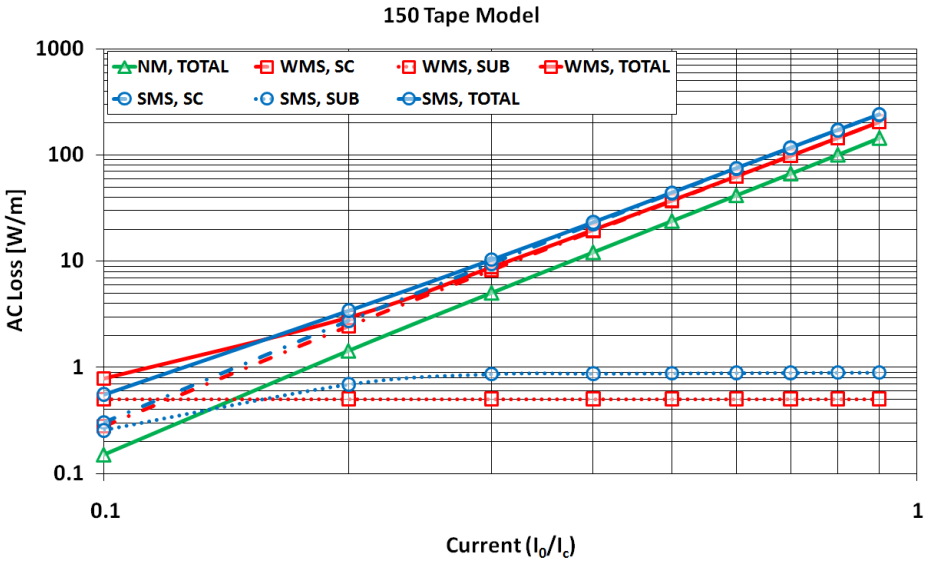

Figure 3.34: Comparison of AC loss in a stack of 150 tapes with and without a magnetic substrate (weak/strong)

3.7.3 AC loss in individual tapes for stacks with/without magnetic substrates

Here the superconductor hysteretic loss per cycle per unit length for individual tapes within each stack is evaluated to show how the presence of a magnetic substrate affects the magnetic field penetration, which directly affects the AC loss within the stack. The tape locations evaluated are the middle tape, and tapes at positions one-fifth and three-fifths from the top to the middle tape; for example, in the 100 tape stack, these correspond to the 10th, 30th and 50th tapes, respectively. By symmetry, the loss in the tapes in the corresponding positions mirrored from the middle tape is the same.

Figure 3.35 shows a comparison of the AC loss for non-magnetic (top), weakly magnetic (middle) and strongly magnetic (bottom) substrates. It is clear that the presence of a magnetic substrate increases the superconductor hysteretic loss in the middle tape, where there is a higher localised magnetic flux density. There is also an increase in loss at the 1/5 and 3/5 points, but the magnitude of this increase varies between the weakly and strongly magnetic substrates, with the

presence of the strong magnetic substrate resulting in an increase in loss throughout the entire stack. However, for significantly large stacks (100 tapes or more), the middle and 3/5 point losses become comparable, regardless of whether the magnetic substrate is weak or strong. The loss tends to be lowest in the tapes towards the top of the stack for most cases.

In order to understand why the loss profile is as described; the magnetic flux penetration can be investigated using a field profile, along with the current density distribution across tapes. Figures 3.36 and 3.38 show the magnetic flux penetration in the tapes at the 1/5 point and middle for the 20 tape and 100 tape stacks, respectively, and figures 3.37 and 3.39 show the current density distribution across these tapes for the same stacks.

For the 20 tape stack, there is a clear increase in penetration into the stack when a magnetic substrate is present, as well as a higher magnetic flux density. The strongly magnetic substrate results in further penetration at the 1/5 position as well. However, for the weakly magnetic substrate, the flux penetration at this position is similar to the case where no magnetic substrate is present, but with slightly less penetration and a higher slope. This corresponds to the triangular flux penetration characteristic observed previously. The current density distributions in Figure 3.37 show an increased current density at the edges in the central tape when a magnetic substrate is present, which corresponds to the characteristics of the magnetic flux penetration described above. This higher current density results in a higher electric field, which increases the AC loss.

For the 100 tape stack, the magnetic flux penetrates a similar distance into the stack at the centre for all substrates (non-magnetic and magnetic), but the presence of the magnetic substrate results in a higher slope. The similar penetration distance may be due to the local magnetic flux density approaching the irreversibility field. This results in the slightly higher current density distribution at the edges, as shown in Figure 3.39. For the tape at the 1/5 position, there is slightly increased penetration with a higher slope for the strongly magnetic substrate, indicating a higher magnetic flux density and further penetration into the stack overall.

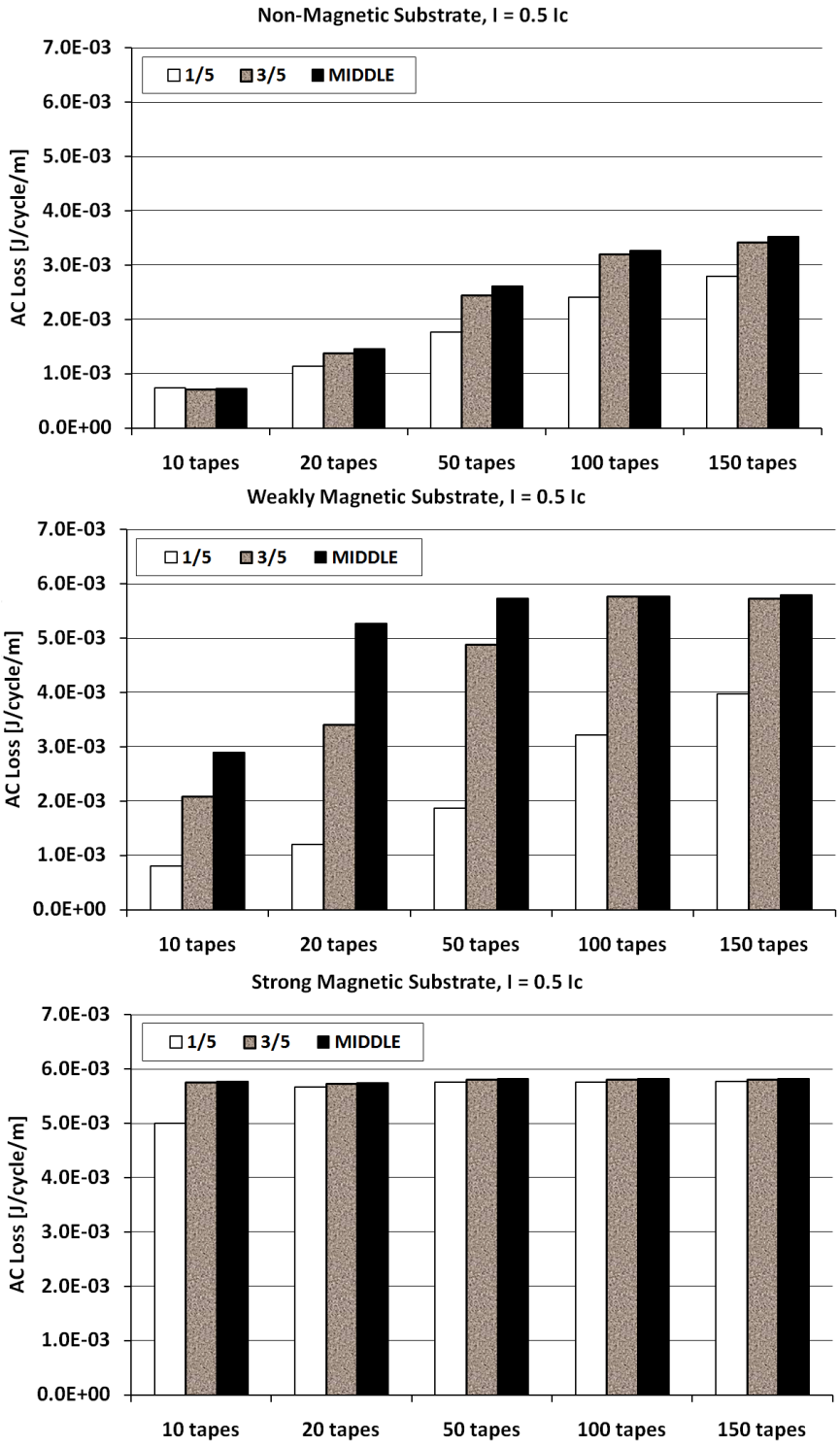

Figure 3.35: Comparison of AC loss in certain tapes (1/5, 3/5 and middle tapes) within stack of tapes with a non-magnetic substrate (top figure), a weakly magnetic substrate (middle figure), and a strongly magnetic substrate (bottom figure)

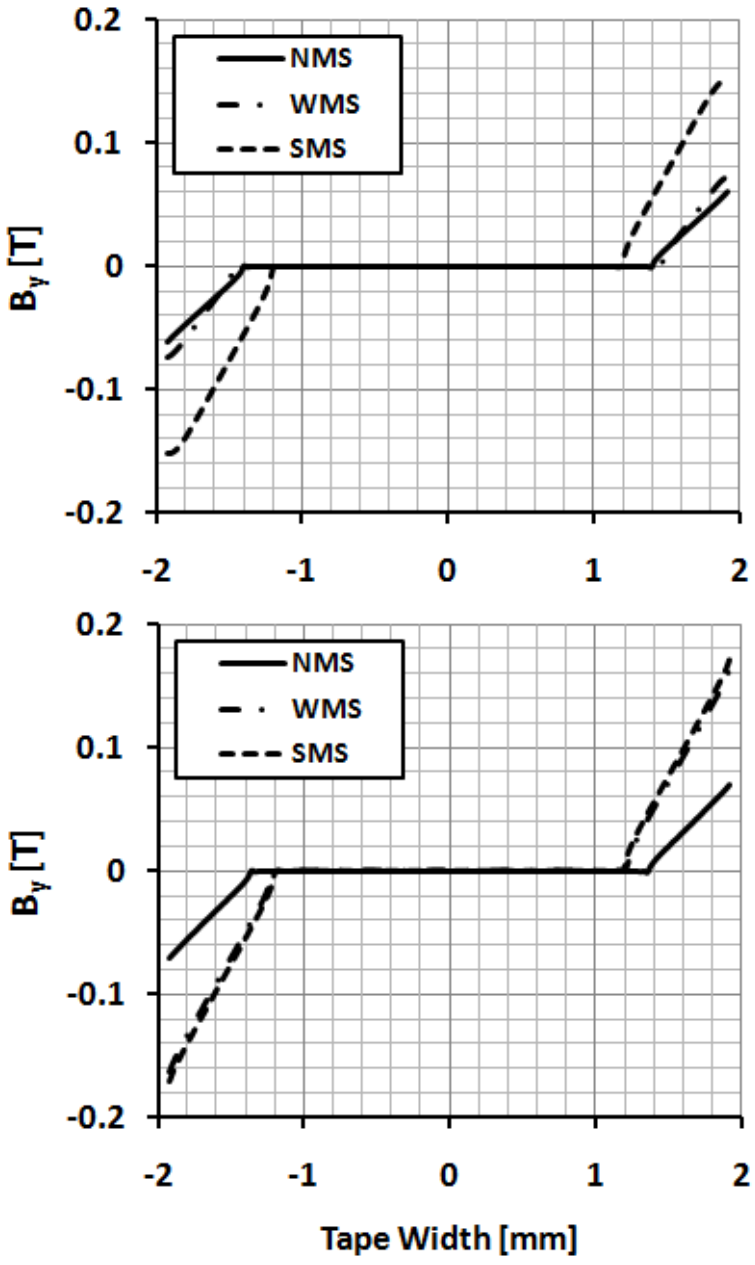

Figure 3.36: Magnetic flux penetration in tapes located at 1/5 between the top (top figure) and centre (bottom figure) for the 20 tape stacks [NMS = non-magnetic substrate, WMS = weakly magnetic substrate, SMS = strongly magnetic substrate]

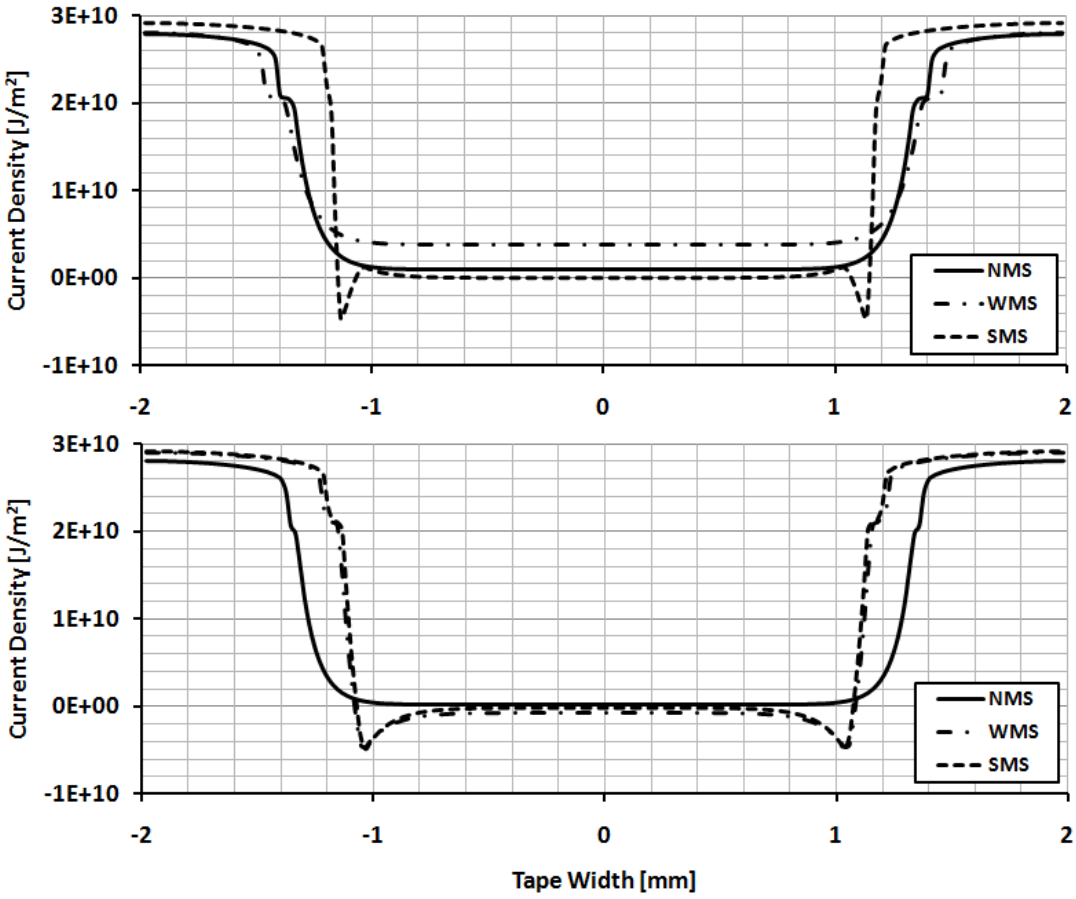

Figure 3.37: Current density distribution in tapes located at 1/5 between the top (top figure) and centre (bottom figure) for the 20 tape stacks [NMS = non-magnetic substrate, WMS = weakly magnetic substrate, SMS = strongly magnetic substrate]

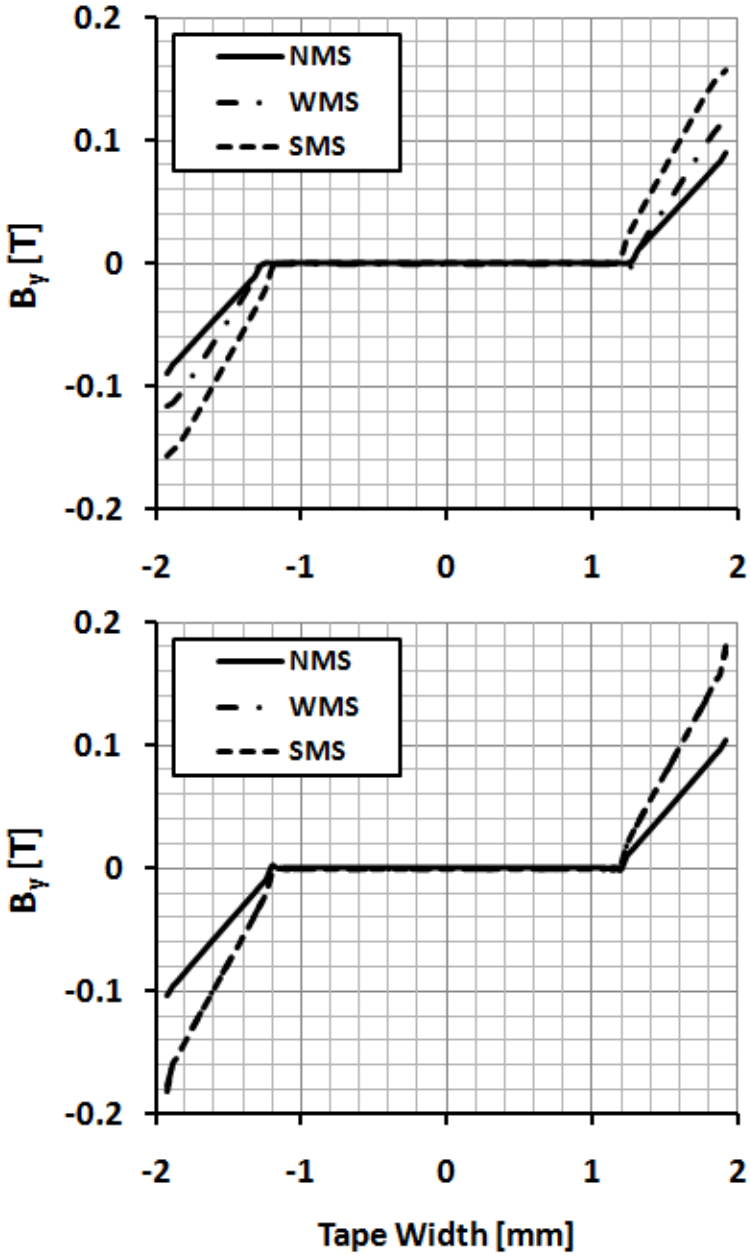

Figure 3.38: Magnetic flux penetration in tapes located at 1/5 between the top (top figure) and centre (bottom figure) for the 100 tape stacks [NMS = non-magnetic substrate, WMS = weakly magnetic substrate, SMS = strongly magnetic substrate]

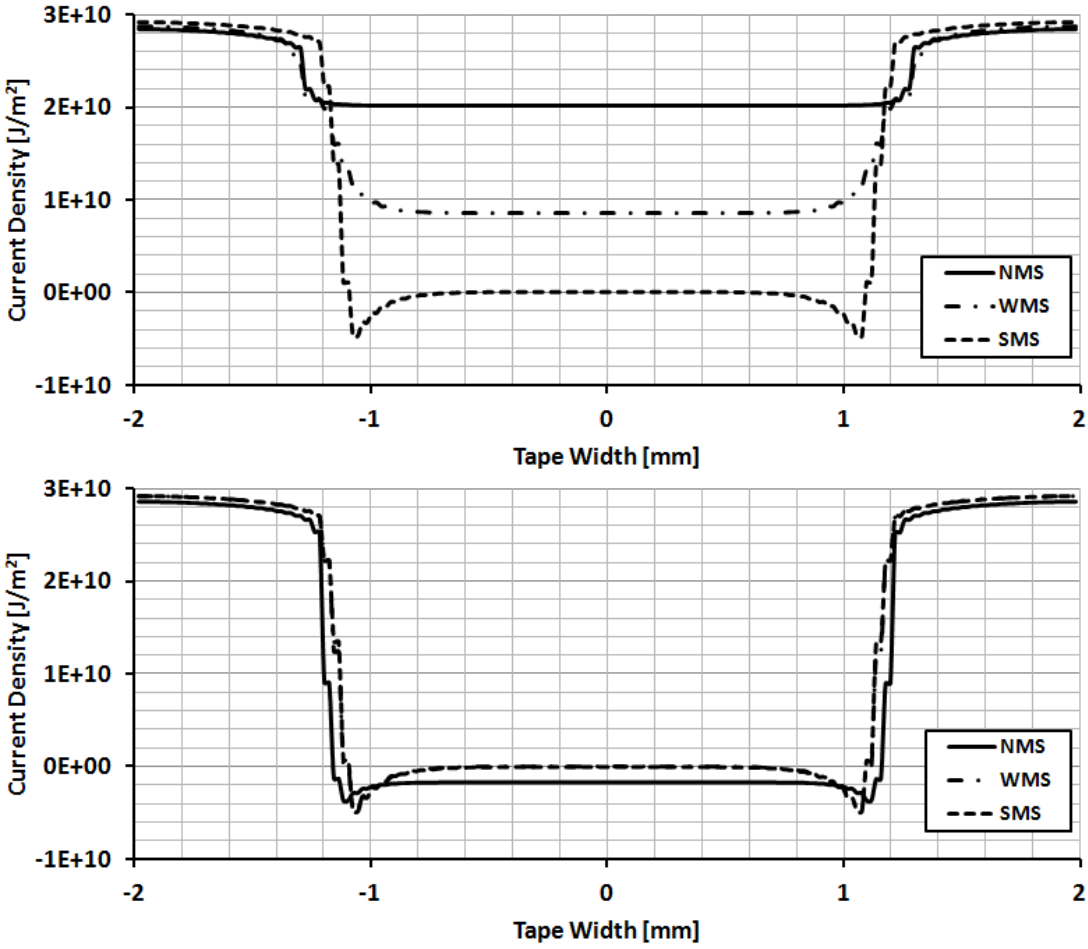

Figure 3.39: Current density distribution in tapes located at 1/5 between the top (top figure) and centre (bottom figure) for the 100 tape stacks [NMS = non-magnetic substrate, WMS = weakly magnetic substrate, SMS = strongly magnetic substrate]

3.8 Summary of refinements

In this chapter, the modelling of HTS-based superconducting coils using the finite element method was described in detail. The numerical model is based on solving a set of Maxwell's equations in 2D implementing the H formulation using the commercial software package Comsol Multiphysics. The coil cross-section is modelled as the number of individual turns in the coil. A number of different aspects of the model were investigated in order to deduce the optimum parameters of the model in terms of computational time and accuracy. A summary of the parameters discussed, as well as comments on other aspects not described above, are outlined below.

1. Mesh refinement

   A refined mesh can result in a much longer computational time, but higher stability and a more accurate result. A combination of different kinds of meshes (free and mapped) and using a finer mesh for subdomains where the accuracy of the solution is most critical, i.e. the superconducting layer, can be advantageous. A solution using as fine a mesh as possible within the limits of the computer's memory can be used to verify the solution for coarser meshes.

2. First order edge elements

   The use of first order edge elements results in a faster solution with higher stability and accuracy than using the default Lagrange elements in Comsol.

3. Artificial expansion of tape thickness

   As long as the tape thickness is not artificially increased above a certain limit, the artificial expansion technique can provide an accurate solution with a reduction in the number of mesh elements required, which can significantly reduce the computation time. This idea works because the dynamics of the flux penetration for the tape geometry is essentially along one axis.

4. Critical current density approximations

   A constant J_c approximation for the critical current density of the superconductor provides a simplified model that can be compared with existing analytical models. The Kim model can be adapted to model the dependence of J_c on the magnitude and direction of the magnetic field using manufacturer-supplied or measured experimental data. This results in a more accurate representation of the superconductor's properties, but results in a longer computational time since the model requires additional calculations each time step.

5. E-J power law n value

   Using a small n value in the E-J power law can result in a faster solution, since the material behaves more like a linear material. However, the n value needs to remain within certain limits to adequately represent the superconductor properties since lowering the n value would cause an increase in flux creep. Using a very high n value allows comparison of the results with Bean-like models, but this can cause stability problems as very small changes in magnetic field can result in large variations in the electric field, as described in [56].

6. Magnitude of applied current/field

   In general, a larger magnitude of applied current/field results in a longer computational time, and for small magnitudes of current/field a more refined mesh is required along the y-axis since the current density distribution along the top and bottom of the tape can be of a similar magnitude as the edges.

7. Magnetic substrates

   The underlying equations of the simple superconductor model can be modified to allow the inclusion of a magnetic substrate, which is present in some superconducting tapes. Including the relatively permeability of such substrates increases the number of calculations per time step, but more accurately represents the whole tape properties.

Chapter 4

AC loss measurement

In this chapter, the measurement of AC loss in HTS-based superconducting coils is described in detail, including an experimental setup that uses an electrical technique to accurately measure the transport AC loss of a superconducting coil. The experimental technique is based on the use of a lock-in amplifier to extract the in-phase component of the superconducting coil voltage, which corresponds to the AC loss voltage. In order to compensate for the coil's large inductive voltage, a variable mutual inductance is used. The technique is applied firstly to measure the racetrack coil introduced in the previous chapter. It is found that the experimental results agree with the modelling results for low current, but some phase drift occurs for higher current, which affects the accuracy of the measurement. In order to overcome this problem, a number of improvements are made to the initial setup to improve the lock-in amplifier's phase setting and other aspects of the measurement technique, including the use of the signal generator's reference (TTL) output and a Rogowski coil to provide stable reference signals to accurately set the reference phase of the lock-in amplifier. New measurements are then carried out on a single, circular pancake coil. Discrepancies between the experimental and modelling results are described in terms of the assumptions made in the model and aspects of the coil that cannot be modelled. Finally, some suggestions to improve the experimental setup in the future are presented.

4.1 Overview of techniques

In order to validate the modelling results of the preceding chapter, it is necessary to establish experimental measurement techniques, and there exist a number of different techniques to measure the AC loss in superconductors. There are a number of reasons why the AC loss should be measured: to better understand the physical mechanism(s) of the loss; to investigate AC loss mitigation methods for the wires themselves, as well as at a device design level; to appropriately judge whether a cable/coil/device will be thermally stable; and to estimate the cooling power required, and hence design an appropriate cryogenic system. In this chapter, the measurement of transport AC loss in a superconducting coil is investigated.

AC loss measurement techniques can be divided into three main groups: calorimetric, electrical and magnetisation measurements. These are summarised below.

- Calorimetric

  The dissipated heat (AC loss) of the superconductor is determined indirectly by measuring the temperature rise or the amount of gas boil-off.

- Electrical

  Based on measurement of the component of the voltage in-phase with the current to determine the AC loss, which is seen as a 'resistive' power.

- Magnetisation

  Losses can be determined from the hysteresis loop in the magnetisation curve of the superconductor [91], which can be achieved by integrating signals from pick-up coils wound around or Hall probes placed close to the sample [92].

Measurement techniques are well established for measuring transport and magnetisation AC loss in short samples of wire, and for power applications (usually 50 or 60 Hz), the Hall probe and pick-up coil techniques are most suitable for measuring the magnetisation AC loss, whereas a four-point measurement technique using voltage taps is commonly used to measure the transport AC loss [48].

It is difficult to utilise calorimetric methods for short samples (approximately up to 0.1 m in length) because liquid nitrogen has a large evaporation heat and the heat capacity of materials used at this temperature is increased, compared with lower temperatures, such as that of liquid helium [48]. In [93,94], the calorimetric and electromagnetic methods are compared for measuring the transport AC loss of short samples and it is shown that both approaches yield the same results. More recently, it has been shown these approaches also yield good agreement when measuring the transport AC loss of HTS pancake coils [95].

The calorimetric and electrical methods are best suited to coil AC loss measurements, as it is difficult to utilise the pick-up coils required for the magnetisation method with a complex shape, such as a coil. Calorimetric methods are advantageous for AC loss measurements in complex electromagnetic environments, such as those found in real superconductor-based devices [93], i.e. a combination of an AC or DC applied magnetic field with an AC or DC transport current. However, calorimetric methods have a number of drawbacks in comparison to electrical methods, including the long time to obtain a stationary regime, the extensive calibration required due to heat losses other than the superconductor AC loss, and the fact that individual components of loss cannot be measured [96]. Electrical methods are generally faster and provide greater sensitivity [97], but a major problem when applying this technique to a superconducting coil is the compensation of the much larger inductive component of the coil's voltage compared to the in-phase component.

In the following section, an electrical method is proposed to measure the transport AC loss of HTS-based superconducting coils, and the measurement results are compared with the modelling results.

4.2 Proposed electrical method

The experimental setup is shown in Figure 4.1 and is based on a combination of a modified existing experimental setup used for measuring the transport AC loss of superconducting tapes [80] with a compensation coil to cancel the large inductive component of the superconducting coil voltage, which can be orders of magnitude higher than the in-phase AC loss component [96]. The compensation

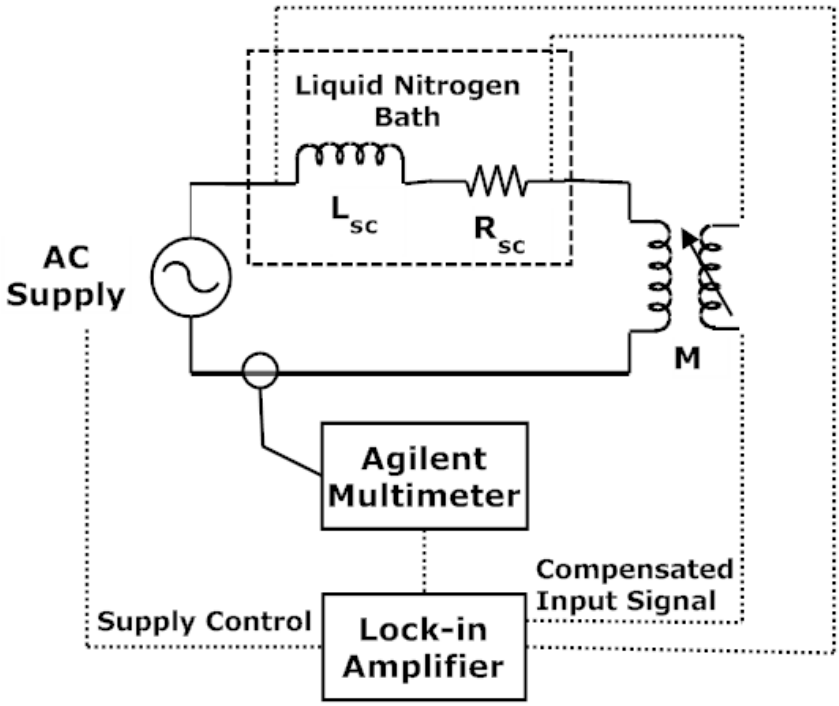

Figure 4.1: Schematic diagram of experimental setup for measuring transport AC loss in superconducting coils electrically

coil needs to provide a high enough compensating voltage with low phase shift and low noise.

Power is supplied via two 400 W KEPCO power supplies connected in parallel (one master, one slave) to provide up to ±20 V, ± 40 A. The output of the power supplies is controlled by the internal oscillator of the lock-in amplifier, which also acts as the lock-in amplifier's reference signal.

The lock-in amplifier can extract a signal with a known carrier wave where the signal-to-noise ratio (SNR) is very small. Lock-in amplifiers use a technique known as phase sensitive detection (PSD) [98] to single out the component of the signal of interest at a specific frequency and phase. It uses mixing, through a frequency mixer, to convert the signal's phase (in reference to the reference signal) and amplitude to a voltage signal, which is then displayed on the lock-in amplifier. To recover a signal at a low SNR requires a strong, clean reference signal at the

same frequency as the input signal, and this reference can be internal (e.g. using the lock-in amplifier's internal oscillator to drive the amplifier) or external.

The current flowing in the circuit is measured by a current transducer connected to an Agilent multimeter, and the input signal to the lock-in amplifier is the compensated superconducting coil voltage. The critical current, measured in [77] and shown in Figure 3.5, is approximately 50 A. The coil is contained within a polystyrene liquid nitrogen bath, and is connected in series with the power supplies and the compensation coil. The signal from the voltage taps at either end of the superconducting coil is connected in series, but with opposite polarity, to the secondary of the compensation coil.

A compensation coil is used, known as inductive compensation, rather than capacitive compensation (for examples, see [48, 99]) to avoid the effects of higher harmonics, which make capacitive compensation very frequency sensitive. It is much easier to design a variable mutual inductance, and any higher harmonics will induce a voltage in the compensation coil in the same way as in the superconducting coil. A voltage divider is not used to reduce the superconducting coil signal [48, 99] as this may introduce a phase shift and reflection [100], so a large mutual inductance must be provided. As thin a wire as possible is used for both the primary and secondary coils to reduce the effect of any induced eddy currents in the windings due to time-varying fields and, for the same reason, no magnetic materials are used in the construction of the coils. The variation of the mutual inductance is achieved by displacing the secondary coils relative to the primary, whose central axes are parallel to each other, which changes the amount of flux linked between the coils.

The compensation coil was designed with a mutual inductance higher than the estimated 3 mH of the racetrack coil. Assuming perfect flux linkage between the primary and secondary coils, the compensation coil mutual inductance was calculated to be 9.4 mH, using

$$\mathrm{M} = \mu_0 \mathrm{N}_1 \mathrm{N}_2 \frac{\pi}{2} \frac{\mathrm{r}_2^2}{\mathrm{r}_1} \tag{4.1}$$

where r_1 and r_2 are the radii of the primary and secondary coils, respectively. This assumes perfect flux linkage between the primary and secondary coils, which

in practice is not achieved (see *Experimental results*). A derivation of this equation is provided in Appendix 2.

The primary coil is wound with 2.18 mm diameter enamelled copper wire with $N_1 = 20$ turns and is 5 cm long. The secondary coil is wound with 0.314 mm diameter enamelled copper wire with $N_2 = 3000$ turns and is also 5 cm long. Thicker wire was used on the primary coil to enable large currents (up to 50 A) through this coil. Plastic plumbing pipe was used as the former for the primary (5 inch pipe) and secondary (4 inch pipe) coils. The compensation coil is shown in Figure 4.2.

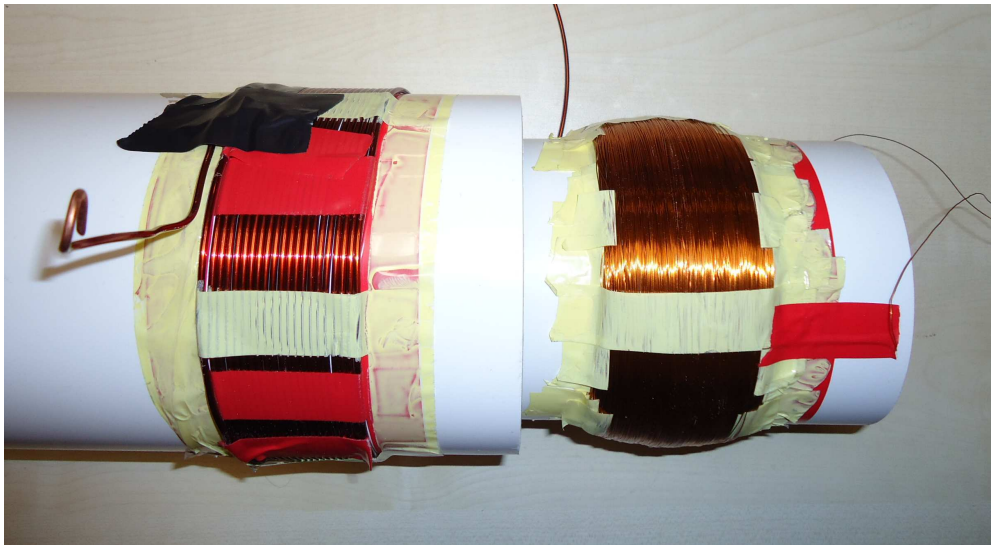

Figure 4.2: Compensation coil (variable mutual inductance) for proposed electrical method

The superconducting coil voltage is compensated such that

$$v_{sc} - v_{comp} = v_{AC} \tag{4.2}$$

where v_{AC} is the AC loss component. The following equation shows the components of the above equation in more detail:

$$\left(i R_{sc} + L_{sc}\frac{di}{dt}\right) - M\frac{di}{dt} = v_{AC} \tag{4.3}$$

Therefore, for complete compensation $L_{sc} = M$. For an input current $i(t) = I_0 \sin(\omega t)$, the inductive voltage across the superconducting coil is $v_L = \omega L_{sc} I_0 \cos(\omega t)$. The resistance of the compensation coil's secondary voltage can be ignored due to the large input impedance of the lock-in amplifier (10 MΩ).

The measured AC loss in J/cycle is calculated using the following equation.

$$Q = \frac{V_{rms} I_{rms}}{f} \tag{4.4}$$

where V_{rms} is the measured voltage across the coil ends, I_{rms} is the transport current flowing through the coil, and f is the frequency of the supply.

4.2.1 Experimental results

The range of the mutual inductance of the compensation coil was measured for various displacement levels of primary versus secondary coil. Using a function generator (50 Hz signal) and an oscilloscope, the mutual inductance was measured to vary between 6.6 mH (no displacement) and 1 mH (9 cm displacement).

The inductance of the superconducting coil was measured by applying a small current (0.6 A) after cooling the coil in the liquid nitrogen bath, and measuring the coil voltage directly with the lock-in amplifier. At such a low current, the superconducting coil voltage is expected to be predominately inductive, but it is important that the current remains low for this measurement as the lock-in amplifier may be damaged by the high inductive voltage presented at the input for higher current. A frequency of 41.7 Hz was used to avoid using a frequency too close to the mains frequency. The inductance was measured as 2.74 mH, close to the estimated 3 mH.

The compensation coil was then connected to the lock-in amplifier (without the superconducting coil) and was adjusted until a voltage equal to the measured superconducting coil voltage was displayed on the lock-in amplifier. The superconducting and compensation coil signals were connected in series, ensuring opposite polarities to cancel the inductive component and achieve the required compensation. The setting of the phase of the lock-in amplifier was performed using its internal reference, which also provides the control signal to the power supply. The phase setting was performed initially, and the same phase was used

for subsequent measurements. The current transducer is used only for the purpose of measuring the magnitude of the current flowing in the circuit and does not provide a reference to the lock-in amplifier. The experimental results for two sets of measurements are shown in Figure 4.3 and these results are compared with the model with $J_c(B)$ and including the magnetic substrate. The power supply described above was able to provide up to approximately 25 A.

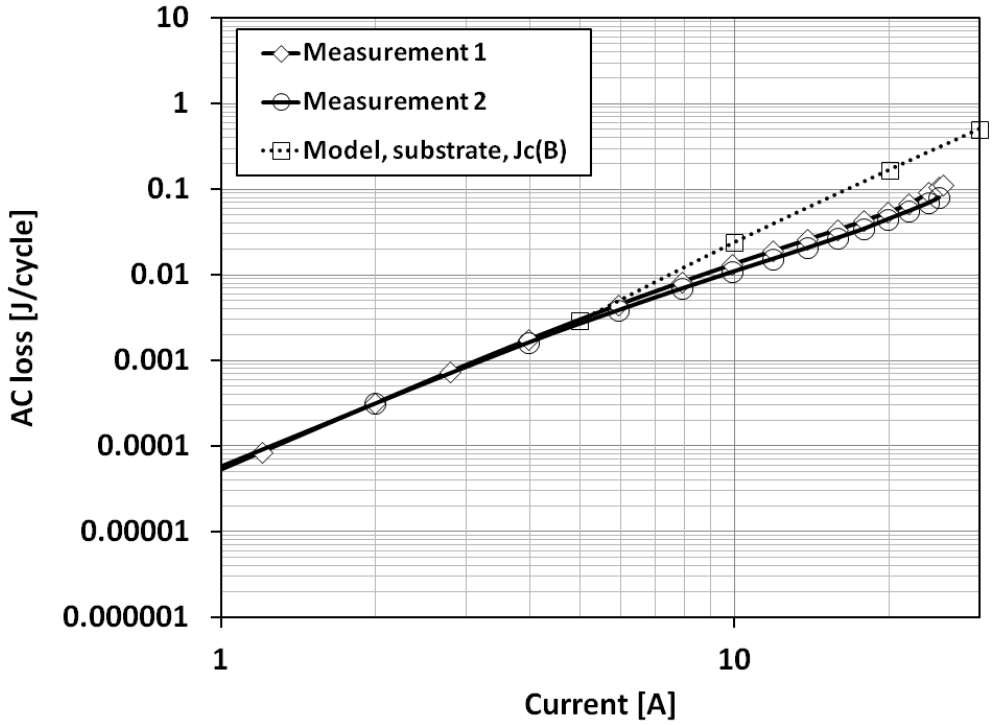

Figure 4.3: Experimental results for the transport AC loss measurement of the superconducting racetrack coil

In analytical models based on the critical state approximation, the AC loss has a cubic or quartic dependence [51,67,101]; however, for currents greater than 10 A, the measured AC loss tends towards a square law relationship, suggesting that the actual phase had drifted from the original phase setting. As the transport current increases, the AC loss voltage increases at a faster rate than the inductive voltage, which increases linearly, and this results in a phase shift from the original setting, i.e. phase drift. If the phase between the control voltage (i.e. the oscillator output

of the lock-in amplifier) and the current does not change, then one phase setting is accurate, but this is not always the case, as found here. In the following section, a method to improve the phase setting in order to obtain more accurate results over a wider range of currents is suggested.

4.3 Improved electrical method

In this section, an improved electrical method is proposed in order to overcome the phase drift observed above, and to improve other aspects of the experimental setup. To avoid phase drift, the phase needs to be adjusted each time the current is varied to ensure that it is set correctly. By using a purely resistive or inductive reference signal, this can be achieved. A different superconducting coil, which is described below, is used for these experiments as the previous racetrack coil has now been installed in the all-superconducting HTS PMSM for its electrical testing.

4.3.1 New superconducting pancake coil

The circular HTS pancake coil to be tested is shown in Figure 4.4 and was wound at the University of Oxford. The wire specification is listed in Table 4.1. The total length of wire used is 29.55 m, resulting in 81.5 layers of silk ribbon interleave, vacuum impregnated with epoxy resin. The inner diameter of the coil is 100 mm and the outer diameter is 130 mm. There are voltage taps located 150 mm from the end of each coil and at intervals of approximately 10 m within the coil. The estimated inductance of the coil is 1 mH.

Table 4.1: SuperPower SCS12050-AP wire specification

Thickness	0.097 mm
Width	12.01 mm
Average critical current at 77K, self-field	295 A
Minimum critical current at 77K, self-field	269 A

Figure 4.4: Completed circular HTS pancake coil wound with SuperPower wire

4.3.2 Experimental setup

A schematic of the new experimental setup is shown in Figure 4.5 and the main components of the setup are shown in Figure 4.6. The main components shown are a lock-in amplifier, a signal generator to provide the sinusoidal waveform input, an oscilloscope to examine signals in real time, and a power amplifier. The liquid nitrogen bath for the superconducting coil, the compensation coil and the clamp meter are shown in Figure 4.7. The superconducting coil submersed in liquid nitrogen, and its associated wiring and voltage taps, are shown in Figure 4.8.

The compensation coil is the same one used above, but a number of turns have been taken off the primary coil to reduce its total mutual inductance, as the new coil under test has an inductance approximately one third of the previous racetrack coil. The transformer has a turns ratio of 115:44 and is used to match

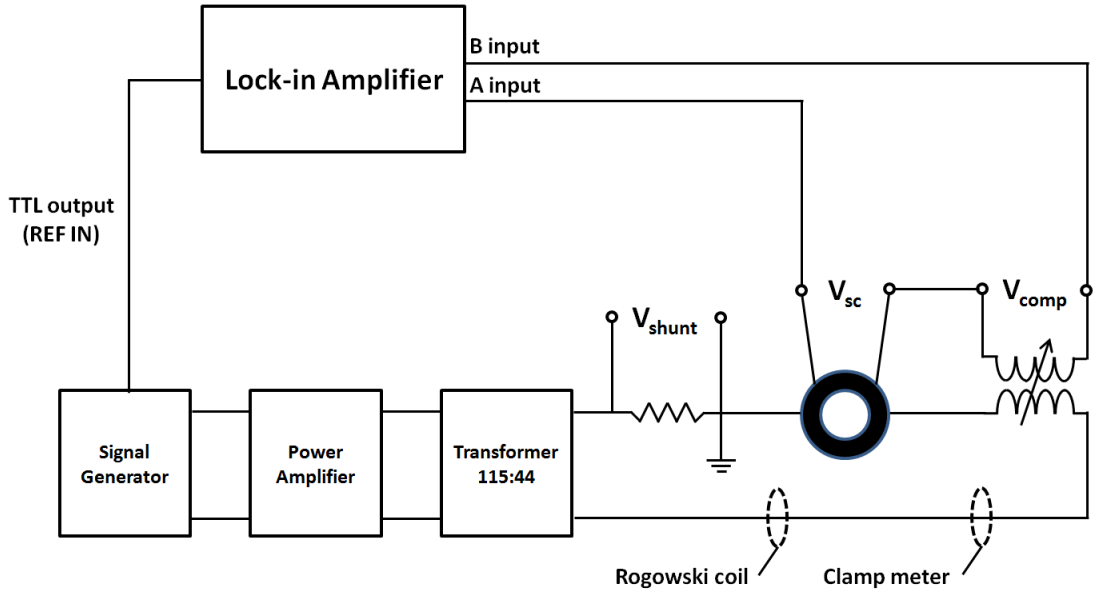

Figure 4.5: Schematic diagram of new experimental setup for measuring transport AC loss in superconducting coils electrically

the power amplifier to the load.

In order to provide a reference signal to the lock-in amplifier, a Rogowski coil is used, which is shown in Figure 4.9. This is a crucial part of the experimental setup, which provides a purely inductive signal 90° out of phase with the circuit current, but at the same frequency, that can be used to accurately set the phase of the lock-in amplifier. A resistor of known value could also be used, but since all resistors have some inductance this may pose problems when setting the phase. Additionally, a Rogowski coil is largely immune to electromagnetic noise if wound correctly with evenly spaced windings. A shunt resistor of 500 $\mu\Omega$ has been provided in the circuit as an additional reference signal (instead of the Rogowski coil), but also as an additional means to measure the current (instead of the clamp meter). Shielded twisted pair cable is used to connect the Rogowski coil to the lock-in amplifier; this type of cable is less susceptible to electrical interference from nearby equipment and wires, and the signal is less likely to cause interference itself. Shielded twisted pair cable is also used for the connection of the compensated superconducting coil voltage signal to the lock-in amplifier.

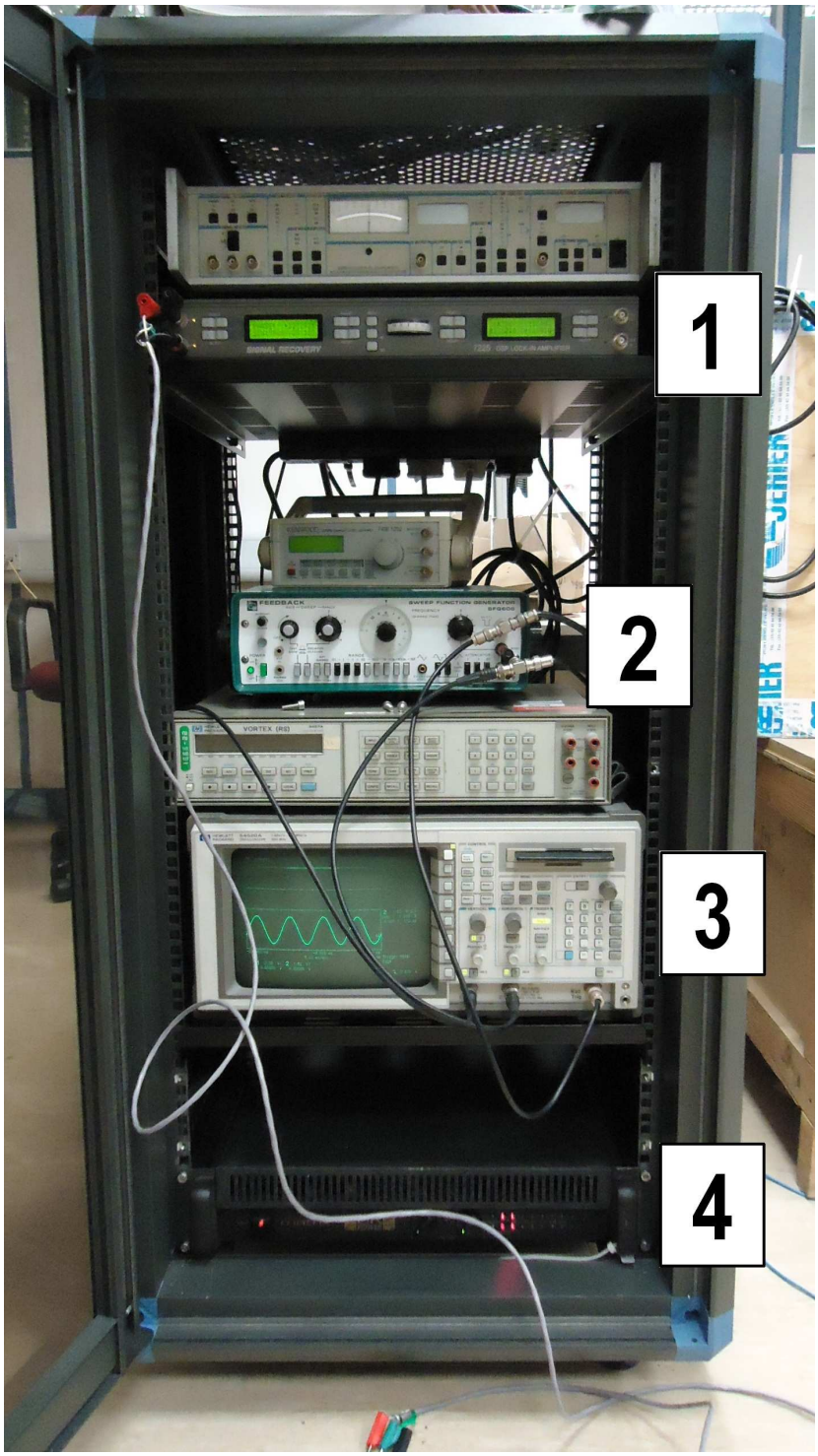

Figure 4.6: Main components of the new experimental setup for measuring transport AC loss in superconducting coils: 1) lock-in amplifier, 2) signal generator, 3) oscilloscope, and 4) power amplifier

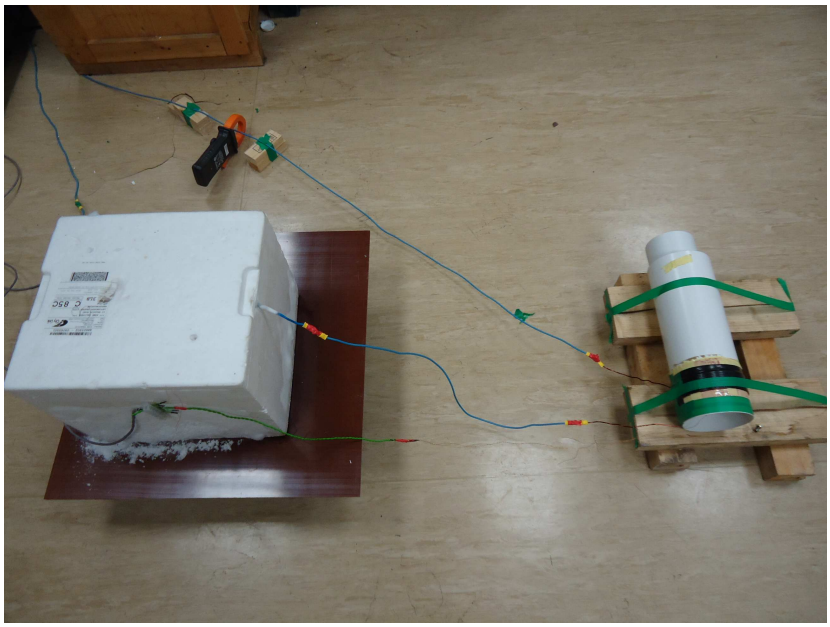

Figure 4.7: Superconducting coil liquid nitrogen bath, compensation coil and clamp meter

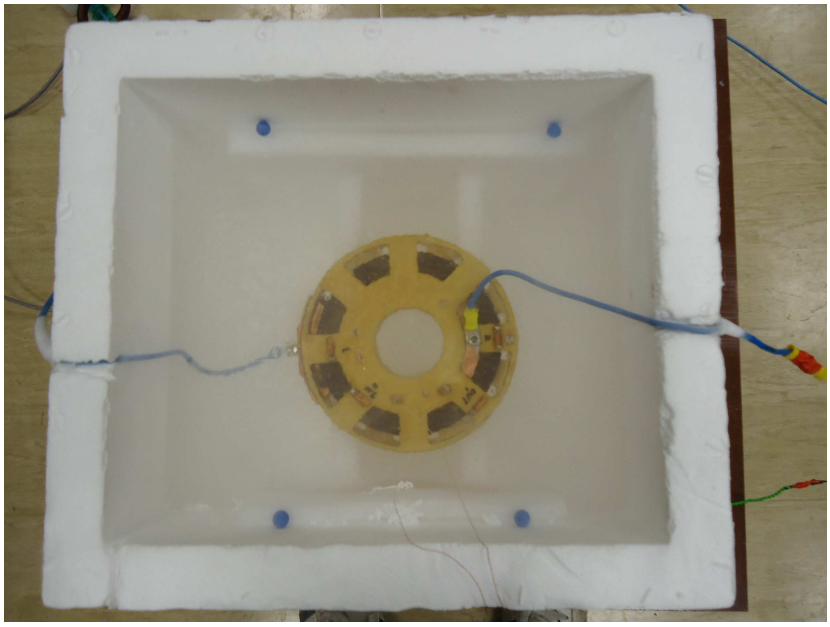

Figure 4.8: Superconducting coil submersed in liquid nitrogen, and its associated wiring and voltage taps

Instead of using the internal reference of the lock-in amplifier as done previously, the reference (TTL) output of the signal generator is used, which provides a clean 5 V square-wave reference signal to the lock-in amplifier at the same frequency as the circuit current. The phase setting of the lock-in amplifier is one of two major problems that can arise when using a lock-in amplifier to measure AC loss [102], and the use of the Rogowski coil in combination with the compensation coil and TTL reference significantly improves the accuracy of the phase setting.

Figure 4.9: Hand-wound Rogowski coil used to provide the lock-in amplifier reference signal

The other major problem that can arise is the presence of a common mode voltage v_{cm} at the lock-in amplifier input [102]. Since the operational amplifiers present at the input stage of all lock-in amplifiers are not ideal, the output of these operational amplifiers is given by

$$v_{\text{out}} = \text{A} \cdot (v_1 - v_2) + v_{\text{cm}} \cdot \text{CMRR} \tag{4.5}$$

where A is the gain of the amplifier, v_1 and v_2 are the input voltages, v_{cm} is the common mode voltage $\frac{v_1+v_2}{2}$, and CMRR is the common mode rejection ratio, a

factor that specifies the degree of cancellation of the common mode voltage [102]. The lock-in amplifier used here is the Signal Recovery Model 7225 DSP lock-in amplifier, which has a CMRR of $>$ 100 dB at 1 kHz. The common mode voltage can also be reduced by grounding the circuit near the coil and ensuring that the entire measurement circuit only has one common ground point [103]. As shown in Figure 4.5, the circuit is grounded between the superconducting coil and shunt resistor; the ground wire is connected via a 1 kΩ resistor to the lock-in amplifier chassis, the transformer aluminium housing and the outside of the transformer. The use of the differential input (A-B) of the lock-in amplifier provides a balanced input, and combined with the use of the GND/AC setting, which connects the input terminals to chassis ground, avoids the problem of 'hidden,' multiple grounds that can arise with some lock-in amplifiers [103]. This setting also makes the signal channel input AC coupled.

Another important setting for the lock-in amplifier is the type of input device. For this, the 'FET' device is selected. The FET device provides the largest input impedance possible (10 MΩ), whereas the other option (Bipolar) provides only 10 kΩ. When the Bipolar setting is used, the lower input impedance can draw some current from the signal source, which affects the phase of the measured signal. For example, the secondary coil of the compensation coil has a relatively high impedance (much greater than the superconducting coil and approximately 230 Ω), and using the Bipolar setting a small in-phase component is measured, whereas using the FET setting, a purely inductive voltage is measured. The combined use of the FET setting and twisted pair cable of small wire diameter for the secondary coil satisfies the requirements of low phase shift and low noise for the compensation coil.

A dummy load, a 0.5 Ω resistive load that has a similar impedance to the superconducting coil at 50 Hz, is used to test the phase setting by comparing the $\frac{V^2}{R}$ loss using the voltage measured by the lock-in amplifier across a small (500 $\mu\Omega$) shunt resistor connected in series with the dummy load and the I^2R loss using the current measured by a clamp meter. It was found that these results are consistent, as shown in Figure 4.10, implying that the phase was correctly set when using both the Rogowski coil and shunt resistor signals as the reference. The dummy load was also used to test the maximum voltage/current provided

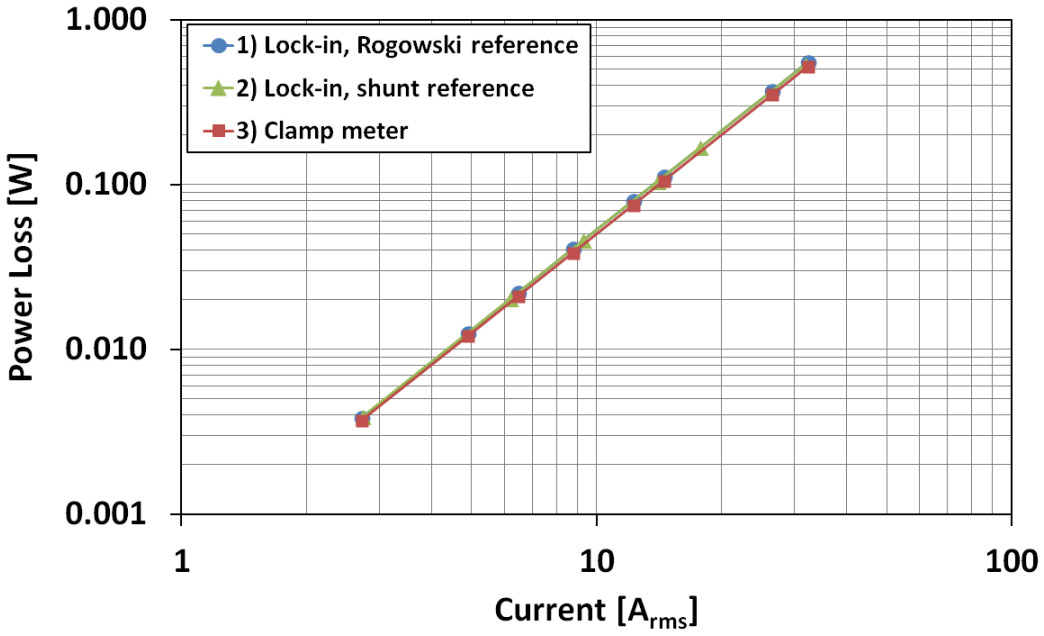

Figure 4.10: Power loss measurement of 500 $\mu\Omega$ shunt resistor using two different methods (lock-in amplifier and clamp meter) and setting the lock-in amplifier phase using the Rogowski coil and shunt resistor

by the setup, which was found to be 30 V/60 A.

The steps involved in the measurement are as follows.

1. Connect the Rogowski coil signal to inputs A and B of the lock-in amplifier, which is set to differential (A-B) mode

2. Measure the voltage across the Rogowski coil and set the phase of the lock-in amplifier to the measured phase $\pm$ 90° (since the Rogowski is 90° out of phase with the circuit current)

3. Connect the compensated* superconducting coil voltage to inputs A and B of the lock-in amplifier

4. If the phase is set correctly, the reading 'X' on the lock-in amplifier is the AC loss voltage

5. Increase the current, and repeat steps 1-4 for each measurement point

* Compensation is carried out by measuring the combined superconducting coil and compensation coil voltage when applying a small current to the coil after setting the phase with the Rogowski coil and minimising the inductive component ('Y' reading) on the lock-in amplifier by adjusting the compensation coil. If the phase is set correctly, adjusting the compensation coil will change the 'Y' reading, but not affect the 'X' reading, i.e. in-phase, 'resistive' component. If the 'X' reading does change, the phase is incorrect and must be set again.

4.3.3 Experimental results

Figure 4.11 shows the experimental results for the transport AC loss measurement for four frequencies (39.93, 80.83, 120.1 and 158.2 Hz) indicated by the transparent symbols, as well as the calculated transport AC loss using a constant J_c (dashed blue line) and $J_c(B)$ (red line). Included in the figure are additional measurements taken at 80.5 Hz with the coil raised from the floor and the compensation coil located further from the coil, which will be discussed later in this section.

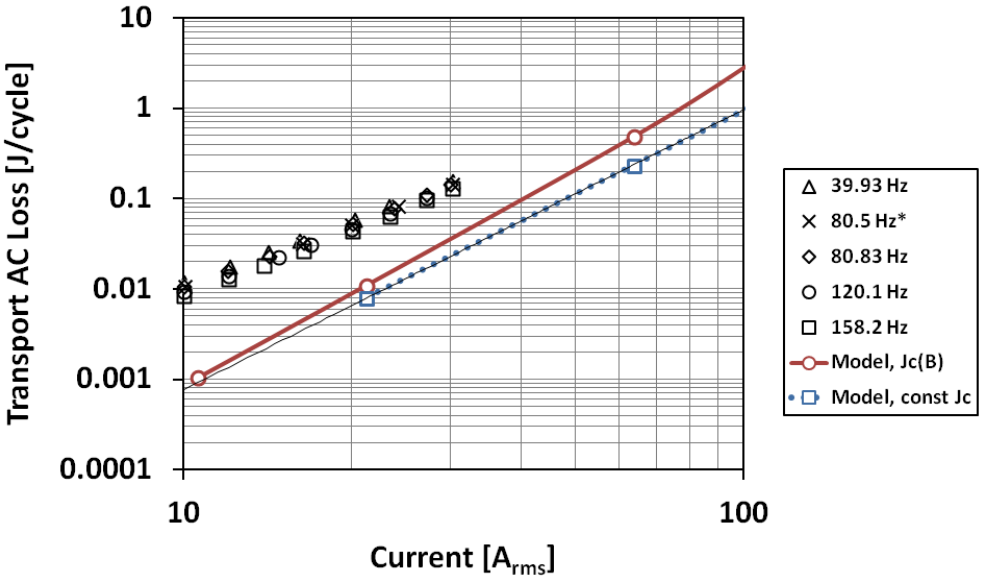

Figure 4.11: Calculated transport AC loss using a constant J_c and $J_c(B)$ and experimental results for four frequencies (39.93, 80.83, 120.1 and 158.2 Hz)

The transport AC loss in J/cycle for each of the frequencies measured is fairly consistent, which is expected for a hysteretic loss. The losses obey an almost cubic law, which is also expected, as described earlier in this chapter. However, the magnitude of the loss is about an order of magnitude higher than predicted by modelling for the coil at low current (10 A), and tends towards the modelled loss for increasing current. The reasons for the discrepancy between the measured results and the model are outlined in the following discussion.

Although the model can account for a reduction in J_c due to magnetic field, which is discussed below, it does not account for a number of other factors, such as any reduction due to bending strain on the tapes, mechanical stresses during the winding process or thermal stresses when the coil is cooled. In regards to the first two factors, if the coil winding process applies higher tension levels than those used by the manufacturer, there is potential to induce mechanical defects in the wire, which will result in a degraded J_c. In regards to the third factor, Siemens recently presented [104] results on coil winding techniques for coils wound with 2G HTS wire. A number of racetrack coils were wound using both American Superconductor and Superpower wire, and it was found that most of the coils had a critical current I_c much lower than the wire I_c, except for a couple of coils. The I_c for some coils degraded with subsequent repeated measurements of the I-V curve, which has been reported elsewhere [99, 105], and the worst coils degraded with each thermal cycle, i.e. each time the coil was cooled down. The likely cause of this degradation was suggested to be how the inner tape is bonded to the former, as when the coil is cooled down, the coil former shrinks more than the tape, which increases the radial tensile stress on the tape and can cause tape delamination. In [105], the authors present evidence for this in the form of images of the microstructure of a fractured surface taken by a scanning electron microscope (SEM).

The solder joint between the superconductor and the current lead contacts (and solder joints between tape lengths in larger coils) has also been identified as a cause of J_c degradation [106]. The model assumes a perfect current connection between the current leads and the superconductor, and heat propagating from the current contacts could reduce J_c locally, without quenching the entire coil, which would cause a transition to the normal state and dramatically increase the

measured loss.

There may also exist localised heat spots within the coil where heat cannot dissipate well. In regards to these potential 'hot spots,' a visual inspection of the coil in the liquid nitrogen bath while current is applied showed a fairly uniform boil-off around the coil, except at the current contacts where there is a large amount of boil-off. There was no conclusive evidence that any particular section of the coil was weak, resulting in a larger localised boil-off. Research into coil winding techniques, including types of and ways to make current contacts, types of coil impregnation, and current leads to connect to a superconducting coil, continues to be carried out by a number of research groups worldwide.

The model therefore represents the best case scenario and assumes a perfectly wound coil, which is currently quite difficult to achieve in practice. Non-uniformities in J_c within the coil can alter the power exponent of the AC loss curve, which has been found for single tapes [107] and for tape-wound coils [108]. In [107], the authors investigate the transport AC loss in a single tape versus Norris's strip model and find that deviation of this loss from Norris's model is mainly caused by degradation of the critical current distribution, particularly at the edges, which results in significant deviation between the experimental results and the model for currents much less than the I_c of the tape. The 30 m spool of Superpower tape used to wind the coil has some variation in I_c from the manufacturing process, as shown in Figure 4.12, varying between approximately 270 A and 310 A for 5 m sections of tape. The n value of the tape also varies from about 22 to 27 between these sections. Although it is possible to achieve good agreement between AC loss measurements and FEM simulations for single tapes and small stacks of tapes [109] without any adjustable parameters, i.e. using only the I_c and n values as inputs, this may not be possible with a coil. It is possible to include in the model J_c values for certain sections of tape that relate to the inhomogeneity of critical current in certain sections or sections with degraded J_c, if these are known.

As observed in the modelling chapter, and as shown in Figures 4.3 and 4.11, the approximation used for J_c can have a large effect on the magnitude of the calculated AC loss, as well as the power exponent of the AC loss curve, particularly when comparing the constant J_c approximation with $J_c(B)$. The constant J_c

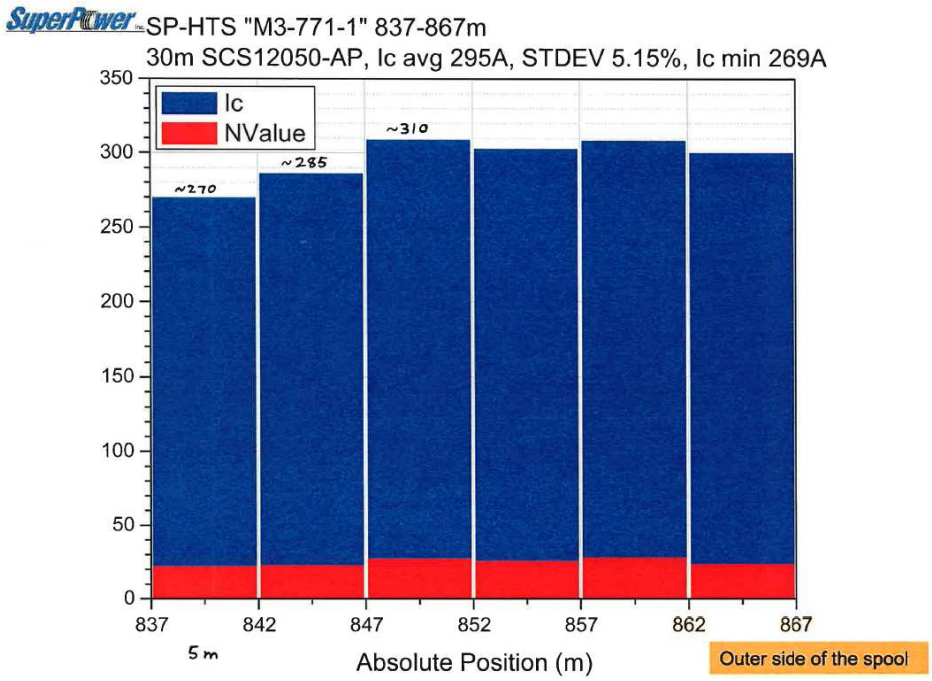

Figure 4.12: Superpower measured data for critical current I_c and n value for 5 m sections of tape for the 30 m spool of tape used to wind the superconducting coil

approximation assumes no magnetic field dependence and has the lowest power exponent, and using a B-dependent J_c results in an increasing power exponent. The $J_c(B)$ used in the model is taken from manufacturer data for a representative tape, but not for the actual tape in the spool used to wind the coil. For improved accuracy for $J_c(B)$, a short sample of tape from the spool could be measured in different magnetic fields (and even for different angles of applied magnetic field) at 77 K before winding. Due to the dynamics of the flux penetration, i.e. mainly along the x axis, the component of loss due to the perpendicular field B_y should be much higher than any effect from B_x, but this may not be true for all coil geometries.

Although the power amplifier was able to provide up to 60 A to the resistive dummy load, it was found that the amplifier did not perform well when the load was changed to the superconducting coil, most likely due to the inductive nature of this load and its poor power factor. The dummy load was added in series with

the superconducting coil, which provided a load with a much better power factor, but this increased the overall impedance of the load, given by

$$Z = 0.5 + j\omega L = 0.5 + j2\pi fL \ [\Omega] \tag{4.6}$$

where f is the frequency of supply and L is the inductance of the coil. The inductance of the coil was measured to be 1.04 mH (cf. estimated value of 1 mH). This increased load impedance meant that the circuit could supply up to only approximately 30 A. However, without knowledge of the I_c of the coil, the percentage of coil I_c that this maximum value of current supplied corresponds to cannot be determined. In both [107] and [110], it was found that the measurement results converged on the modelling results for current close to I_c, but deviated somewhat for current much less than I_c. According to the model, the I_c of the coil should be around 233 A, which was calculated using the model used in the comparison in Figure 4.11, based on complete penetration of the perpendicular magnetic field to the centre of any tape in the stack. This model uses the $J_c(B)$ relationship described previously and assumes that all tapes have an I_c of 300 A. An I_c measurement of the coil will provide information on the overall J_c of the coil, and measurement of the voltage across the voltage taps will provide detailed information on the sections where J_c may be degraded the most. This will be presented later in this section.

4.3.3.1 Voltage tap measurements

These voltage taps were utilised in the transport AC loss measurement to measure the loss in certain sections of the coil. Figure 4.13 shows a comparison of the measured transport AC loss of the entire coil and each voltage tap for f = 80.9 Hz with the modelling results for sections corresponding to the voltage taps. v_1 corresponds to the voltage tap on the outermost turn, v_2 and v_3 correspond to voltage taps located at positions 10 m and 20 m from the outermost turn, respectively, and v_4 corresponds to the voltage tap on the innermost turn. The measured results indicate that the largest loss occurs between the innermost voltage taps $(v_3 - v_4)$ and the smallest loss occurs between the outermost voltage taps $(v_1 - v_2)$. The modelling results indicate that the largest loss is expected between

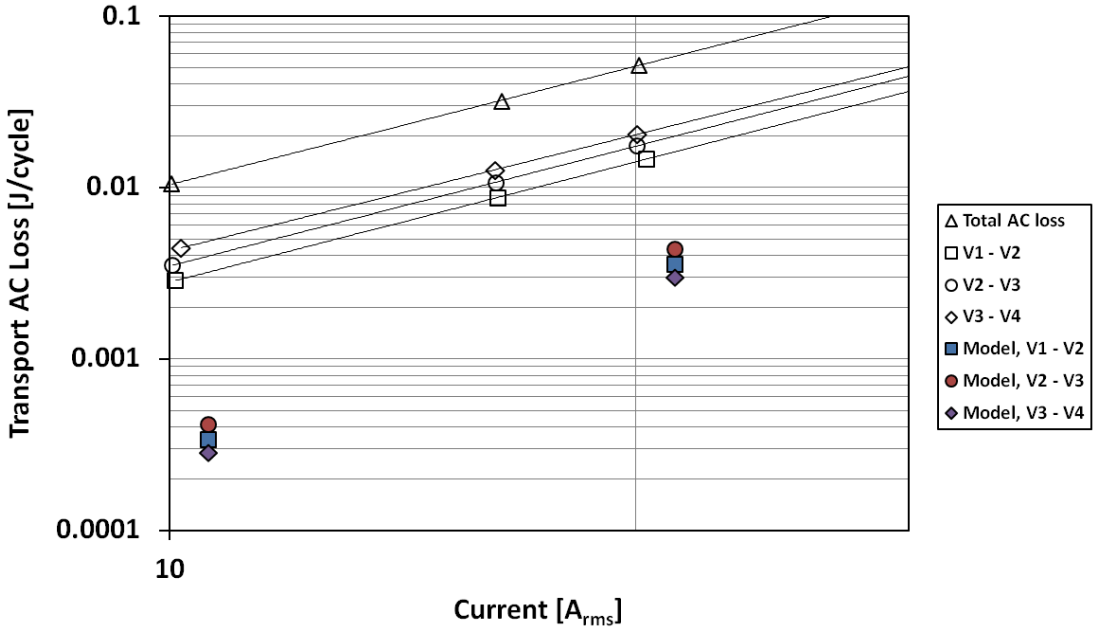

Figure 4.13: Comparison of measured transport AC loss of entire coil and each voltage tap for f = 80.9 Hz with modelling results for sections corresponding to the voltage taps

the middle voltage taps ($v_2 - v_3$) and the smallest between the innermost voltage tapes ($v_1 - v_2$). Therefore, the major difference between the experimental and modelling results is a larger loss measured for the innermost voltage tap, which may correspond to the problem described above in relation to stress on the inner turn and perhaps the joint between the inner turn and the current contact.

4.3.3.2 Coil critical current measurement

In order to account for degradation of the tape J_c within the coil in the model to accurately estimate the AC loss, the critical current measurement should be performed first. However, there is a risk of quenching the coil with this type of measurement and irreversible damage to the coil can occur. The waveform of the applied current for this measurement is shown in Figure 4.14, where I_{step} is the magnitude of the step change in current and t_s is the settling time between each step change. Figure 4.15 shows the first set of critical current measurements

for I_{step} = 1 A. Measurements 1 and 2 were carried out with t_s = 1 s, and measurements 3 and 4 were carried out with t_s = 2 s. Using the voltage criterion of 1 μV/cm and the length of tape used to wind the coil l $\approx$ 30 m, the voltage across the coil when carrying its critical current is defined as 30 mV, which corresponds to approximately 60 A in Figure 4.15. This is significantly less than the predicted critical current (233 A) based on the model above, which uses the original critical current of the tape, assuming no degradation. The curve continues to increase until approximately 100 A, where there is a large increase in voltage due to thermal runaway, which is more prevalent when t_s = 2 s, as there is more heat generated for each step in this case. It should also be noted that the critical current did not degrade with each measurement.

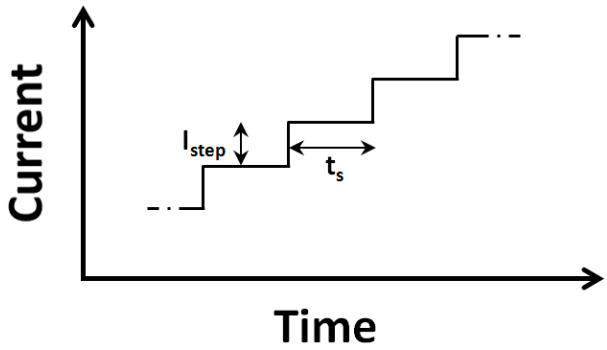

Figure 4.14: Waveform of applied current for coil critical current measurement

These results indicate that the J_c of the tape has degraded during the winding and/or cooling process, and the coil critical current data can be utilised in the model to more accurately calculate the AC loss. Since the critical current of the coil is approximately 60 A, an average critical current for the tape can be estimated as 100 A, taking into account that the critical current of the coil is reduced in comparison to the tape due to the larger coil self-field and the B-dependent J_c (cf. the coil critical current is approximately 233 A using a tape critical current of 300 A). A comparison of the calculated transport AC loss using this modified J_c to account for degradation of the superconducting tape and the experimental results presented earlier is shown in Figure 4.16. The model shows good agreement with the experimental results when the model is modified to

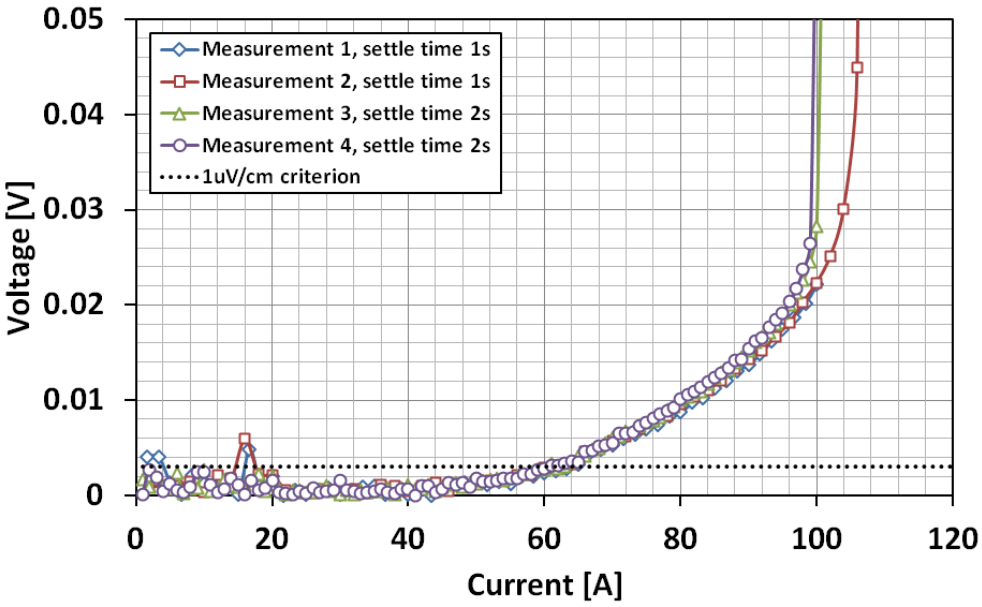

Figure 4.15: Coil critical current measurement

account for J_c degradation. It should be noted here that the coefficient relating to the B-dependence of J_c has not been modified here, which has an effect on the power exponent of the AC loss curve. Since the J_c of the tape has degraded significantly, it is not unreasonable to expect that this coefficient has also changed, but this would be difficult to measure for the wound coil.

In order to assess which area (or areas) of the coil has degraded, the voltage taps were then utilised, but a large quench of the coil occurred during the first measurement. The critical current of the coil was re-measured, and the results are shown in Figure 4.17. Some damage to the coil occurred during the quench, which resulted in the critical current reducing to approximately 30 A. The voltage across each of the voltage taps was then measured in order to deduce where the damage occurred and where the weakest part of the coil is located. Figure 4.18 shows the voltage measured across each set of voltage taps: the outermost taps $(v_1 - v_2)$, middle taps $(v_2 - v_3)$, and the innermost taps $(v_3 - v_4)$. A large voltage is observed across the innermost taps, present even at even low current, suggesting the damage occurred in the area closest to the inner turn. The voltage across the other taps remains low, although the voltage between the middle taps does

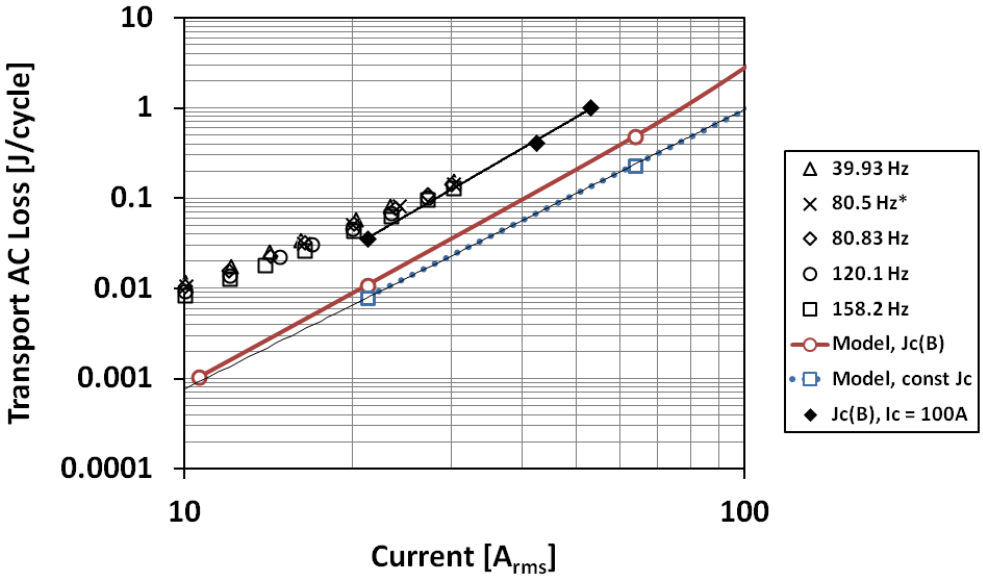

Figure 4.16: Comparison of calculated transport AC loss using a modified J_c to account for degradation of the superconducting tape and experimental results

increase more as the current is increased past approximately 60 A. This suggests the weakest part of the coil is closest to the inner turn, providing evidence for the argument above. This result is consistent with the AC loss measured across the voltage taps shown in Figure 4.13. One last coil critical current measurement was carried out after measuring the voltage taps, and no further degradation of the coil was observed.

4.3.3.3 Possible sources of measurement error

Although as much care as possible was taken in regards to sources of measurement error, there may be small sources of loss within the experimental environment that could contribute to the losses measured. These losses can be attributed to magnetic losses (proportional to frequency) and eddy current losses (proportional to frequency-squared). The measured voltage signals increase in proportion to frequency, which results in the consistent J/cycle loss for different frequencies shown in Figure 4.11. Both magnetic losses and the hysteretic loss in the superconducting coil are proportional to frequency, so it is hard to determine from the voltage

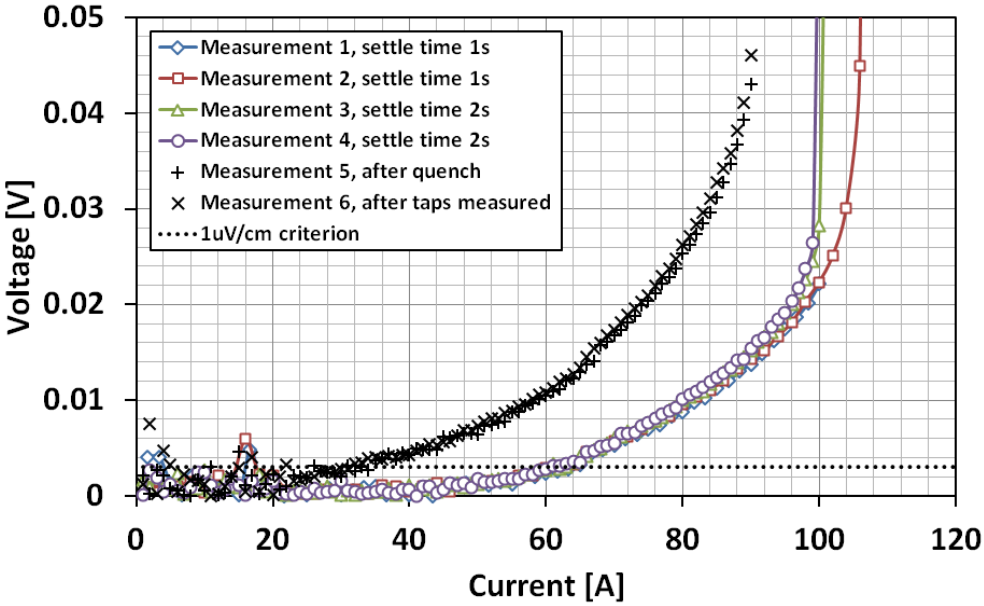

Figure 4.17: Coil critical current measurement after large quench

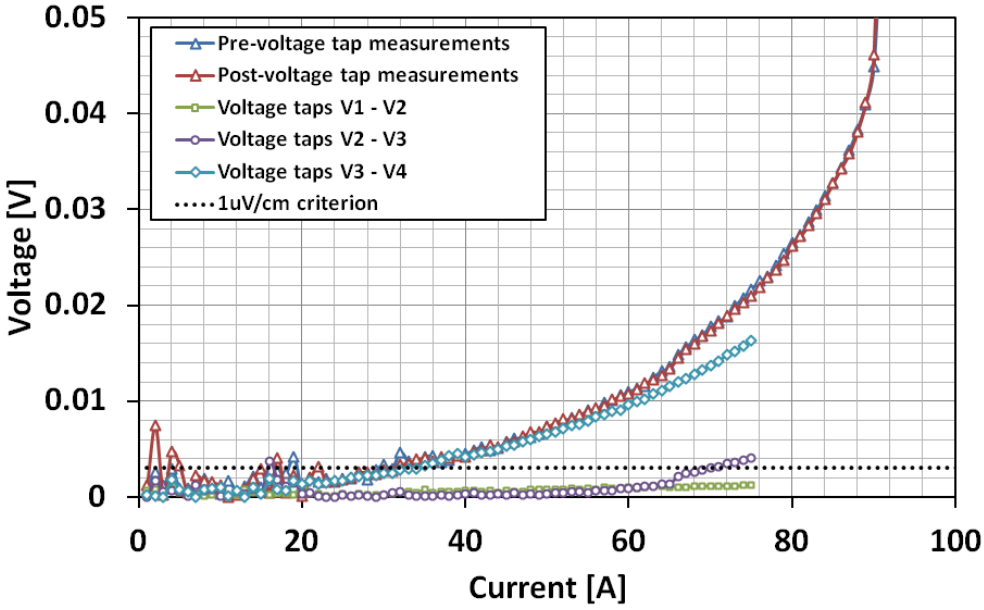

Figure 4.18: Voltage taps measurement after large quench

signal whether there is a significant magnetic loss present. However, measures were taken to ensure that any magnetic or conductive materials (for example, the transformer, which has a large magnetic core, and the power amplifier, which has a magnetic toroidal transformer inside) were located at a significant distance away from the superconducting coil and compensation coil. A concern was raised that if there is magnetic material present in the floor of the room housing the experiment (for example, steel reinforcement), then this can affect the measurement, since the coil is close to the floor. In order to check this potential problem, the liquid nitrogen bath was raised 17 cm from the floor using a plastic box, and measurements were carried out at f = 80.5 Hz. This measurement was consistent with the previous measurements, satisfying this concern.

4.3.4 Suggested future improvements

In order to improve measurements in the future, the following should be considered.

- Two compensation coils

  It is difficult to achieve exact compensation of the inductive voltage using the large compensation coil used in these experiments. An additional, smaller compensation coil could be introduced to provide fine-tuning of the compensation. Although exact compensation is not necessary, it would improve the accuracy of the measurement, since the measurement error of the in-phase voltage depends strongly on the inductive and resistive voltage component ratio of the sample [102]. More accurate compensation increases the tolerance of any phase error that may exist in the measurement of the reference phase. For example, if the inductive voltage is two orders of magnitude higher than the resistive voltage for an uncompensated sample, then a phase error of 0.1° will result in 0.1745% of the inductive voltage being added to the resistive voltage [102]. Figure 4.19 shows the calculated relative in-phase (resistive) voltage error as a function of the ratio between the inductive and resistive voltage components for phase errors of 0.05, 0.1 and 0.5°.

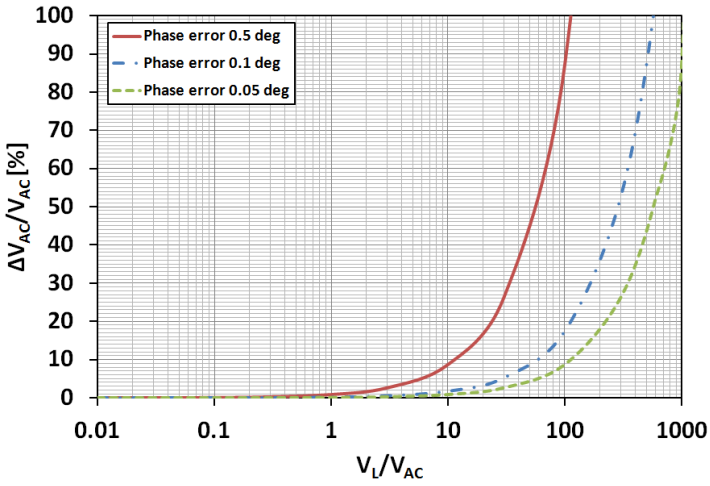

Figure 4.19: Relative in-phase (resistive) voltage error as a function of the ratio between the inductive and resistive voltage components of the measured signal for different phase errors

- Two lock-in amplifiers

  The existing setup requires that the phase setting be performed first using the Rogowski coil, then the AC loss measured. By using two lock-in amplifiers - one to set the phase and one to measure the loss - the swapping of the Rogowski coil signal and the compensated superconducting coil signal wires, which is currently required for each measurement point, could be avoided.

- Isolated experimental environment

  As described above, the measurement can be sensitive to nearby conducting and magnetic materials, and carrying out the experiments in an isolated room free of these materials, other than those necessary for the experimental setup itself, would improve the accuracy of the setup. A larger room, where the superconducting coil and compensation coil can be isolated at a large distance from other equipment, would also be recommended.

In the following chapter, an investigation on a method to reduce transport AC losses in superconducting coils is carried out, using magnetic materials as a flux diverter.

Chapter 5

AC loss mitigation

In this chapter, methods used to mitigate AC loss in superconducting wires and coils are summarised, and the use of weak and strong magnetic materials as a flux diverter is investigated as a technique to reduce AC loss in superconducting coils that does not require modification to the conductor itself, which can be detrimental to the superconductor's properties.

5.1 AC loss mitigation techniques

As seen in previous chapters, the AC loss of a superconducting coil is significantly large, and this will reduce the efficiency of the device in which it is utilised, particularly when the loss is reflected back to room temperature by including the refrigeration cost. In order to improve the efficiency of practical superconducting devices, the AC loss needs to be reduced, and a number of groups have been involved in research on possible AC loss mitigation methods. There exist methods to reduce AC loss through improved material manufacturing techniques, which can improve pinning, grain structure/boundaries, and so on, but this is the domain of materials scientists. Here the discussion is limited to existing methods to reduce AC loss of already manufactured, i.e. 'off-the-shelf', HTS conductors, and these methods are summarised below.

5.1.1 Striation into narrow filaments

This method involves the HTS conductor being striated into narrow filaments, which reduces the hysteretic loss, since hysteretic loss is proportional to the width of the tape [111–113]. The conductor can be striated using a slitter machine [114], which cuts the conductor into separate filaments, or with laser ablation [115, 116], photolithography or wet etching [111]. An example of tape striation using laser ablation is shown in Figure 5.1. However, striated tapes are vulnerable to localised defects [116], which can impede the flow of current through a filament, so uniformity of the properties of individual filaments is extremely important [117]. This problem can be overcome either by covering the filaments with a thick normal metal layer of low resistivity or by making a network of superconducting bridges, in such a way that allows current sharing between filaments [116]. For mechanical cutting, degradation of J_c can occur at the edges of the filaments and can depend on the cutting process used [114]. However, the original tape itself may suffer from non-uniformities, from which the striated tape is prepared [117]. Whilst striation reduces the hysteretic loss in comparison with a single tape, it introduces a new loss in the form of a coupling loss due to the coupling of separate filaments [116, 118] and this loss can be significantly more than the self-field loss for an uncoupled tape carrying the same current [119]. Research continues in this area [120–123].

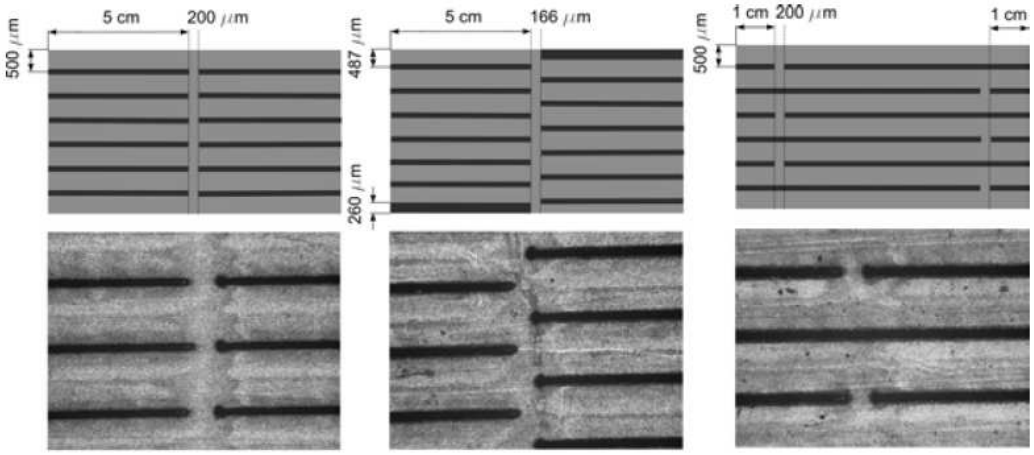

Figure 5.1: Striation of HTS coated conductor using laser ablation [116]

5.1.2 Roebel transposition

The concept of Roebel transposition was first introduced by Ludwig Roebel in 1914 in his patent application to reduce AC losses in copper cables for generators, and the design is particularly suitable for AC windings [124]. In relation to superconducting wires, the Roebel concept has been applied already to NbTi cables [125] for use in the International Energy Agency (IEA) Large Coil Task (LCT), which was an international collaboration between the United States, EURATOM, Japan, and Switzerland to develop large superconducting magnets for fusion reactors [126], and to BSCCO-2223 for use in a transformer [127]. Recent research has seen the application of the Roebel concept to YBCO coated conductors; for example, [124, 128, 129]. The YBCO conductor must be cut or punched into shape before winding, and an example of cut/punched filaments and an assembled cable is shown in Figure 5.2. Various groups have shown promising results, such as measurement of reduced AC loss [129] and accurate prediction of a cable's critical current from the $J_c(B)$ dependence of a single tape [44], and research continues in this area [130–136].

5.1.3 Twisted wires

The large current that can be carried by a superconductor generates a large self-field, and in the past superconducting wires have been twisted to avoid flux linkage between the filaments. Ideally the wires would be fully transposed, where each wire swaps places with every other wire along the length, so that averaged over the length, no net mutual flux linkage occurs [137]. Many studies have been carried out on the AC loss of twisted multifilamentary superconductors, most extensively for low temperature superconductors (NbTi and Nb_3Sn, for example) in [138–140], but also for 1G HTS (BSCCO) in [141–143] and for MgB_2 in [144–146]. Indeed, one particular type of twisted multifilamentary superconductor configuration - the Rutherford cable - has been highly successful, and has been used in all particle accelerators to date [137]. However, twisting the filaments severely will damage the microstructure, the evolution of texture, and eventually decrease the critical current [141]. Due to the nature of the geometry of the high temperature superconductors, having a large aspect ratio, the damage

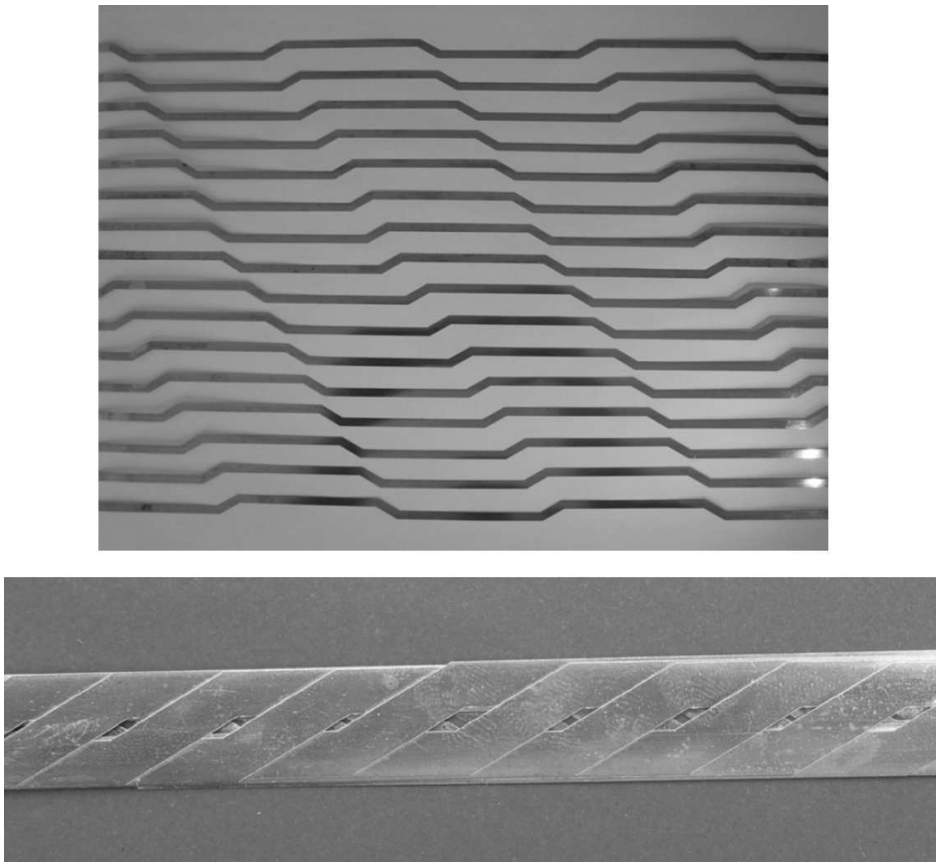

Figure 5.2: Punched strands from SuperPower-manufactured YBCO coated conductor (top) and an assembled YBCO Roebel cable (bottom) [124]

can be even greater than with other superconductors. A conceptual approach to the "ultimate low AC loss YBCO superconductor" is presented in [147], where a fully transposed YBCO tape approximating a Rutherford cable has been conceived. When compared with the AC coupling loss in a flat twisted tape, the loss can be reduced by as much as a factor of 20 [147]. However, since the Rutherford configuration requires a tape edge turnaround for the YBCO current path, a more elaborate analysis is required of the YBCO material in these locations, as there will most likely be disrupted grain orientations [147], which would significantly affect the current path and the critical current density. The current path turnarounds on both tape edges will see a significantly reduced J_c due to YBCO J_c limits on the c-axis [147].

5.1.4 Magnetic shielding/flux diverter

Magnetic materials can be used to manipulate the magnetic flux in a superconductor to reduce the AC loss, and different terms have been used in the literature for this: *magnetic shielding/screening* [119, 148, 149] and *(magnetic) flux diverter* [43, 150, 151].

In [148, 149], a magnetic cover is used for individual filaments in a striated YBCO conductor in an attempt to decouple the filaments and reduce losses. The former reference refers to filaments that are totally enclosed by the magnetic material, and the latter refers to filling only the slits between the filaments with a magnetic material. Both configurations result in a similar reduction in AC loss; however, the latter is much more practical.

In [119], a magnetic cover is used around BSCCO-2223 multifilimentary tapes, and it was found that this can actually increase the AC loss in a single tape, but that it can be an effective screening material to decouple multiple tapes. An iron sheath around a BSCCO-2223 tape in [152] also resulted in a significant increase in AC loss (three orders of magnitude), but in addition an increase in the critical current density was reported. However, in [150], a magnetic material (nickel) is used in a C-shape to cover only the edges of BSCCO-2223 tapes, in contrast to the covers [119, 152], which covered the entire outside of the tape. This resulted in a substantial reduction in AC loss, indicating that a number of factors, such as the shape and location of the magnetic material, plays a role in whether there is an increase or decrease in loss. The work in [150] was extended to YBCO coated conductors in [43], where a horse-shoe cover of ferromagnetic material is applied to the edges of the conductor. It is observed that the loss in the superconductor is significantly less than the Norris strip model, but the additional loss incurred in the cover must be taken into account, which can be higher than the superconductor loss itself. The authors also mention that the material used (nickel) is far from a low loss ferromagnetic material, stressing the importance of material selection. In [153], the authors find that an AC loss reduction can also be achieved using ferromagnetic covers on the edges of multiple superconducting tapes in a stack. Ferromagnetic diverters have also been investigated for their application in power transmission cables to improve the magnetic flux distribution

for a given cable geometry [154] and in a synchronous generator [155]. There is a minimal number of studies on the effect of flux diverters on AC loss in superconducting coils, but one particular study on the use of a flux diverter in a YBCO-based superconducting coil has shown a reduction in AC loss without any change in the critical current [151], which is a promising result for this technique.

5.2 Flux diverter analysis

The first three techniques, and some magnetic shielding techniques, involve modification of the HTS conductor itself. If these modifications are not carried out precisely, significant degradation of the conductor properties can occur. The use of external flux diverters modifies the magnetic flux profile of the conductor(s) in order to achieve a reduction in AC loss without modifying the original conductor. Hence, the conductor can be used 'as is' (off the shelf). In this section, a study of the use of flux diverters to reduce AC loss is carried out for stacks of tapes with and without a (weak) magnetic substrate. Extending this kind of numerical modelling in the future, it will be possible to find an optimal geometry and location for the diverter to achieve the greatest reduction in loss, and different magnetic materials can be used to deduce their effect on the loss of the coil.

5.2.1 Modelling results

Figure 5.3 shows a comparison of the reduction in AC loss using a flux diverter using weak and strong magnetic materials of thickness 0.5 mm and 1 mm for stacks of tapes with and without a magnetic substrate. The flux diverter is placed along the right-hand edge of the stack of tapes, and by symmetry, would be present on the opposite side. The loss is given as a percentage of the original loss calculated for the models with no flux diverter present. It is apparent that the use of a flux diverter achieves a reduction in the AC loss of a stack of tapes, which is particularly pronounced for smaller stacks. The greatest AC loss reduction occurs when the thicker (1 mm), strong magnetic material is used, and this will be discussed in the following section. There is a pronounced decrease in the AC loss for stacks of tapes with a magnetic substrate, which is a promising result

as it was shown previously that the presence of a magnetic substrate in the superconducting tape causes an increase in AC loss.

5.2.2 Discussion

Figure 5.4 shows a comparison of the magnetic field density profiles, including magnetic flux lines, for a 50 tape stack (without a magnetic substrate) with and without a flux diverter (weak magnetic material). The same scale is used for both figures, ranging from 0 T (dark blue) to 0.567 T (red), and the density of magnetic flux lines is the same. By comparing the magnetic flux lines between the two, it can be observed that the flux diverter attracts magnetic flux towards it and changes the distribution of the field lines, which are densely packed within the magnetic material. Figure 5.5 shows the difference in the penetration of the perpendicular component of the magnetic field into the stack with and without a flux diverter for a 50 tape stack, for tapes at the 1/5 point (top) and centre (bottom).

For the flux diverter to work well, it must be within the saturation limit of the magnetic material used. When the magnetic material is saturated, any increase in the external magnetising field H, i.e. the field from the stack of tapes, cannot increase the magnetisation of material any further, so the total magnetic flux density B levels off. Hence, it ceases to act as a diverter of flux. Figures 5.6 and 5.7 show comparisons of the peak diverter magnetic flux density for diverters of weak and strong magnetic materials, respectively, for thicknesses of 0.5 mm and 1 mm for stack of 10 to 100 tapes with and without a weak magnetic substrate. The thick dashed line indicates the saturation magnetic flux density of the material. It is clear that the weak magnetic material is unsuitable as a flux diverter as for all cases the magnetic flux density exceeds the material's saturation limit. This also explains why the weak diverter performs worse than the strong diverter in respect to reducing AC loss; the strong magnetic material saturates for the 50 and 100 tape stacks, but the higher saturation limit reduces the AC loss in comparison to the weak magnetic material. Therefore, the ideal flux diverter material will have a high saturation field, as well as a low remanent field, which reduces the size of its hysteresis loop, resulting in lower loss in the material for each AC cycle.

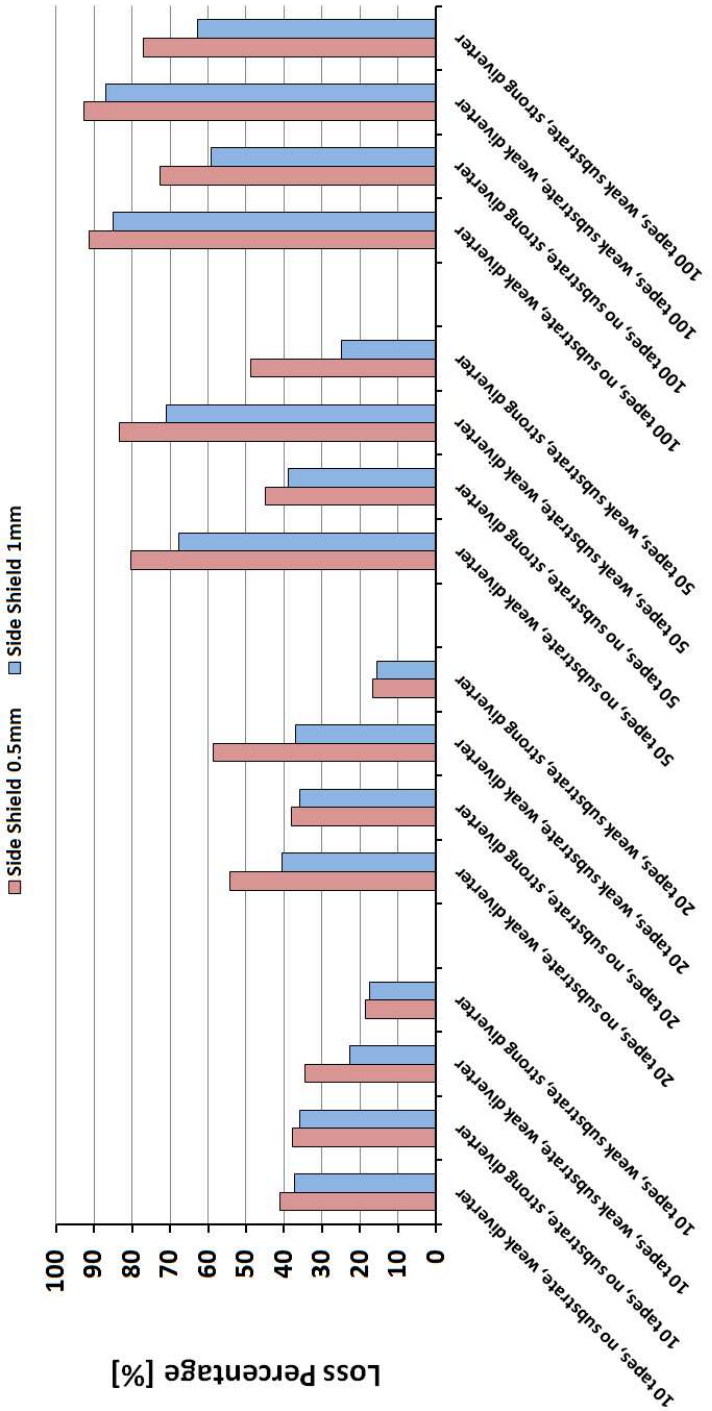

Figure 5.3: AC loss reduction using flux diverter using weak and strong magnetic materials of thickness 0.5 mm and 1 mm for stacks of tapes with and without a weak magnetic substrate

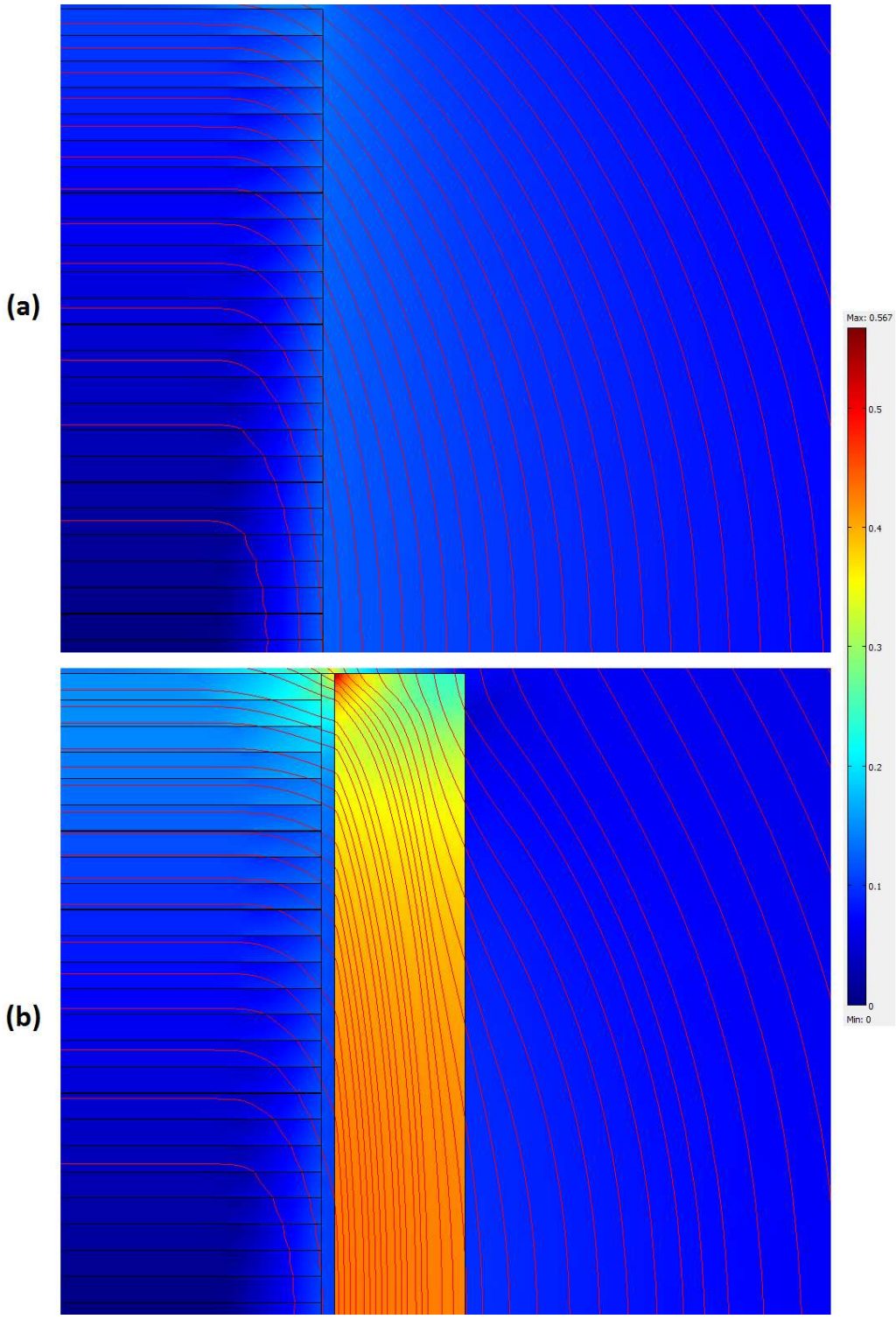

Figure 5.4: Comparison of magnetic flux density profiles, including magnetic flux lines, for a 50 tape stack (a) without and (b) with a flux diverter (weak magnetic material)

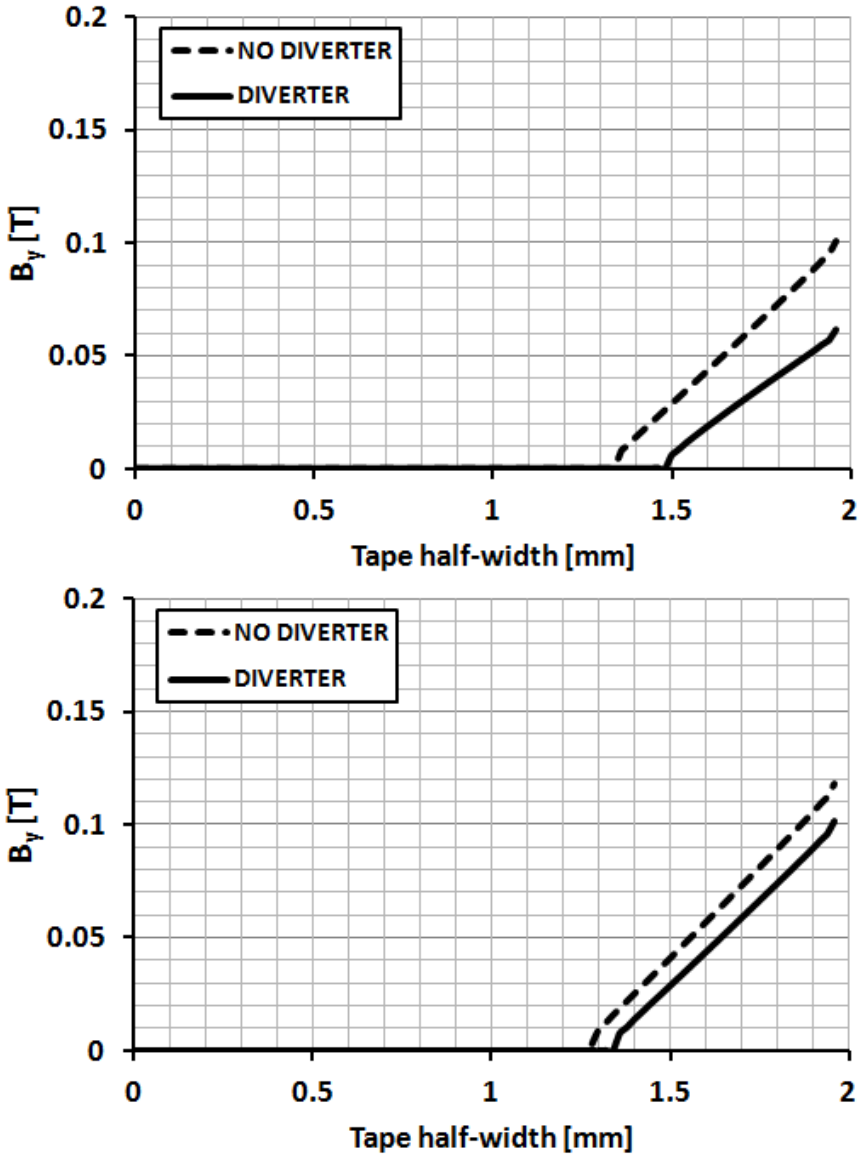

Figure 5.5: Comparison of magnetic flux penetration in tapes located at the 1/5 point (top figure) and centre (bottom figure) for the 50 tape stack (without a magnetic substrate) with and without a diverter

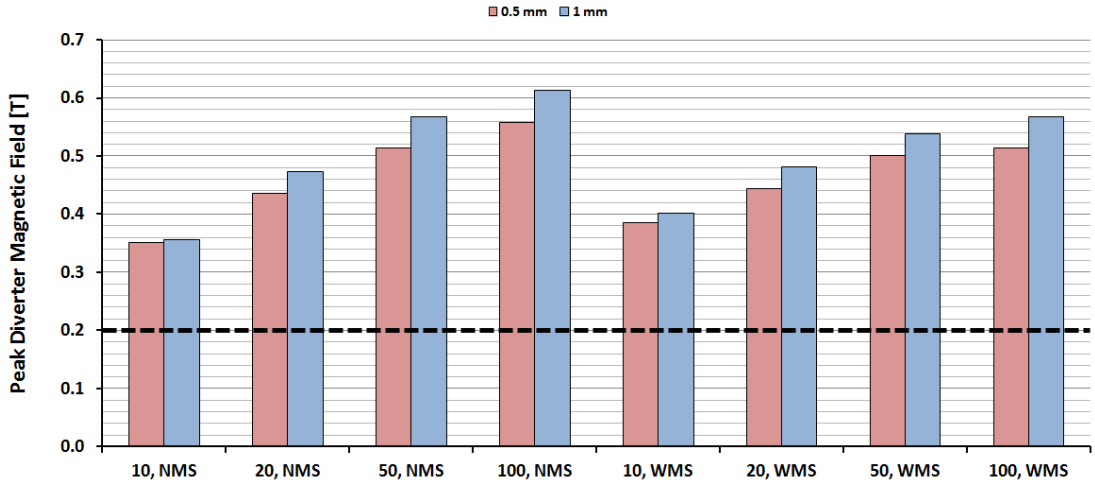

Figure 5.6: Peak diverter magnetic flux density for diverter of weak magnetic material for thicknesses of 0.5 mm and 1 mm for stacks of 10 to 100 tapes with and without a weak magnetic substrate [NMS = non-magnetic substrate, WMS = weakly magnetic substrate]

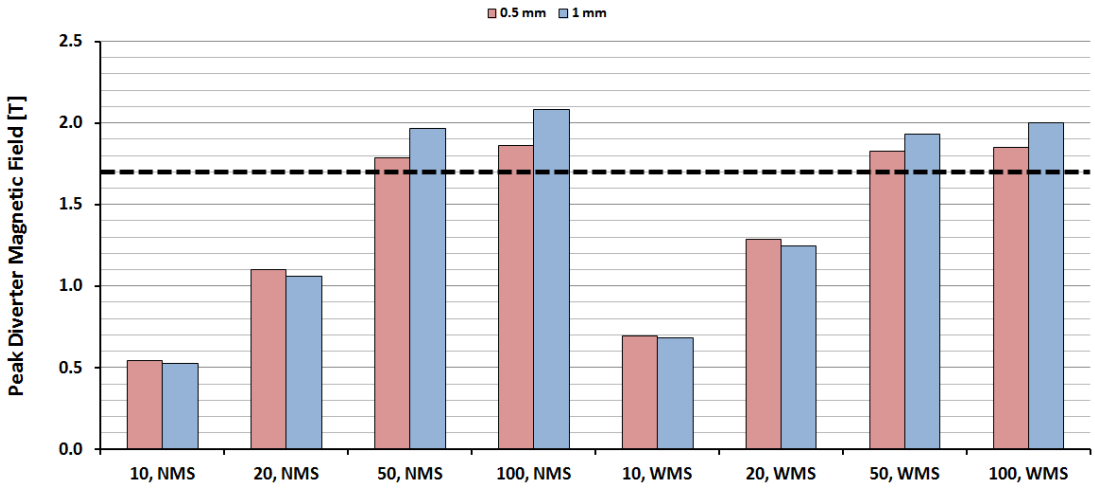

Figure 5.7: Peak diverter magnetic flux density for diverter of strong magnetic material for thicknesses of 0.5 mm and 1 mm for stacks of 10 to 100 tapes with and without a weak magnetic substrate [NMS = non-magnetic substrate, WMS = weakly magnetic substrate]

One shortcoming of this model is that the magnetic material model does not account for the hysteresis loop of the magnetic material, i.e. when the field is removed, the material returns to the virgin magnetisation state rather than having some remanent magnetisation. This is adequate for the AC loss calculation described previously, as the model is combined with experimental results to calculate the total loss. For complete and accurate representation of magnetic materials, hysteresis loops need to be implemented in the model, which is difficult to achieve in finite element modelling. However, this would allow the ferromagnetic losses to be calculated using the model, rather than relying on experimental data for this calculation.

In conclusion, there is significant promise in using magnetic materials as a flux diverter to significantly reduce the AC loss in superconducting coils, although further research is necessary to prove these results experimentally. At the cryogenic temperatures at which the superconductor operates, there is less of a restriction on the number of magnetic materials that could be utilised for this purpose, as operation would occur at temperatures well below the Curie point, the temperature at which a ferromagnetic material becomes paramagnetic and loses its magnetism. Ideally the magnetic material will have a high saturation field (to reduce the losses more and to work for a larger range of coils) and a low remanent field (to reduce the ferromagnetic loss in the diverter itself).

Chapter 6

Conclusions

6.1 Conclusions

In this dissertation, the problem of calculating and measuring AC losses in superconducting coils, with a particular focus on the transport AC loss of coils for electric machines, is addressed. In an electric machine, and indeed in other superconductor-based devices, such as SMES systems and transformers, there are usually multiple superconductors in tape/wire form wound into coils and interacting together in a complex magnetic environment. In order to assess the performance of such devices, it is crucial to have reliable techniques to model and measure the AC losses in complex geometries, since these AC losses increase the refrigeration load, which decreases the overall efficiency and increases the technological complexity of the design. The main contributions of this dissertation are highlighted below.

In order to model the superconducting coil's electromagnetic properties and calculate the AC loss, an existing two dimensional (2D) finite element model that implements a set of equations known as the H formulation, which directly solves the magnetic field components in 2D, was extended to model a superconducting coil, where the cross-section of the coil is modelled as a 2D stack of superconducting coated conductors.

Firstly, the artificial expansion of the thickness of the YBCO layer was investigated using a single tape, as the preliminary groundwork for optimising more complex geometries, which can require hundreds of thousands of mesh elements.

It was found that the thickness may be expanded in the model up to 20-30 μm before the calculated result begins to deviate appreciably from the analytical model used for comparison. The use of edge elements provides the best compromise between the computation time required to solve the model and the accuracy of the solution.

The artificial expansion technique was applied to the geometry of a superconducting racetrack coil of an all-superconducting high-temperature superconductor (HTS) permanent magnet synchronous motor to model the individual turns of the coil. The result is compared with a model using a bulk approximation, which assumes that the tapes couple electromagnetically such that the individual tapes behave as a finite superconducting slab carrying n times the current of each individual tape, where n is the number of tapes. The artificially-expanded, individual tapes model is more accurate than the bulk approximation, as long as the expanded thickness remains within the limits specified above.

A technique, which uses large aspect ratio mapped meshes, is then applied to allow the actual superconducting layer thickness to be modelled without the associated problem of increased computation time due to a large number of mesh elements. In combination with a sparser mapped mesh between the superconducting layers, an overall reduction of about two orders of magnitude in the number of mesh elements was achieved.

The model was modified to allow the inclusion of a magnetic substrate, which is present in some commercially available HTS wire. The analysis raised a number of interesting points regarding the use of superconductors with magnetic substrates. In particular, the presence of a magnetic substrate affects the penetration of the magnetic flux front within the coil and increases the magnetic flux density within the penetrated region, both of which can increase the AC loss significantly. The effect of the substrate loss itself on the overall AC loss can, in general, be neglected, except for a suitably low current. In order to investigate these findings further, a comprehensive analysis on stacks of tapes with weak and strong magnetic substrates was carried out, using a symmetric model that requires only one quarter of the cross-section to be modelled.

In order to validate the modelling results, an extensive experimental setup was designed and built to measure the transport AC loss of a superconducting

coil using an electrical method based on inductive compensation by means of a variable mutual inductance. The variable mutual inductance is utilised to cancel the inductive component of the superconducting coil's voltage, which is 90° out of phase with the current and much larger than the AC loss voltage, which is in-phase with the current. This is used in conjunction with a lock-in amplifier, which can extract a signal with a known carrier wave where the signal-to-noise ratio is very small.

Measurements were carried out on the superconducting racetrack coil and it was found that the experimental results agree with the modelling results for low current. However, some phase drift occurs for higher current, which affects the accuracy of the measurement. In order to overcome this problem, a number of improvements were made to the initial setup to improve the lock-in amplifier's phase setting and other aspects of the measurement technique, including the use of the signal generator's reference (TTL) output and a Rogowski coil to provide stable reference signals to accurately set the reference phase of the lock-in amplifier.

New measurements were carried out on a single, circular pancake coil and the discrepancies between the experimental and modelling results were described in terms of the assumptions made in the model and aspects of the coil that cannot be modelled. Using the original measured properties of the superconducting tape, there is an order of magnitude difference between the experiment and model. The properties of the superconductor can degrade during the winding and cooling processes, and a critical current measurement coil showed that the tape critical current reduced from nearly 300 A, down to around 100 A. Applying this finding to the model, the experimental and modelling results showed good agreement, and the difference in the slope of the AC loss curve can be described in terms of the B-dependent critical current dependency $J_c(B)$ used in the model. Accurate information on the superconductor properties is crucial for estimating the AC loss. The utilisation of voltage taps can provide more information on different regions of the coil and identify areas of weakness, i.e. areas of significant J_c degradation.

Finally, methods used to mitigate AC loss in superconducting wires and coils are summarised, and the use of weak and strong magnetic materials as a flux

diverter is investigated as a technique to reduce AC loss in superconducting coils. This technique can achieve a significant reduction in AC loss and does not require modification to the conductor itself, which can be detrimental to the superconductor's properties.

6.2 Future research

The analyses presented in this dissertation provide a number of interesting results which, combined with addressing some shortcomings in the present modelling and experimental setup, will form the basis for a number of fundamentally interlinked and exciting research topics to be carried out in the future. These are outlined below.

- Modelling technique:

  One shortcoming of the model is that the modelling of magnetic materials does not account for the hysteresis loop of the material. In the current model, when the field is removed, the material returns to its virgin magnetisation state rather than having some remanent magnetisation. This is adequate for the AC loss calculation described in this disseration, as the model is combined with experimental results to calculate the total loss. However, implementing hysteresis loops for magnetic materials would allow ferromagnetic losses to be calculated directly and would alleviate the need to use experimental data.

  For some coil geometries and magnetic environments, the infinitely long approximation may not provide an accurate solution, and axisymmetric modelling of the coil in 2D cylindrical coordinates or extending the model to 3D would provide information on cases where it is applicable and where it is not, for most practical coil geometries. This may be particularly important when calculating the magnetisation AC loss of a superconducting coil due to an applied magnetic field. A 3D model would also allow more complex superconducting coils, such as saddle coils, to be analysed.

  There are a number of approximations that can be made in regards

to the critical current density J_c, and in this dissertation, a constant J_c approximation and a $J_c(B)$ approximation that assumes the perpendicular component dominates the suppression of J_c are used. In reality, there are components at various angles to the tape face, i.e. $J_c(B, \theta)$, and if detailed information on this relationship is provided (either by the manufacturer or by measuring directly), this would improve the modelling further.

- Experimental technique:

  The transport AC loss of a superconducting coil is the focus of this dissertation, but the modelling and experimental setup could be extended to calculate and measure the magnetisation AC loss, which is crucial for the design of a superconducting electric machine, where a superconducting coil may be subjected to a combination of a transport current and an external magnetic field.

  In the final chapter of this dissertation, an investigation on the use of magnetic materials as a flux diverter was presented as a technique to reduce AC loss in superconducting coils. The results of this investigation show significant promise for this technique, but further research is required to prove these results experimentally.

Appendix 1

AC loss calculation example using a superconducting slab

In this section, an example of an AC loss calculation for a superconducting slab is given [156]. The superconducting slab is infinitely long in the y and z directions, and has a finite width in the x direction. According to Bean's model, transport current begins to penetrate from the edge of a slab. If a coordinate system is chosen such that 0 corresponds to the point of full penetration for the maximum transport current and s corresponds to the surface of the slab. Ampere's law states that

$$\nabla \times \mathbf{H} = \mathbf{J} \tag{1}$$

and for only one dimension, the equation reduces to

$$\frac{\mathrm{dH(x)}}{\mathrm{dx}} = \mathrm{J(x)} \tag{2}$$

Bean's model:

$$\frac{\mathrm{dH(x)}}{\mathrm{dx}} = \mathrm{J_c} \tag{3}$$

Integrating both sides and assuming that the field is zero at the penetration point:

$$\mathrm{H(x)} = \mathrm{J_c x} \tag{4}$$

Similarly, for the minimum transport current, -I, the field is

$$\mathrm{H(x)} = -\mathrm{J_c x} \tag{5}$$

The enclosed flux per unit length in the 'positive' half of the slab for currents -I and I can be determined by

$$\phi(\mathrm{x},0) = \int_0^{\mathrm{x}} \mathrm{B(x,0)}\,\mathrm{dx} = \int_0^{\mathrm{x}} \mu_0 \mathrm{H(x,0)}\,\mathrm{dx} = \int_0^{\mathrm{x}} -\mu_0 \mathrm{J_c x}\,\mathrm{dx} = -\frac{\mu_0 \mathrm{J_c x^2}}{2} \tag{6}$$

Similarly,

$$\phi(\mathrm{x}, \frac{\mathrm{T}}{2}) = \frac{\mu_0 \mathrm{J_c x^2}}{2} \tag{7}$$

The total AC loss per cycle of current per unit area of the slab can be determined using equation 2.25:

$$\frac{\mathrm{Q}}{\mathrm{S}} = 2\int_0^{\mathrm{T}} \int_0^{\mathrm{p}} \mathrm{E}\cdot\mathrm{J_c}\,\mathrm{dx}\,\mathrm{dt} = 4\mathrm{J_c}\int_0^{\frac{\mathrm{T}}{2}} \int_0^{\mathrm{p}} \mathrm{E}\,\mathrm{dx}\,\mathrm{dt} \tag{8}$$

where p is the penetration depth. $\mathrm{E} = 0$ in the slab when $\mathrm{J} = 0$, so the electric field can be solved using Faraday's law:

$$\frac{\mathrm{Q}}{\mathrm{S}} = 4\mathrm{J_c}\int_0^{\frac{\mathrm{T}}{2}} \int_0^{\mathrm{p}} \frac{\mathrm{d}\phi(\mathrm{x,t})}{\mathrm{dt}}\,\mathrm{dx}\,\mathrm{dt} \tag{9}$$

Changing the order of integration:

$$\begin{aligned}
\frac{\mathrm{Q}}{\mathrm{S}} &= 4\mathrm{J_c}\int_0^{\mathrm{p}}\int_0^{\frac{\mathrm{T}}{2}}\frac{\mathrm{d}\phi(\mathrm{x},\mathrm{t})}{\mathrm{dt}}\,\mathrm{dt}\,\mathrm{dx} \\
&= 4\mathrm{J_c}\int_0^{\mathrm{p}}(\phi(\mathrm{x},\frac{\mathrm{T}}{2})-\phi(\mathrm{x},0))\,\mathrm{dx} \\
&= 4\mathrm{J_c}\int_0^{\mathrm{p}}\mu_0\mathrm{J_c}\mathrm{x}^2\,\mathrm{dx} \\
&= 4\mu_0\mathrm{J_c^2}\int_0^{\mathrm{p}}\mathrm{x}^2\,\mathrm{dx} \\
&= \frac{4}{3}\mu_0\mathrm{J_c^2}\mathrm{s}^3
\end{aligned} \tag{10}$$

To investigate this equation numerically, the following assumptions can be made:

- Slab width = 1 mm

  Thus, s = 0.5 mm

- $\mathrm{J_c} = 1\times10^5$ A/m^2

  Thus, critical current of the slab per unit length along the y axis is 50 A/m

- Transport current of 40 A/m

  Thus, the penetration depth, p, is

$$\mathrm{p} = \frac{\mathrm{I}}{\mathrm{I_c}}\mathrm{s} = 4\times10^{-4}\mathrm{m}\ (0.4\ \mathrm{mm}) \tag{11}$$

This gives a total AC loss of

$$\frac{\mathrm{Q}}{\mathrm{S}} = \frac{4}{3}\mu_0\mathrm{J_c^2}\mathrm{p}^3 \approx 1.07\times10^{-6}\ [\mathrm{J/cycle/m^2}] \tag{12}$$

Appendix 2

Derivation of equation for mutual inductance of compensation coil

The equation for the mutual inductance of the compensation coil is derived as follows.

The magnetic field from a current element in the Biot-Savart law is given by

$$d\mathbf{B} = \mu_0 \frac{Id\mathbf{L} \times \mathbf{r}}{4\pi r_1^2} \tag{13}$$

Therefore,

$$dB = \mu_0 \frac{IdLsin\theta}{4\pi r_1^2} \tag{14}$$

which, in the case of a circular current loop of radius r_1, becomes

$$B = \frac{\mu_0 I}{4\pi r_1^2} \oint dL = \frac{\mu_0 I}{4\pi r_1^2} 2\pi r_1 = \frac{\mu_0 I}{2r_1} \tag{15}$$

In the case of a circular loop of N_1 turns, i.e. the compensation coil primary coil, this becomes

$$B = \frac{\mu_0 N_1 I}{2r_1} \tag{16}$$

For a loop of N_2 turns placed inside of this coil, i.e., the compensation coil secondary coil, of a small enough radius such that B is assumed constant, the

mutual inductance is defined as

$$M = \frac{N_2 \Phi_{21}}{I} \tag{17}$$

where Φ_{21} is the flux linked by the secondary coil and is given by

$$\Phi_{21} = \Phi_1 \frac{A_2}{A_1} \tag{18}$$

where $\Phi_1 = B \cdot A_1$, which results in $\Phi_{21} = B \cdot A_2$.
The mutual inductance is then

$$M = \frac{N_2 B A_2}{I} \tag{19}$$

where $A_2 = \pi r_2^2$ and $B = \frac{\mu_0 N_1 I}{2 r_1}$, which gives

$$M = \mu_0 N_1 N_2 \frac{\pi}{2} \frac{r_2^2}{r_1} \tag{20}$$

References

[1] Energy Information Administration, U.S. Department of Energy. International Energy Outlook 2009. [Online]. Available: http://www.eia.doe.gov/oiaf/ieo/ 1

[2] U.S. Energy Information Administration, "Annual Energy Review 2010: Energy Consumption Estimates by Sector Overview," 2010. 1

[3] ABB, "ABB drives and motors for improving energy efficiency," 2010. 1

[4] C. McNaught, "Running smoothly: making motors more efficient," *IEE Review*, vol. 39, no. 2, pp. 89–91, 1993. 1

[5] H. K. Onnes, *Comm. Phys. Lab. Univ. Leiden*, pp. 119,120,122, 1911. 7

[6] W. Meissner and R. Ochsenfeld, *Naturewiss*, vol. 21, p. 787, 1933. 8, 9

[7] M. Tinkham, *Introduction to Superconductivity*, 2nd ed. Dover Publications, 1996. 8

[8] F. and H. London, "The electromagnetic equations of the supraconductor," *Proc. Roy. Soc.*, vol. 149, no. 866, pp. 71–88, 1935. 9, 33

[9] V. L. Ginzburg and L. D. Landau, *Zh. Eksp. Teor. Fiz.*, vol. 20, p. 1064, 1950. 9

[10] J. Bardeen, L. N. Cooper, and J. R. Schrieffer, "Microscopic theory of superconductivity," *Phys. Rev.*, vol. 106, pp. 162–164, 1957. 9

[11] A. A. Abrikosov, "On the magnetic properties of superconductors of the second group," *Sov. Phys. JETP-USSR*, vol. 5, no. 6, pp. 1174–1183, 1957. 9

[12] A. C. Rose-Innes and E. H. Rhoderick, *Introduction to Superconductivity*, revised 2nd ed. Pergamon Press, 1994, pp. 183–194. 9

[13] Laboratory of Advanced Energy Systems, Helsinki University of Technology. High-Temperature Superconductivity. [Online]. Available: http://tfy.tkk.fi/aes/AES/projects/prlaser/supercond.htm 9, 11, 13

[14] A. A. Golubov, *Handbook of Applied Superconductivity*. IOP Publishing, 1998, vol. 1, ch. A1: The evolution of superconducting theories, pp. 3–36. 9, 10

[15] C. P. Poole, *Superconductivity*, 2nd ed. Elsevier Ltd., 2007. 9, 19, 20, 23

[16] A. C. Fischer-Cripps, *The Material Physics Companion*. Taylor & Francis, 2008, p. 192. 9

[17] G. Fuchs and L. Schultz, *Concise Encyclopedia of Magnetic and Superconducting Materials*, 2nd ed. Elsevier, 2005, ch. Superconducting Permanent Magnets: Principles and Results, pp. 1166–1174. 10

[18] P. Lee, Ed., *Engineering Superconductivity*. John Wiley & Sons, 2001. 10, 11

[19] Oak Ridge National Laboratory. Fundamentals of Superconductors. [Online]. Available: http://www.ornl.gov/info/reports/m/ornlm3063r1/pt3.html 10

[20] D. A. Cardwell, "Processing and properties of large grain (RE)BCO," *Materials Science and Engineering: B*, vol. 53, no. 1-2, pp. 1–10, 1998. 11

[21] Coalition for the Commercial Applications of Superconductivity (CCAS). Superconductivity. [Online]. Available: http://www.ccas-web.org/superconductivity/ 12

[22] D. U. Gubser, "Superconductivity: An emerging power-dense energy-efficient technology," *IEEE Trans. Appl. Supercond.*, vol. 14, no. 4, pp. 2037–2046, Dec 2004. 11

[23] Hoffman Lab. Superconducting Cuprates. [Online]. Available: http://hoffman.physics.harvard.edu/materials/CuprateIntro.php 11

[24] J. G. Bednorz and K. A. Muller, "Possible high Tc superconductivity in the Ba-La-Cu-O system," *Zeitschrift fur Physik B Condensed Matter*, vol. 64, no. 2, pp. 189–193, 1986. 11

[25] B. Oswald, *Concise Encyclopedia of Magnetic and Superconducting Materials*, 2nd ed. Elsevier, 2005, ch. Superconducting Permanent Magnets: Potential Applications, pp. 1164–1166. 13

[26] American Superconductor. American Superconductor. [Online]. Available: http://www.amsc.com 13, 42

[27] SuperPower Inc. HTS Materials Technology. [Online]. Available: http://www.superpower-inc.com/ 13, 15

[28] X. Li *et al.*, "The development of second generation HTS wire at American Superconductor," *IEEE Trans. Appl. Supercond.*, vol. 19, no. 3, pp. 3231–3235, 2009. 15

[29] Z. Hong, A. M. Campbell, and T. A. Coombs, "Numerical solution of critical state in superconductivity by finite element software," *Supercond. Sci. Technol.*, vol. 19, pp. 1246–1252, 2006. 14, 37, 78

[30] R. Pecher, M. D. McCulloch, S. J. Chapman, L. Prigozhin, and C. M. Elliott, "3D-modelling of bulk type-II superconductors using unconstrained H-formulation," in *Proceedings of the 6th EUCAS*, 2003, pp. 1–11. 16

[31] C. P. Bean, "Magnetization of hard superconductors," *Phys. Rev. Lett.*, vol. 8, p. 250, 1962. 16, 18, 32

[32] Y. B. Kim, C. F. Hempstead, and A. R. Strnad, "Critical persistent currents in hard superconductors," *Phys. Rev. Lett.*, vol. 9, no. 7, pp. 306–309, 1963. 16, 19, 24

[33] P. W. Anderson, "Theory of flux creep in hard superconductors," *Phys. Rev. Lett.*, vol. 9, no. 7, pp. 309–311, 1963. 16, 19, 23, 24

[34] J. Rhyner, "Magnetic properties and AC-losses of superconductors with power law current-voltage characteristics," *Physica C*, vol. 212, pp. 292–300, 1993. 16, 23

[35] A. A. Golubov, *Handbook of Applied Superconductivity.* IOP Publishing, 1998, vol. 1, ch. A2: Type II superconductivity, pp. 37–52. 16, 29

[36] W. J. Carr, *AC loss and macroscopic theory of superconductors*, 2nd ed. CRC Press, 2001. 17, 27, 29, 30

[37] S. Stavrev *et al.*, "Comparison of numerical methods for modeling of superconductors," *IEEE Trans. Mag.*, vol. 38, no. 2, pp. 849–852, Mar 2002. 17, 23, 37

[38] E. H. Brandt and M. Indenbom, "Type-II superconductor strip with current in a perpendicular magnetic field," *Phys. Rev. B*, vol. 48, no. 17, pp. 12 893–12 906, 1993. 21, 35, 47

[39] E. H. Brandt, "Superconductors of finite thickness in a perpendicular magnetic field: strips and slabs," *Phys. Rev. B*, vol. 54, pp. 4246–4264, 1996. 21, 35

[40] N. Nibbio, S. Stavrev, and B. Dutoit, "Finite Element Method simulation of AC loss in HTS tapes with B-dependent E-J power law," *IEEE Trans. Appl. Supercond.*, vol. 11, no. 1, pp. 2631–2634, Mar 2001. 25

[41] Q. Jiang, M. Majoros, Z. Hong, A. M. Campbell, and T. A. Coombs, "Design and AC loss analysis of a superconducting synchronous motor," *Supercond. Sci. Technol.*, vol. 19, pp. 1164–1168, 2006. 25, 42

[42] J. Souc, E. Pardo, M. Vojenciak, and F. Gomory, "Theoretical and experimental study of AC loss in high temperature superconductor single pancake coils," *Supercond. Sci. Technol.*, vol. 22, no. 015006, 2009. 25, 41

[43] F. Gomory, M. Vojenciak, E. Pardo, M. Solovyov, and J. Souc, "AC losses in coated conductors," *Supercond. Sci. Technol.*, vol. 23, no. 034012, 2010. 25, 122

[44] M. Vojenciak, F. Grilli, S. Terzieva, W. Goldacker, M. Kovacova, and A. Kling, "Effect of self-field on the current distribution in Roebel-assembled coated conductor cables," *Supercond. Sci. Technol.*, vol. 24, no. 095002, 2011. 25, 120

[45] E. Pardo, M. Vojenciak, F. Gomory, and J. Souc, "Low-magnetic-field dependence and anisotropy of the critical current density in coated conductors," *Supercond. Sci. Technol.*, vol. 24, no. 065007, 2011. 25

[46] M. P. Oomen, "AC loss in superconducting tapes and cables," Ph.D. dissertation, University of Twente, Enschede, The Netherlands, 2000. 27, 28

[47] P. N. Barnes, M. D. Sumption, and G. L. Rhoads, "Review of high power density superconducting generators: present state and prospects for incorporating YBCO windings," *Cryogenics*, vol. 45, pp. 670–686, 2005. 28

[48] J. J. Rabbers, "AC loss in superconducting tapes and coils," Ph.D. dissertation, University of Twente, Enschede, The Netherlands, 2001. 28, 29, 30, 33, 91, 92, 94

[49] Z. Hong, A. M. Campbell, and T. A. Coombs, "Computer modeling of magnetisation in high temperature bulk superconductors," *IEEE Trans. Appl. Supercond.*, vol. 17, no. 2, pp. 3761–3764, Jun 2007. 29

[50] M. M. Farhoudi, "AC loss in Ag/Bi-2223 tapes in AC field," Master's thesis, University of Wollongong, Wollongong, Australia, 2005. 30

[51] W. T. Norris, "Calculation of hysteresis loss in hard superconductors carrying ac: isolated conductors and edges of thin sheets," *J. Phys. D: Appl. Phys.*, vol. 3, pp. 489–507, 1969. 33, 34, 78, 97

[52] G. Barnes, M. McCulloch, and D. Dew-Hughes, "Computer modelling of type II superconductors in applications," *Supercond. Sci. Technol.*, vol. 12, pp. 518–522, 1999. 37

[53] L. Prigozhin, "Analysis of critical-state problems in type-II superconductivity," *IEEE Trans. Appl. Supercond.*, vol. 7, pp. 3866–3873, 1997. 37

[54] A. M. Campbell, "A direct method for obtaining the critical state in two and three dimensions," *Supercond. Sci. Technol.*, vol. 22, no. 034005, 2009. 37

[55] N. Amemiya, K. Miyamoto, S. Murasawa, H. Mukai, and K. Ohmatsu, "Finite element analysis of AC loss in non-twisted Bi-2223 tape carrying AC transport current and/or exposed to DC or AC external magnetic field," *Physica C*, vol. 310, pp. 30–35, 1998. 37

[56] J. K. Sykulski, R. L. Stoll, A. E. Mahdi, and C. P. Please, "Modelling HTc superconductors for AC power loss estimation," *IEEE Trans. Magn.*, vol. 33, no. 2, pp. 1568–1571, 1997. 37, 89

[57] J. K. Sykulski, M. Rotaru, and R. L. Stoll, "Highly non-linear field diffusion in HTC superconducting tapes," *COMPEL*, vol. 18, no. 2, pp. 215–224, 1999. 37

[58] ——, "2D modeling and field diffusion and AC losses in high temperature superconducting tapes," *IEEE Trans. Magn.*, vol. 36, no. 4, pp. 1178–1182, 2000. 37

[59] K. Kajikawa, "Numerical evaluation of AC losses in HTS wires with 2D FEM formulated by self magnetic field," *IEEE Trans. Appl. Supercond.*, vol. 13, no. 2, pp. 3630–3633, 2003. 37

[60] R. Brambilla, F. Grilli, and L. Martini, "Development of an edge-element model for AC loss computation of high-temperature superconductors," *Supercond. Sci. Technol.*, vol. 20, pp. 16–24, 2007. 37

[61] F. Sirois, M. Dione, F. Roy, F. Grilli, and B. Dutoit, "Evaluation of two commercial finite element packages for calculating AC losses in 2-D high temperature superconducting strips," *J. Phys.: Conf. Ser.*, vol. 97, no. 012030, 2008. 37

[62] F. Grilli, R. Brambilla, and L. Martini, "Modeling High-Temperature Superconducting Tapes by Means of Edge Finite Elements," *IEEE Trans. Appl. Supercond.*, vol. 17, no. 2, pp. 3155–3158, 2007. 37, 41, 52, 78

[63] P. Vanderbemden, Z. Hong, T. A. Coombs, S. Denis, M. Ausloos, J. Schwartz, I. B. Rutel, N. H. Babu, D. A. Cardwell, and A. M. Campbell, "Behaviour of bulk high-temperature superconductors of finite thickness subjected to crossed magnetic fields: experiment and model," *Phys. Rev. B*, vol. 75, no. 174515, 2007. 38

[64] Y. Mawatari, "Critical state of periodically arranged superconducting-strip lines in perpendicular fields," *Phys. Rev. B*, vol. 54, pp. 13 215–13 221, 1996. 41

[65] K.-H. Muller, "Self-field hysteresis loss in periodically arranged superconducting strips," *Physica C*, vol. 289, no. 1-2, pp. 123–130, 1997. 41

[66] J. R. Clem, J. H. Claassen, and Y. Mawatari, "AC losses in a finite Z stack using an anisotropic homogeneous-medium approximation," *Supercond. Sci. Technol.*, vol. 20, pp. 1130–1139, 2007. 41, 47, 78

[67] W. Yuan, A. M. Campbell, and T. A. Coombs, "A model for calculating the AC losses of second-generation high temperature superconductor pancake coils," *Supercond. Sci. Technol.*, vol. 22, no. 075028, 2009. 41, 47, 97

[68] ——, "ac losses and field and current density distribution during a full cycle of a stack of superconducting tapes," *J. Appl. Phys.*, vol. 107, no. 093909, 2010. 41

[69] W. Yuan, A. M. Campbell, Z. Hong, M. D. Ainslie, and T. A. Coombs, "Comparison of AC losses, magnetic field/current distributions and critical currents of superconducting circular pancake coils and infinitely long stacks

using coated conductors," *Supercond. Sci. Technol.*, vol. 23, no. 085011, 2010. 41

[70] E. Pardo, "Modeling of coated conductor pancake coils with a large number of turns," *Supercond. Sci. Technol.*, vol. 21, no. 065014, 2008. 41, 78

[71] L. Prigozhin and V. Sokolovsky, "Computing AC losses in stacks of high-temperature superconducting tapes," *Supercond. Sci. Technol.*, vol. 24, no. 075012, 2011. 41, 78

[72] D. N. Nguyen, S. P. Ashworth, J. O. Willis, F. Sirois, and F. Grilli, "A new finite-element method simulation model for computing AC loss in roll assisted biaxially textured substrate YBCO tapes," *Supercond. Sci. Technol.*, vol. 23, no. 025001, 2010. 41, 66, 67, 76

[73] D. N. Nguyen, J. Y. Coulter, J. O. Willis, S. P. Ashworth, H. P. Kraemer, W. Schmidt, B. Carter, and A. Otto, "AC loss and critical current characterization of a noninductive coil of two-in-hand RABiTS YBCO tape for fault current limiter applications," *Supercond. Sci. Technol.*, vol. 24, no. 035017, 2011. 41

[74] Y. Jiang, R. Pei, Q. Jiang, Z. Hong, and T. A. Coombs, "Control of a superconducting synchronous motor," *Supercond. Sci. Technol.*, vol. 20, pp. 392–396, 2007. 42

[75] Y. Jiang, R. Pei, Z. Hong, J. Song, F. Fang, and T. A. Coombs, "Design and control of a superconducting permanent magnet synchronous motor," *Supercond. Sci. Technol.*, vol. 20, pp. 585–591, 2007. 42

[76] Y. Jiang, R. Pei, Z. Hong, Q. Jiang, and T. A. Coombs, "Design of an HTS motor," *J. of Phys.: Conf. Ser.*, vol. 97, no. 012123, 2008. 42, 43, 46

[77] Y. Jiang, R. Pei, W. Xian, Z. Hong, and T. A. Coombs, "The design, magnetization and control of a superconducting permanent magnet synchronous motor," *Supercond. Sci. Technol.*, vol. 21, no. 065011, 2008. 42, 94

[78] Y. Jiang, R. Pei, W. Xian, Z. Hong, W. Yuan, R. Marchant, and T. A. Coombs, "Magnetization process of an HTS motor and the torque ripple suppression," *IEEE Trans. Appl. Supercond.*, vol. 19, no. 3, pp. 1644–1647, 2009. 42

[79] W. Xian, W. Yuan, and T. A. Coombs, "Numerical assessment of efficiency and control stability of an HTS synchronous motor," *J. of Phys.: Conf. Ser.*, vol. 234, no. 032063, 2010. 42

[80] R. Pei, A. Velichko, M. Majoros, Y. Jiang, R. Viznichenko, Z. Hong, R. Marchant, A. M. Campbell, and T. A. Coombs, "Ic and AC loss of 2G YBCO tape measurement for designing and fabrication of an HTS motor," *IEEE Trans. Appl. Supercond.*, vol. 18, no. 2, pp. 1236–1239, Jun 2008. 42, 92

[81] R. Pei, A. Velichko, Z. Hong, Y. Jiang, W. Yuan, A. M. Campbell, and T. A. Coombs, "Numerical and experimental analysis of I_c and AC loss for bent 2G HTS wires used in an electric machine," *IEEE Trans. Appl. Supercond.*, vol. 19, no. 3, pp. 3356–3360, 2009. 42

[82] Y. Jiang, "The design and control of a superconducting motor," Ph.D. dissertation, University of Cambridge, Cambridge, UK, 2009. 44

[83] R. Brambilla, F. Grilli, L. Martini, and F. Sirois, "Integral equations for the current density in thin conductors and their solution by the finite-element method," *Supercond. Sci. Technol.*, vol. 21, no. 105008, 2008. 56

[84] V. M. Zermeno-Rodriguez, M. P. Sorensen, N. F. Pedersen, N. Mijatovic, and A. Abrahamsen, "Fast 2D simulation of superconductors: a multiscale approach." 61

[85] V. M. Zermeno-Rodriguez, N. Mijatovic, C. Traeholt, T. Zirngibl, E. Seiler, A. B. Abrahamsen, N. F. Pedersen, and M. P. Sorensen, "Towards faster FEM simulation of thin film superconductors: a multiscale approach," *IEEE Trans. Appl. Supercond.*, vol. 21, no. 3, pp. 3273–3276, 2011. 61

[86] D. Miyagi, Y. Yunoki, M. Umabachi, N. Takahashi, and O. Tsukamoto, "Measurement of magnetic properties of Ni-alloy substrate of HTS coated conductor in LN_2," *Physica C*, vol. 468, pp. 1743–1746, 2008. 66, 75

[87] S. Kapa and P. Capper, Eds., *Springer Handbook of Electronic and Photonic Materials*, 1st ed. Springer, 2007, p. 1195. 70, 71

[88] S. P. Mehta, N. Aversa, and M. S. Walker, "Tranforming transformers," *IEEE Spectrum*, vol. 34, no. 7, pp. 43–49, 1997. 71

[89] PowerStream Technologies. American Wire Gauge table and AWG Electrical Current Load Limits with skin depth frequencies. [Online]. Available: http://www.powerstream.com/Wire_Size.htm 72

[90] M. D. Ainslie, Y. Jiang, W. Xian, Z. Hong, W. Yuan, R. Pei, T. J. Flack, and T. A. Coombs, "Numerical analysis and finite element modelling of an HTS synchronous motor," *Physica C*, vol. 450, no. 2, pp. 1752–1755, 2010. 73, 74

[91] J. Evetts, Ed., *Concise Encyclopedia of Magnetic & Superconducting Materials*, 1st ed. Pergamon Press, 1992, pp. 19–22. 91

[92] C. Schmidt, K. Itoh, and H. Wada, "Second VAMAS a.c. loss measurement intercomparison: a.c. magnetization measurement of hysteresis and coupling losses in NbTi multifilamentary strands," *Cryogenics*, vol. 37, no. 2, pp. 77–89, 1997. 91

[93] P. Dolez, M. Aubin, W. Zhu, and J. Cave, "A comparison between ac losses obtained by the null calorimetric and a standard electrical method," *Supercond. Sci. Technol.*, vol. 11, pp. 1386–1390, 1998. 92

[94] A. E. Mahdi *et al.*, "Thermometric measurements of the self-field losses in silver sheathed PbBi2223 multifilimentary tapes," *IEEE Trans. Appl. Supercond.*, vol. 7, no. 2, pp. 1658–1661, 1997. 92

[95] J.-H. Kim, C. H. Kim, G. Iyyani, J. Kvitkovic, and S. Pamidi, "Transport AC loss measurements in superconducting coils," *IEEE Trans. Appl. Supercond.*, vol. 21, no. 3, pp. 3269–3272, 2011. 92

[96] J. Kokavec, I. Hlasnik, and S. Fukui, "Very sensitive electric method for AC measurement in SC coils," *IEEE Trans. Appl. Supercond.*, vol. 3, no. 1, pp. 153–155, 1993. 92

[97] H. Okamoto, F. Sumiyoshi, K. Miyoshi, and Y. Suzuki, "The nitrogen boil-off method for measuring AC loss in HTS coils," *IEEE Trans. Appl. Supercond.*, vol. 16, no. 2, pp. 105–108, 2006. 92

[98] B. Armen. Phase sensitive detection: the lock-in amplifier. [Online]. Available: http://www.phys.utk.edu/labs/modphys/Lock-InAmplifierExperiment.pdf 93

[99] W. Yuan, "Second-generation high-temperature superconducting coils and their applications for energy storage," Ph.D. dissertation, University of Cambridge, Cambridge, UK, 2010. 94, 107

[100] H. Daffix and P. Tixador, "Electrical AC loss measurements in superconducting coils," *IEEE Trans. Appl. Supercond.*, vol. 7, no. 2, pp. 286–289, 1997. 94

[101] M. P. Oomen, "AC Losses in HTS Conductors, Cables and Coils," in *Flux Pinning and AC Loss Studies on YBCO Coated Conductors*, 1st ed., M. P. Paranthaman and V. Selvamanickam, Eds. Nova. 97

[102] L. Jansak, "ac self-field loss measurement system," *Rev. Sci. Instrum.*, vol. 70, no. 7, pp. 3087–3091, 1999. 103, 104, 116

[103] S. Ashworth, Los Alamos National Laboratory, "Measurement of AC losses in HTS conductors," ASC 2008 Short Course: Testing of superconducting wires and coils. 104

[104] M. P. Oomen, W. Herkert, D. Bayer, W. Nick, and T. Arndt, "Manufacturing and test of 2G-HTS coils for rotating machines: Challenges, conductor requirements, realisation," 2011, EUCAS 2011 conference invited presentation. 107

[105] T. Takematsu, R. Hu, T. Takao, Y. Yanagisawa, H. Nakagome, D. Uglietti, T. Kiyoshi, M. Takahashi, and H. Maeda, "Degradation of the performance of a YBCO-coated conductor double pancake coil due to epoxy impregnation," *Physica C*, vol. 470, no. 17-18, pp. 674–677, 2010. 107

[106] M. Sugano, T. Nakamura, K. Shikimachi, N. Hirano, and S. Nagaya, "Stress tolerance and fracture mechanism of solder joint of YBCO coated conductors," *IEEE Trans. Appl. Supercond.*, vol. 17, no. 2, pp. 3067–3070, 2007. 107

[107] D. Miyagi and O. Tsukamoto, "Characteristics of AC transport current losses in YBCO coated conductors and their dependence on distributions of critical current density in the conductors," *IEEE Trans. Appl. Supercond.*, vol. 12, no. 1, pp. 1628–1631, 2002. 108, 110

[108] F. Grilli and S. P. Ashworth, "Measuring transport AC losses in YBCO-coated conductor coils," *Supercond. Sci. Technol.*, vol. 20, pp. 794–799, 2007. 108

[109] ——, "Quantifying AC losses in YBCO coated conductor coils," *IEEE Trans. Appl. Supercond.*, vol. 17, no. 2, pp. 3187–3190, 2007. 108

[110] S. Ashworth, D. Nguyen, J.-H. Kim, C. H. Kim, and S. Pamidi, "Experimental and numerical studies for ac losses in IBAD and RABiTS YBCO coils," 2011, 2011 CEC/ICMC conference presentation. 110

[111] M. Polak, L. Krempasky, S. Chromik, D. Wehler, and B. Moenter, "Magnetic field in the vicinity of YBCO thin film strip and strip with filamentary structure," *Physica C*, vol. 372-376, pp. 1830–1834, 2002. 119

[112] M. Majoros, R. I. Tomov, B. A. Glowacki, A. M. Campbell, and C. E. Oberly, "Hysteretic losses in YBCO coated conductors on textured metallic substrates," *IEEE Trans. Appl. Supercond.*, vol. 13, pp. 3626–3629, 2003. 119

[113] N. Amemiya, K. Yoda, S. Kasai, Z. Jiang, G. A. Levin, P. N. Barnes, and C. E. Oberly, "AC loss characteristics of multifilamentary YBCO coated

conductors," *IEEE Trans. Appl. Supercond.*, vol. 15, no. 2, p. 1637, 2005. 119

[114] N. Amemiya, Q. Li, R. Nishino, K. Takeuchi, T. Nakamura, K. Ohmatsu, M. Ohya, O. Maruyama, T. Okuma, and T. Izumi, "Lateral critical current density distributions degraded near edges of coated conductors through cutting processes and their influence on ac loss characteristics of power transmission cables," *Physica C*, vol. Article in press, 2011. 119

[115] C. B. Cobb, P. N. Barnes, T. J. Haugan, J. Tolliver, E. Lee, M. Sumption, E. Collings, and C. E. Oberly, "Hysteretic loss reduction in striated YBCO," *Physica C*, vol. 382, no. 1, pp. 52–56, 2002. 119

[116] M. Polak, E. Usak, L. Jansak, E. Demencik, G. A. Levin, P. N. Barnes, D. Wehler, and B. Moenter, "Coupling losses and transverse resistivity of multifilament YBCO coated superconductors," *J. Phys.: Conf. Ser.*, vol. 43, pp. 591–594, 2006. 119

[117] M. Polak, J. Kvitkovic, P. Mozola, P. N. Barnes, and G. A. Levin, "Characterization of Individual Filaments in a Multifilamentary YBCO Coated Conductor," *IEEE Trans. Appl. Supercond.*, vol. 17, no. 2, pp. 3163–3166, 2007. 119

[118] N. Amemiya, S. Kasai, K. Yoda, Z. Jiang, G. A. Levin, P. N. Barnes, and C. E. Oberly, "AC loss reduction of YBCO coated conductors by multifilamentary structure," *Supercond. Sci. Technol.*, vol. 17, pp. 1464–1471, 2004. 119

[119] M. Majoros, B. A. Glowacki, and A. M. Campbell, "Transport ac losses and screening properties of Bi-2223 multifilamentary tapes covered with magnetic materials," *Physica C*, vol. 338, pp. 251–262, 2000. 119, 122

[120] S. Terzieva, M. Vojenciak, F. Grilli, R. Nast, J. Souc, W. Goldacker, A. Jung, A. Kudymow, and A. Kling, "Investigation of the effect of striated strands on the AC losses of 2G Roebel cables," *Supercond. Sci. Technol.*, vol. 24, no. 045001, 2011. 119

[121] G. Majkic, I. Kesgin, Y. Zhang, Y. Qiao, R. Schmidt, and V. Selvamanickam, "Ac loss filamentization of 2G HTS tapes by buffer stack removal," *IEEE Trans. Appl. Supercond.*, vol. 21, no. 3, pp. 3297–3300, 2011. 119

[122] B. W. Han, S. H. Park, W. S. Kim, J. K. Lee, S. Lee, S. B. Byun, C. Park, B. W. Lee, K. Choi, and S. Hahn, "Non-contact measurement of current distribution in striated CTCC," *IEEE Trans. Appl. Supercond.*, vol. 20, no. 3, pp. 1952–1955, 2010. 119

[123] M. Polak, S. Takacs, P. N. Barnes, and G. A. Levin, "The effect of resistive filament interconnections on coupling losses in filamentary $YBa_2Cu_3O_7$ coated conductors," *Supercond. Sci. Technol.*, vol. 22, no. 025016, 2009. 119

[124] W. Goldacker, A. Frank, R. Heller, S. I. Schlachter, B. Ringsdorf, K.-R. Weiss, C. Schmidt, and S. Schuller, "ROEBEL Assembled Coated Conductors (RACC): Preparation, Properties and Progress," *IEEE Trans. Appl. Supercond.*, vol. 17, no. 2, pp. 3398–3401, 2007. 120, 121

[125] D. S. Beard, W. Klose, S. Shimamoto, and G. Vecsey, "The IEA Large Coil Task; Development of Superconducting Toroidal Field Magnets for Fusion Reactors," *Fus. Eng. and Design*, vol. 7, 1988. 120

[126] M. S. Lubell *et al.*, "The IEA Large Coil Task Test Results in IFSMTF," *IEEE Trans. Magn.*, vol. 24, no. 2, pp. 761–766, 1988. 120

[127] M. Leghissa, V. Hussennether, and H.-W. Neumuller, "kA-class high-current HTS conductors and windings for large scale applications," *Advances in Science and Technology*, vol. 47, pp. 212–219, 2006. 120

[128] W. Goldacker, R. Nast, G. Kotzyba, S. I. Schlachter, A. Frank, B. Ringsdorf, C. Schmidt, and P. Komarek, "High current DyBCO-ROEBEL Assembled Coated Conductor (RACC)," *J. of Phys.: Conf. Ser.*, vol. 43, pp. 901–904, 2006. 120

[129] N. J. Long, R. Badcock, P. Beck, M. Mulholl, N. Ross, M. Staines, H. Sun, J. Hamilton, and R. G. Buckley, "Narrow strand YBCO Roebel cable for lowered AC loss," *J. of Phys.: Conf. Ser.*, vol. 97, no. 012280, 2008. 120

[130] K. P. Thakur, Z. Jiang, M. P. Staines, N. J. Long, R. A. Badcock, and A. Raj, "Current carrying capability of HTS Roebel cable," *Physica C*, vol. 471, no. 1-2, pp. 42–47, 2011. 120

[131] Z. Jiang, K. P. Thakur, M. Staines, R. A. Badcock, N. J. Long, R. G. Buckley, A. D. Caplin, and N. Amemiya, "The dependence of AC loss characteristics on the spacing between strands in YBCO Roebel cables," *Supercond. Sci. Technol.*, vol. 24, no. 065005, 2011. 120

[132] L. S. Lakshmi, N. J. Long, R. A. Badcock, M. P. Staines, Z. Jiang, K. P. Thakur, and J. Emhofer, "Magnetic and transport AC losses in HTS Roebel cable," *IEEE Trans. Appl. Supercond.*, vol. 21, no. 3, pp. 3311–3315, 2011. 120

[133] Z. Jiang, R. A. Badcock, N. J. Long, M. Staines, K. P. Thakur, L. S. Lakshmi, A. Wright, K. Hamilton, G. N. Sidorov, R. G. Buckley, N. Amemiya, and A. D. Caplin, "Transport AC loss characteristics of a nine strand YBCO Roebel cable," *Supercond. Sci. Technol.*, vol. 23, no. 025028, 2010. 120

[134] N. J. Long, R. A. Badcock, K. Hamilton, A. Wright, Z. Jiang, and L. S. Lakshmi, "Development of YBCO Roebel cables for high current transport and low AC loss applications," *J. of Phys.: Conf. Ser.*, vol. 234, no. 022021, 2010. 120

[135] L. S. Lakshmi, M. P. Staines, R. A. Badcock, N. J. Long, M. Majoros, E. W. Collings, and M. D. Sumption, "Frequency dependence of magnetic ac loss in a Roebel cable made of YBCO on a Ni-W substrate," *Supercond. Sci. Technol.*, vol. 23, no. 085009, 2010. 120

[136] Z. Jiang, M. Staines, R. A. Badcock, N. J. Long, and N. Amemiya, "Transport AC loss measurement of a five strand YBCO Roebel cable," *Supercond. Sci. Technol.*, vol. 22, no. 095002, 2009. 120

[137] M. N. Wilson, "Lecture 3: Cables and quenching," Superconducting Magnets for Accelerators, JUAS, Feb 2006. 120

[138] D. Ciazynski, B. Turck, J. L. Duchateau, and C. Meuris, "AC losses and current distribution in 40 ka NbTi and Nb3Sn conductors for NET/ITER," *IEEE Trans. Appl. Supercond.*, vol. 3, no. 1, 1993. 120

[139] M. Sumption, R. M. Scanlan, and E. W. Collings, "Coupling current control in Rutherford cables wound with NbTi, Nb_3Sn, and Bi:2212/Ag," *Physica C*, vol. 310, pp. 291–295, 1998. 120

[140] M. N. Wilson, "NbTi superconductors with low ac loss: A review," *Physica C*, vol. 48, pp. 381–395, 2008. 120

[141] J. Yoo, J. Ko, H. Kim, and H. Chung, "Fabrication of Twisted Multifilamentary BSCCO 2223 Tapes by Using High Resistive Sheath for AC Application," *IEEE Trans. Appl. Supercond.*, vol. 9, no. 2, 1999. 120

[142] Z. Jiang, N. Amemiya, N. Ayai, and K. Hayashi, "AC Loss Measurements of Twisted and Non-Twisted BSCCO Tapes in Transverse Magnetic Field With Various Directions," *IEEE Trans. Appl. Supercond.*, vol. 13, no. 2, 2003. 120

[143] Z. Jiang, N. Amemiya, T. Nishioka, and S.-S. Oh, "AC loss measurements of twisted and untwisted BSCCO multifilamentary tapes," *Cryogenics*, vol. 45, no. 1, pp. 29–34, 2005. 120

[144] A. Kawagoe, F. Sumiyoshi, Y. Fukushima, Y. Wakabayashi, T. Mito, N. Yanagi, M. Takahashi, and M. Okada, "Critical Currents and AC Losses in MgB_2 Multifilamentary Tapes With 6 Twisted Filaments," *IEEE Trans. Appl. Supercond.*, vol. 19, no. 3, pp. 2686–2689, 2009. 120

[145] A. Malagoli, C. Bernini, V. Braccini, C. Fanciulli, G. Romano, and M. Vignolo, "Fabrication and superconducting properties of multifilamentary MgB_2 conductors for AC purposes: twisted tapes and wires with very thin filaments," *Supercond. Sci. Technol.*, vol. 22, no. 105017, 2009. 120

[146] M. Polak, E. Demencik, I. Husek, L. Kopera, P. Kovac, P. Mozola, and S. Takacs, "AC losses and transverse resistivity in filamentary MgB_2 tape with Ti barriers," *Physica C*, vol. 471, pp. 389–394, 2011. 120

[147] C. E. Oberly, B. Razidlo, and F. Rodriguez, "Conceptual Approach to the Ultimate Low AC Loss YBCO Superconductor," *IEEE Trans. Appl. Supercond.*, vol. 15, no. 2, pp. 1643–1646, 2005. 121

[148] M. Majoros, B. A. Glowacki, and A. M. Campbell, "Modelling of the Influence of Magnetic Screening on Minimisation of Transport AC Losses in Multifilamentary Superconductors," *IEEE Trans. Appl. Supercond.*, vol. 11, no. 1, pp. 2780–2783, 2001. 122

[149] M. Majoros, M. D. Sumption, and E. W. Collings, "Transport AC Loss Reduction in Striated YBCO Coated Conductors by Magnetic Screening," *IEEE Trans. Appl. Supercond.*, vol. 19, no. 3, pp. 3352–3355, 2009. 122

[150] F. Gomory, M. Vojenciak, E. Pardo, and J. Souc, "Magnetic flux penetration and AC loss in a composite superconducting wire with ferromagnetic parts," *Supercond. Sci. Technol.*, vol. 22, no. 034017, 2009. 122

[151] E. Pardo, J. Souc, and M. Vojenciak, "AC loss measurement and simulation of a coated conductor pancake coil with ferromagnetic parts," *Supercond. Sci. Technol.*, vol. 22, no. 075007, 2009. 122, 123

[152] P. Kovac, I. Husek, T. Melisek, M. Ahoranta, J. Souc, J. Lehtonen, and F. Gomory, "Magnetic interaction of an iron sheath with a superconductor," *Supercond. Sci. Technol.*, vol. 16, pp. 1195–1201, 2003. 122

[153] S. Safran, F. Gomory, and A. Gencer, "AC loss in stacks of Bi-2223/Ag tapes modified with ferromagnetic covers at the edges," *Supercond. Sci. Technol.*, vol. 23, no. 105003, 2010. 122

[154] M. Vojenciak, J. Souc, and F. Gomory, "Critical current and AC loss analysis of a superconducting power transmission cable with ferromagnetic diverters," *Supercond. Sci. Technol.*, vol. 24, no. 075001, 2011. 123

[155] H. Wen, W. Bailey, K. Goddard, M. Al-Mosawi, C. Beduz, and Y. Yang, "Performance Test of a 100 kW HTS Generator Operating at 67 K-77 K," *IEEE Trans. Appl. Supercond.*, vol. 19, no. 3, pp. 1652–1655, 2009. 123

[156] L. Rostila, Tampere University of Technology, "Introduction to AC losses," 2008, ESAS Summer School on Superconductivity, Finland. 135